



TOWARD A FLYING MEMS ROBOT

THESIS

Nathan E. Glauvitz, Captain, USAF

AFIT/GE/ENG/07-09

**DEPARTMENT OF THE AIR FORCE
AIR UNIVERSITY**

AIR FORCE INSTITUTE OF TECHNOLOGY

Wright-Patterson Air Force Base, Ohio

APPROVED FOR PUBLIC RELEASE; DISTRIBUTION UNLIMITED

The views expressed in this thesis are those of the author and do not reflect the official policy or position of the United States Air Force, Department of Defense, or the U.S. Government.

TOWARD A FLYING MEMS ROBOT

THESIS

Presented to the Faculty

Department of Electrical and Computer Engineering

Graduate School of Engineering and Management

Air Force Institute of Technology

Air University

Air Education and Training Command

In Partial Fulfillment of the Requirements for the
Degree of Master of Science in Electrical Engineering

Nathan E. Glauvitz, BSEE

Captain, USAF

March 2007


APPROVED FOR PUBLIC RELEASE; DISTRIBUTION UNLIMITED

TOWARD A FLYING MEMS ROBOT

Nathan E. Glauvitz, BSEE


Captain, USAF

Approved:




LaVern A. Starman, Maj, USAF (Chairman)

28 Feb 07
Date




James A. Fellows, Lt Col, USAF (Member)

6 MAR 07
Date



Guna S. Seetharaman, PhD (Member)

28 Feb 07
Date



Ronald A. Coutu, Jr., Maj, USAF (Member)

28 Feb 07
Date

Abstract

The work in this thesis includes the design, modeling, and testing of motors and rotor blades to be used on a millimeter-scale helicopter style flying micro air vehicle (MAV). Three different types of motor designs were developed and tested, which included circular scratch drives, electrostatic motors, and comb drive resonators. Six different rotor designs were tested; five used residual stress while one design used photoresist to act as a hinge to achieve rotor blade deflection. Two key parameters of performance were used to evaluate the motor and rotor blade designs: the frequency of motor rotation and the angle of deflection achieved in the rotor blades. One successful design utilized a scratch drive motor with four attached rotor blades to try to achieve lift. While the device rotated successfully, the rotational frequency was insufficient to achieve lift-off. The electrostatic motor designs proved to be a challenge, only briefly moving before shorting out; nonetheless, lessons were learned. Comb drive designs operated over a wide range of high frequencies, lending them to be a promising method of turning a rotary MAV. None of the fabricated devices were able to achieve lift, due to insufficient rotational rates and low angles of attack on the rotor blades. With slight modifications to the current designs, the required rotational rates and rotor blade deflections could yield a viable MAV. The ultimate objective of this effort was to create an autonomous MAV on the millimeter scale, able to sense and act upon targets in its environment. Such a craft would be virtually undetectable, stealthily maneuvering and capable of precision engagement.

Acknowledgments

First off, I would like to thank my wife for her constant support and understanding during our time here at Wright-Patterson AFB. I am very grateful for her continual encouragement, motivation, and taking such good care of our family everyday. Thank you to my parents for their support, encouragement, and for being excellent role models.

I would like to express my sincere appreciation to my faculty advisor Maj Starman, for his guidance and input throughout the course of this thesis effort. His insight and experience was certainly appreciated. Thank you to my sponsor Mr. Perry, from the Air Force Research Laboratory, for the support and latitude provided to me in this endeavor. Thank you to the clean room manager for his assistance capturing images on the scanning electron microscope, the images were perfect.

Nathan E. Glauvitz

Table of Contents

	Page
Abstract.....	iv
Acknowledgments.....	v
Table of Contents.....	vi
List of Figures.....	viii
List of Tables	xvi
I. Introduction to Flying Microrobots.....	1
1.1 Problem Statement	2
1.2 Research Objectives	2
1.3 Research Focus.....	3
1.4 Vision	3
1.5 Organization of Thesis	4
II. Literature Review	5
2.1 Chapter Overview	5
2.2 Rotary Style Designs.....	5
2.3 Flapping Robots	12
2.4 Airplane-Style Robots.....	17
2.5 Current MEMS Motors	20
2.6 Applications of Solar Cell Technology	22
2.7 Chapter Summary.....	24
III. Theory	25
3.1 Chapter Overview	25
3.2 Aerodynamics.....	26
3.3 PolyMUMPs Process.....	29
3.4 SUMMiT V TM Process.....	33
3.5 Circular Scratch Drives	35
3.6 Electrostatic Motor Design.....	37
3.7 Comb Drive Resonators	39
3.8 Rotor Blade Deflection.....	43
3.9 Vision of Flying Microrobot	45
3.10 Conclusion	46
IV. Modeling & Simulation.....	48
4.1 Chapter Overview	48
4.2 Comb Drive Analysis.....	48

	Page
4.3 Rotor Blade Deflection.....	52
4.4 Thrust Generation of Rotor Blades	57
4.5 Chapter Summary.....	60
V. Power Sources	61
5.1 Chapter Overview	61
5.2 Solar Cells	61
5.3 Radioisotopes as a Power Source.....	71
5.4 Thermoelectrics.....	73
5.5 Chemical Batteries	75
5.6 Chapter Summary.....	76
VI. Experimental Setup and Results.....	78
6.1 Chapter Overview	78
6.2 Signal Generation.....	78
6.3 Circular Scratch Drives	81
6.4 Three Phase Electrostatic Motors.....	84
6.5 Comb Drives	88
6.6 Rotor Blade Designs.....	95
6.6.1 Poly2/gold Rotor Blades.....	95
6.6.2 Photoresist Hinge for Rotor Blade Deflection.....	99
6.7 Chapter Summary.....	103
VII. Conclusions and Recommendations.....	106
7.1 Conclusions of Research	106
7.2 Recommendations for Future Research	107
7.3 Summary	110
Appendix A: L-Edit Mask Designs for PolyMUMPs Fabrication.....	111
Appendix B: Mask Designs for Rotor Mounting and Bending	124
Appendix C: LabVIEW VI Files and External Circuit.....	125
Appendix D: Comb Drive Calculations	128
Bibliography	130
Vita	134

List of Figures

	Page
Figure 1: Image of 8 x 5 x 8 mm ³ flying rotary device weighed 3.5 mg [1].	5
Figure 2: The 2 mm diameter rotor shown here is the smallest flying device weighing 165 µg and achieved lift in the guide at 570 Hz [1].	6
Figure 3: Predictions and experimental values of rotational frequency versus wing radial length required to achieve lift [2].	7
Figure 4: Seiko Epson developed the Micro-Flying Robot-II, one of smallest rotary flying vehicles, which weighs only 12.3 g and has a 13.6 cm diameter rotor [3].	8
Figure 5: Proposed micro air vehicle with multiple rotary drives shown in (A) was never fabricated. The individual SDA motors with wings, shown in (B), were fabricated and tested [4].	9
Figure 6: Operating rotational speed vs. the drive frequency for SDA motor with attached fan blades [4].	10
Figure 7: Initial Mesicopter concept MAV from Stanford University [5].	11
Figure 8: Mesicopter powered by eight batteries, has 1.5 cm diameter rotors [6].	12
Figure 9: Laser powered flapping design fabricated out of polysilicon and gold with a 500 µm diameter [8].	13
Figure 10: Flying Insect Thorax developed at the University of California at Berkley measures only 25 mm from wing tip to wing tip [10].	14
Figure 11: Theoretical flying micro structure which uses flapping motion [11].	15
Figure 12: The Entomopter is a flapping style robot which uses a reciprocating chemical muscle to actuate the wings [12].	16
Figure 13: The MAV shown in (A) had a 6 in wing span and was developed at the University of Arizona [13]. The Black Widow in (B) has the same wing span and was developed by AeroVironment Inc [14].	17
Figure 14: This variable-camber MAV in image (A) shows the wing configured for flight at low speeds with a high camber, while image (B) shows the configuration for maximum speed with the low camber setting [16].	18

	Page
Figure 15:	BATCAM, developed by the Munitions Directorate of AFRL, has a wing span of 21 inches and has two cameras; one forward/down looking and the other looking out the left side [18]...... 19
Figure 16:	Two comb drive resonators, like the one shown in (A), was used to drive the 10:1 gear system shown in (B). This design was fabricated by Sandia National Labs using the SUMMiT process [20]...... 20
Figure 17:	Image (A) is a multi-stator bank electrostatic motor, which operates at less than 6 V. The motor is composed of four stator banks just to the outside of the central pie-shaped wedges [23]. The electrostatic motor shown in (B) was fabricated using the PolyMUMPs process and should operate in the range of 150-300 V..... 21
Figure 18:	The triple junction a-Si solar cell above placed 100 cells in series, creating an open circuit voltage of 150 V and a short circuit current of 2.8 μ A on a 1 cm ² wafer [24]...... 22
Figure 19:	This 10 mg robot used a 2 mm ² solar cell to produce an open circuit voltage over 50 V, enough to power the actuation of the electrostatic based inchworm motors [25]. 23
Figure 20:	Example aircraft wing shows the flow of air over the airfoil. The reduced pressure on the top surface of the wing generates lift. [26]. 26
Figure 21:	Plot shows the mass of the aircraft verses Reynolds chord number for a vast range of air vehicle types [28]. 28
Figure 22:	Cross-section of an electrostatic motor design illustrating the various layers and thicknesses. 30
Figure 23:	The cross-section of the SUMMiT V TM fabrication process shows some of the realizable structures [30]. 33
Figure 24:	Scratch drive actuator drawn in L-Edit identifies the primary components and the normal direction of rotation. 35
Figure 25:	The typical structure of a scratch drive actuator plate is pictured with important regions labeled..... 36
Figure 26:	Shows the cross-sectional view of operation for the SDA. For forward motion, the drive signal operates between the priming voltage and stepping voltage [4]. 37

	Page
Figure 27:	Planar electrostatic motor designed in the PolyMUMPs process. The capacitive interaction to cause rotation only occurs at the electrode-stator interface where the thickness of the electrode is 3.5 μm thick. 38
Figure 28:	Simple illustration of comb drive resonator parts where the shuttle is able to move laterally in the x-direction. 40
Figure 29:	Simple cantilever with a fixed end on the left and a load force F acting in the x-direction on the free end. 40
Figure 30:	Relevant comb finger dimensions are labeled in the above picture. The gap between the fingers is g , t is the thickness of the material, b is the width of the fingers, l is the amount of initial overlap and d is the initial distance between the outer comb and the inner finger tip. 42
Figure 31:	Double rotor concept includes solar cell and signal conditioning circuitry with the rotors placed on top of the motors. 46
Figure 32:	L-Edit drawing of the large Poly1/Poly2 comb drive resonator with stacked comb finger and spring system. 49
Figure 33:	The Manhattan bricks mesh was applied to the large Poly1/Poly2 comb drive with resolution (10, 10, 2) μm in the (x,y,z) directions. 50
Figure 34:	Results of the CoSolvEM simulation for the large Poly1/Poly2 comb drive resonator shows a lateral shuttle displacement of 7.2 μm when 200 V are applied to the bottom two out combs. 51
Figure 35:	Lateral shuttle displacement as predicted by the CoventorWare FEM and the analytical equations for the large comb drive resonator. The predicted window of operation to achieve 7 μm of lateral displacement ranged from 180 V to 200 V. 52
Figure 36:	A sparse 3-D mesh model of cantilever beams with a resolution of (10, 10, 5) μm in the (x,y,z) directions. 53
Figure 37:	CoventorWare simulation shows the vertical deflection of Poly2/gold beams of various lengths ranging from 50-250 μm at increments of 50 μm 53
Figure 38:	These are the five wing designs that were fabricated using Poly2/gold in an attempt to achieve the desired deflection. 54

	Page
Figure 39: The CoventorWare simulation of a simplified model-A rotor shows a predicted vertical deflection of nearly 50 μm when the chord length was 500 μm long.....	55
Figure 40: Rotor blade model-C modeled in CoventorWare.	55
Figure 41: Result of simulating two sections of each rotor design when the residual stress value of gold is set to 25 MPa tensile.....	56
Figure 42: Graph shows the thrust generated by each rotor design when the $(C_1 + \phi C_d)$ term was assumed to be 0.55.	58
Figure 43: Solar spectral irradiance of sunlight incident on the earth's surface and upper atmosphere [33].	62
Figure 44: Solar cell efficiencies have greatly increased over the last quarter century [34].....	63
Figure 45: Proposed energy harvesting and storage system which will be made of polymer solar cells and lithium polymer batteries [35].	64
Figure 46: Energy band diagram of a simple p-n junction under solar illumination showing the generation of an electron hole pair when the photon was absorbed [36].	65
Figure 47: The depletion region has a specific width, W which is the active region for current productive photon absorption.	66
Figure 48: Example solar connected to a load resistance. Note the current flow is in the direction of reverse saturation current.	67
Figure 49: I-V curve for a solar cell showing the maximum power square [36].	68
Figure 50: Triple junction lattice-matched solar cell with labeled layers, produced by NREL [38].	69
Figure 51: Band diagram of a typical two junction tandem solar cell structure.	70
Figure 52: Diagram of a thermoelectric device generating power from the temperature gradient [42].....	74
Figure 53: Graph of power density and specific energy for different types of power sources, specifically performance of the nanostructured electrode Li batteries highlighted by the X's on the graph [44].	76

	Page
Figure 54: Trend in research is heading toward six junction solar cells with higher efficiencies [45].	77
Figure 55: Experimental setup for generating the signals required to run the three phase electrostatic motors.	79
Figure 56: External circuit that is used to produce square waves with high peak voltages nearly equal to Vcc.	80
Figure 57: Experimental setup showing the LabVIEW software controlling the DAQ card which is signaling the external circuit which will drive the electrostatic motors.	81
Figure 58: This scratch drive with attached 700 μm long rotor blades was fabricated in PolyMUMPS [®] run 74 and rotated at a rate of less than 3 RPM when the 9 kHz drive frequency was applied.....	82
Figure 59: Image (A) is an electrostatic motor from PolyMUMPS [®] run 71 before power was applied. Image (B) is the same motor after the three phase 150 V signal was applied. The only visible sign of shorting out that can be seen under the optical microscope is where the wires connect to the probe pads.	85
Figure 60: SEM image of an electrostatic motor design from PolyMUMPS run 71 after being tested with 150 V signals and then shorted out due to the polysilicon stringers.	85
Figure 61: The SEM image shown in (A) has Poly stringers created from having the stacked Poly1, Poly2 layers and the Poly1/Poly2 Via all the same size which is shown in the L-Edit drawing in (B).	86
Figure 62: The SEM image of an electrostatic motor shown in (A) from a design in PolyMUMPS run 75 was taken at a 45° angle and does not have any Poly stringers. L-Edit drawing (B) shows that the Poly1/Poly2 Via extends beyond the Poly1 region by 2 μm . Poly1 material that is exposed by the Via and is not covered by Poly2, will be removed by the Poly2 etch, ensuring vertical sidewalls on the stacked poly layers.	87
Figure 63: Plausible method for mounting the rotor blade to the electrostatic motor is illustrated above. The cross-sectional view, shown on the left, illustrates stacking the mounting collars onto the electrostatic motor and the top view is shown on the right.	88

	Page
Figure 64:	SEM image illustrates the important dimensions of the fabricated comb drive fingers. 89
Figure 65:	Image (A) is the large Poly1/Poly2 spring system CD with a 24 μm diameter etch hole labeled. Image (B) shows the same structure oscillating at 7,510 Hz with a 0 V to 200 V saw tooth wave being applied to the right hand side combs. 90
Figure 66:	Image (A) is the large Poly1/Poly2 spring system CD with a 28 μm gap between the shuttle and the anchor. Image (B) shows the same structure oscillating with a drive frequency of 11,310 Hz with a 0 V to 200 V saw tooth wave applied, causing $\pm 26 \mu\text{m}$ of displacement from center. 91
Figure 67:	Orthogonally linked comb drives should operate 90° out of phase to turn circular gear. 92
Figure 68:	Due to a possible drawing/fabrication error and nitride break down, the substrate is being biased to some positive potential. The toothed “pusher” is held at a 0 V potential and is attracted to the substrate; thereby not allowing the comb drive to oscillate. 94
Figure 69:	Graph of the three different results obtained by experiment, FEM and analytical calculations. 95
Figure 70:	Deflection curve for rotor blade with a cord length of 250 μm is shown in image (A). The red line in image (B) shows the location on the wing where the cross-sectional plot was taken. 97
Figure 71:	Image (A) shows the chip after the first step of exposure and development, a large majority of the PR is still in place. Image (B) shows the result after a second sequence of exposure and development was completed. The only unwanted remaining PR is the edge bead seen near the very top portion of image (B). 101
Figure 72:	Four layers of Rohm & Haas 1818 photoresist are masking the spar-Poly1 blade joint in (A) prior to fully releasing the sacrificial oxides. Image (B) shows the result after five minute etch in HF acid and drying on a hot plate for 5 minutes. 101
Figure 73:	Image (A) shows the probe tip lifting up the Poly1 rotor blade. After that portion of the rotor blade is removed, image (B) shows the remaining PR which partially caused the rotor blade to not achieve any deflection. 102

	Page
Figure 74:	Image (A) shows an improved concept of the cross-section of a rotor blade with photoresist on prior to releasing the device in HF acid. The image in (B) shows how the rotor blade should look after the oxide layers are removed. 103
Figure 75:	Proposed design would consist of four rotors with two independent banks of pusher comb drives and four small independent clutch comb drives. Views shown are from the bottom and side respectively..... 109
Figure 76:	MUMPs® 71 Glauvitz Chip 1 scratch drives and test structures. 112
Figure 77:	MUMPs® 71 Glauvitz Chip 2 electrostatic motors and rotor test structures. 113
Figure 78:	MUMPs® 71 Glauvitz Chip 3 scratch drive with rotors and large cantilever beams. 114
Figure 79:	MUMPs® 72 Glauvitz Chip 1 electrostatic motors with rotor mounting collars. 115
Figure 80:	MUMPs® 72 Glauvitz Chip 2 electrostatic motors with rotor mounting collars. 116
Figure 81:	MUMPs® 73 Glauvitz Chip 1 electrostatic motors with rotor mounting collars. 117
Figure 82:	MUMPs® 73 Glauvitz Chip 2 electrostatic motors with rotor mounting collars. 118
Figure 83:	MUMPs® 73 Glauvitz Chip 3 with rotor designed for photoresist hinge. 119
Figure 84:	MUMPs® 74 Glauvitz Chip 1 thermal actuators drive a gear system. 120
Figure 85:	MUMPs® 74 Glauvitz Chip 2 contains a scratch drive with rotors, electrostatic motors, and thermal actuator array driving a gear with wings. 121
Figure 86:	MUMPs® 75 Glauvitz Chip 1 layout of electrostatic motors and comb drive resonators. 122
Figure 87:	MUMPs® 75 Glauvitz Chip 2 has different electrostatic motors, comb drive resonators rotating a wheel and cantilever beam sensor designs. 123

	Page
Figure 88: Mask designed in L-Edit to achieve rotor bending and bonding location of the rotor to the electrostatic motors.	124
Figure 89: LabVIEW block diagram that is used to generate the three phase signals designed to operate the electrostatic motors.	125
Figure 90: The LabVIEW front panel shows the variables that can be adjusted and what the signal at each output will look like.	126
Figure 91: One of the external circuits built to drive the three phase motors.	127

List of Tables

	Page
Table 1: List of characteristics for the Seiko Epson Micro-Flying Robot-II [3].	8
Table 2: Comparison of mass, radius, and rotational frequency for three different helicopter designs.....	29
Table 3: Analytical values for comb drive spring constant, electrostatic force and shuttle displacement.	49
Table 4: Comparison of the FEM and numerical calculations for rotor blade deflection and angle of attack.	57
Table 5: The thrust generated for each rotor design operating at 250 Hz is shown. The other listed parameters are derived from the thrust calculation.	59
Table 6: Support structure minimum dimensions based on the thrust generated by each.	59
Table 7: List of factors that reduce solar cell efficiency.	71
Table 8: Important comb drive dimensions for the fingers and springs.	89
Table 9: Measured vertical deflection of the rotor blade tips versus predicted.	98
Table 10: Comparison of the experimental angle of deflection versus predicted.	99
Table 11: Summary of motor performance done in this work compared to other state of the art motors.	105

TOWARD A FLYING MEMS ROBOT

I. Introduction to Flying Microrobots

Microrobotics is a rapidly increasing field of research and development which could be utilized in a wide range of operations including remote sensing, surveillance, chemical contamination detection, or reconnaissance. Miniature flying microrobots could be deployed from a safe location to investigate any situation that is deemed too dangerous or inaccessible to humans. Hazardous material spill areas or radiation exposed environments could be sampled for contamination levels by an autonomous, disposable micro air vehicle (MAV) prior to endangering human investigators.

There are an abundant number of applications where MAVs could be used in a surveillance role. Imagine a MAV smaller than a house fly, virtually undetectable, and able to position itself to monitor conversations. Something so small could travel through ductwork in a building or delve deep into a cave to probe for information.

The vast realm of applications for nano and micro robotics is limited only by the imagination. Realizing these novel ideas on the other hand, is limited by current fabrication and design technology. As nano technology advances, many different sensors could be integrated into a MAV, giving it more functionality.

Very few people have fabricated flying robots on the 10-centimeter scale and even fewer on the millimeter scale. No man-made flying devices exist today that are truly on the micro scale, less than 1 millimeter. By convention, the largest dimension of a robot determines its size scale, not its smallest feature size.

1.1 Problem Statement

There are many avenues that could be taken in pursuit of creating a millimeter-scale flying robot. The style of motor or driving mechanism used to generate the thrust required for lift-off will determine the power requirements necessary for the device to operate. The two primary methods used in MEMS to cause motion are electrical and thermal actuation. For electrical actuation, some methods are capacitive in nature, which use fairly high voltages and low currents. In applications of electro-thermal actuation, high currents and low voltages are typical. Thermal actuation can also be accomplished by using a light source such as a laser.

A helicopter style design would provide a good platform for a MAV surveillance device. Due to the small scale of the rotors, the frequency of rotation will most likely need to be in the range of hundreds of rotations per second. Two mechanisms to achieve a high rate of rotation should be considered; a direct drive system or the use of gear ratios could be used to achieve the desired speed.

A major difficulty in designing flying robots on the millimeter scale and below, exists in finding a power source that can supply sufficient energy in a very lightweight package. Several different sources of power will be compared later in this document, including batteries, solar cells, betavoltaics, and thermoelectrics.

1.2 Research Objectives

The objective of this research was to create a millimeter-scale structure capable of independent powered flight through the design, fabrication, testing, and modeling of a rotary driven flying robot. The concept pursued was to attach rotary blades to a circular

drive mechanism and generate sufficient lift to overcome the force of gravity. There are three main contributing factors to the success of a MAV. The robot must be extremely light weight, the rotor blades must have the correct angle of attack, and the motor must be able to turn the rotor at the desired rate. The rotational frequency of the rotors plays a large role in how much thrust is generated. Few projects on the millimeter scale have been successful in this endeavor using other lift techniques. In this work, power is applied to the motors from an external source via probes. A miniature power supply would need to be incorporated in future work to achieve independent flight.

1.3 Research Focus

The focus of this research was to design, test, and compare different motors that could be used to turn the rotors of a MAV. The second objective was to fabricate rotors and achieve the desired amount of deflection to maximize thrust. The integration of the motor and rotor connection will also be discussed.

The mass of an aero vehicle has always been a primary concern for robotic design engineers. Future work could implement techniques to thin the substrate, reducing the overall mass of the flying robot. Less mass means less thrust will be needed to lift the robot off the ground. Since the devices will be fabricated using the Polysilicon Multi-User MEMS Processes (PolyMUMPs), much of the 500 μm thick substrate could be removed.

1.4 Vision

The ideal microrobot would be capable of autonomous operation for a few hours or even a few months. This would require a power source capable of lasting that long or

the ability to scavenge power from an external source. If an external power source is to be used, some method of power storage should be incorporated to allow the robot to operate when the primary external source is not available. Possible energy storage mechanisms are rechargeable batteries or supercapacitors, or a combination of both.

With current technology, the most probable mission for a flying robot less than 3 mm in diameter is a listening device, chemical sensor, or a small optical imaging system. MEMS microphones and cantilever sensors used to detect chemical contamination are very small and could be easily implemented. A small array of sensors for optical imaging could also be employed.

1.5 Organization of Thesis

The remaining material will be broken down into the following sections of this thesis. Chapter 2, the Literature Review, presents a thorough examination of the progress made to date in the arena of flying microrobots. Several examples of the latest and greatest flying robots will be discussed. Chapter 3 will focus on the relevant theories of aerodynamics, motor operation, and rotor blade deflection will be presented. Chapter 4, Modeling & Simulation, will cover some finite element analysis on different motors and rotor blade designs. Subsequently, power sources will be looked at in Chapter 5. The Experiment Setup and Results section will show what successes have been made during this endeavor in Chapter 6. Finally this thesis concludes with some recommendations regarding this and future work in MAV design.

II. Literature Review

2.1 Chapter Overview

The purpose of this chapter is to cover what current researchers have achieved up to this point in flying microrobots. The three main approaches engineers have taken in designing flying microrobots include: helicopter style, standard airplane style, and flapping methods designed to mimic insect flight, called biomimetics.

2.2 Rotary Style Designs

The smallest, most successful miniature robot is based on a rotary design shown in Figure 1. An alternating magnetic field is used to cause the wings to rotate. The rotor diameter was five millimeters from tip to tip for this particular design and was able to achieve lift when the alternating magnetic field oscillated at 500 Hz.

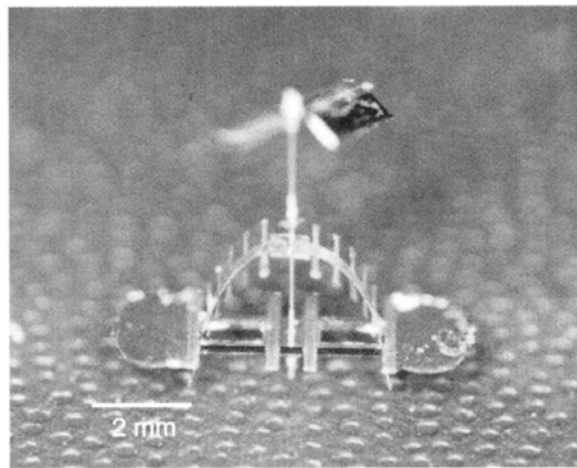


Figure 1: Image of $8 \times 5 \times 8 \text{ mm}^3$ flying rotary device weighed 3.5 mg [1].

Many experiments were performed using the alternating magnetic field, varying the size of the wings which ranged from 8 mm all the way down to the model in Figure 2,

which spanned approximately two millimeters. A glass rod was placed through a hole in the electroplated Ni, CoNi magnetic wings, which was then placed into a glass tube guide. The Greek letter ϕ shown in Figure 2 is a variable representing the diameter of the glass. The glass tube guide is necessary to hold the device upright in place, but is able to “freely” rotate when the wings are acted upon in the alternating magnetic field. The experimental designs started out large at 8 mm and progressively were designed smaller to the size of the device shown in Figure 2. The roughly 2 mm diameter rotor had a mass of 165 μg and achieved lift in the guide at a rotational frequency of 570 Hz.

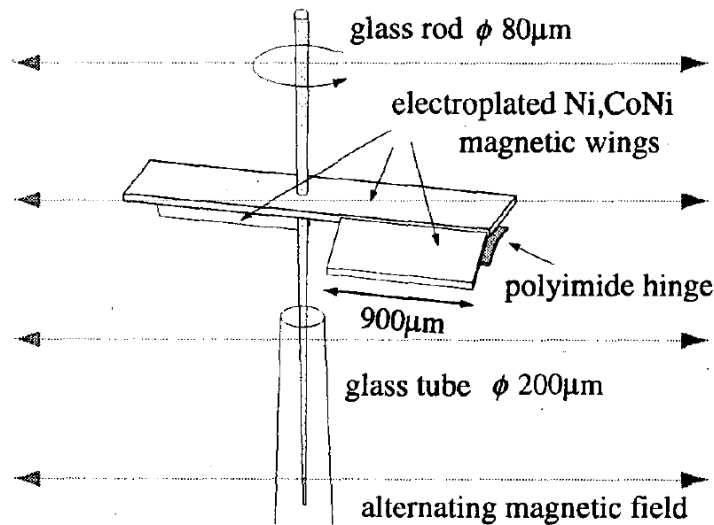


Figure 2: The 2 mm diameter rotor shown here is the smallest flying device weighing 165 μg and achieved lift in the guide at 570 Hz [1].

For rotor designs with a small radius R , when R was 1-8 mm, the frequency of rotation to achieve lift was proportional to $R^{-0.9}$ as shown in Figure 3. Although use of a magnetic field to power a flying robot outside of a laboratory has very little application, the data gathered provided valuable insight into flying microrobots at this scale.

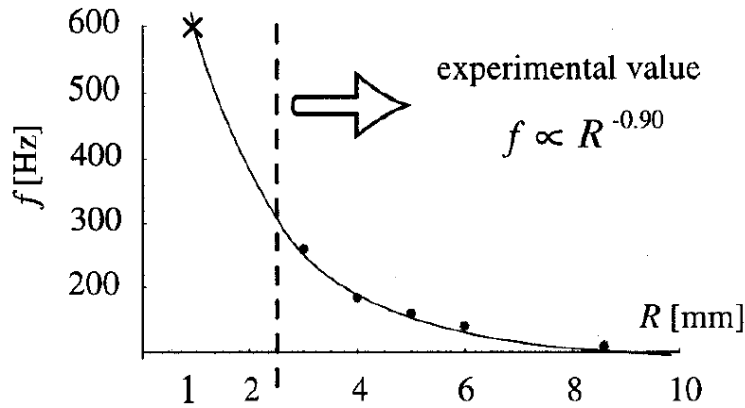


Figure 3: Predictions and experimental values of rotational frequency versus wing radial length required to achieve lift [2].

The next successful and much larger rotary driven flying platform was developed by Seiko Epson. Pictured in Figure 4, the Micro-Flying Robot – II (μ FR-II), is equipped with a sensor which can capture and then transmit images to a nearby monitor. The signal is transmitted via a Bluetooth wireless connection. MEMS gyro-sensors allow the onboard control system to attain independent flight. Successful fabrication of this design resulted from two universities and laboratories contributing important inputs, including advice on the ultrasonic motor design as well as collaborative work on the control system.

Several important upgrades were made to improve the performance over the first μ FR. Originally, wires were attached to deliver the power to the ultrasonic motors and circuitry. In addition, the μ FR was remotely controlled and unable to fly without human intervention. The μ FR-II is truly an autonomous flying robot. As improvements in battery technology advance, this will soon be a very useful system for a vast range of applications. Table 1 shows the important specifications of the μ FR-II [3].

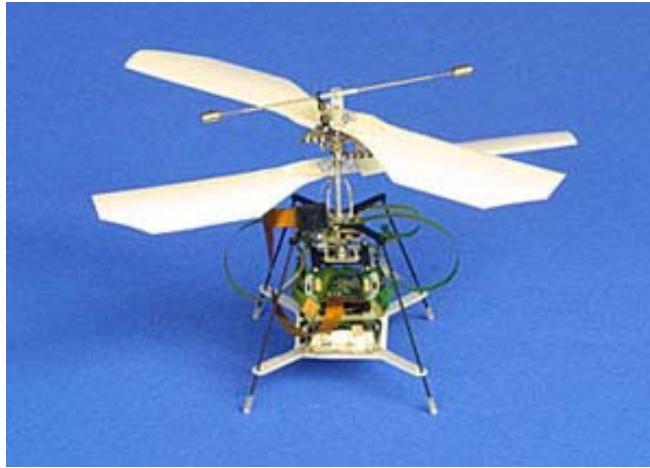


Figure 4: Seiko Epson developed the Micro-Flying Robot-II, one of smallest rotary flying vehicles, which weighs only 12.3 g and has a 13.6 cm diameter rotor [3].

Table 1: List of characteristics for the Seiko Epson Micro-Flying Robot-II [3].

Voltage	4.2 V
Power	3.5 W
Time of flight	~3 Minutes
Diameter	13.6 cm
Height	8.5 cm
Motor Type	Ultrasonic Motor
Power Source	Polymer-lithium battery

Several conceptual MAV designs have been theorized over the last few years at different universities which have proposed ideas similar to the one pictured in Figure 5. The design pictured in Figure 5 envisioned a multi-rotor device with a very thin frame to reduce the overall mass of the design. The circular scratch drive actuators used to rotate the design are shown in Figure 5 (B) with the attached rotor blades. The large angle of deflection in the rotor blades was achieved by using solder sphere assembly. The solder spheres have a tin and lead composition and are deposited in a three step process. First

they are placed on top of the unreleased hinge joint of the rotor blade and outer rim of the scratch drive actuator (SDA). The spheres are then reflowed in a heated vapor of N_2 -formic acid. Next the sacrificial oxides are removed in a 48% solution of hydrofluoric acid and dried in a CO_2 dryer. The final step is to reflow the spheres again in a heated vapor of N_2 -formic acid to achieve the desired amount of deflection. Through earlier work, recipes were developed to achieve blade deflections ranging from 0° to 90° .

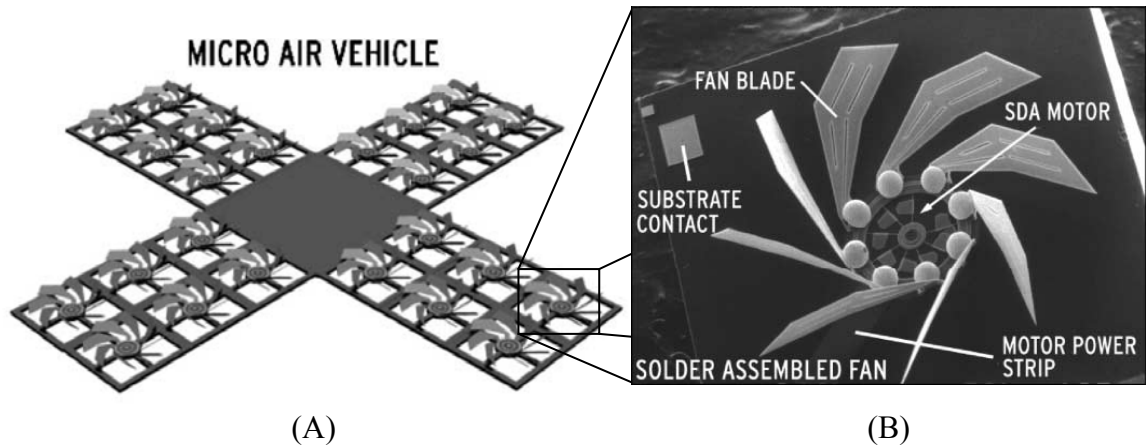


Figure 5: Proposed micro air vehicle with multiple rotary drives shown in (A) was never fabricated. The individual SDA motors with wings, shown in (B), were fabricated and tested [4].

The results for rotational frequency achieved verses drive frequency of a SDA are shown in Figure 6. The drive signal reached the maximum frequency of operation at 15 kHz. The maximum frequency of operation is believed to be due to squeeze-film dampening effects. Under ambient air pressure the electrostatic plates are unable to effectively actuate due to the inability of the air to flow out from under the plate and back under again [4].

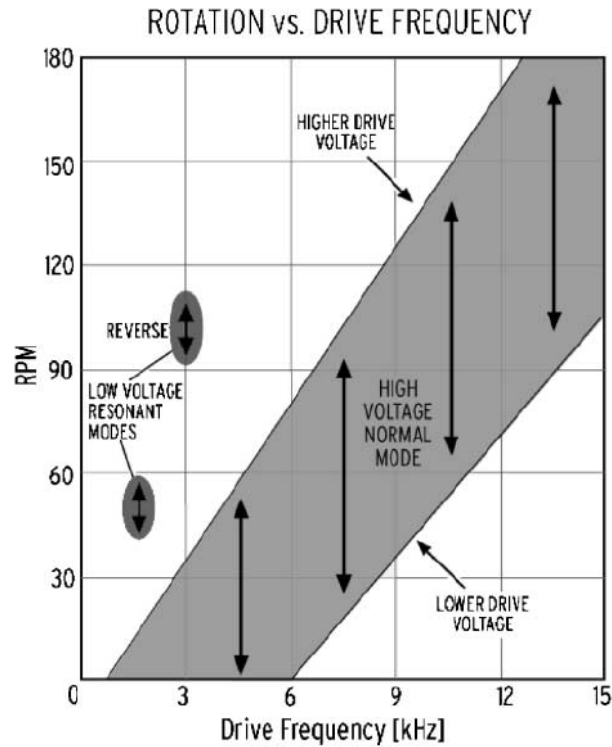


Figure 6: Operating rotational speed vs. the drive frequency for SDA motor with attached fan blades [4].

The moderately high operating voltage required to make the SDA function is one disadvantage. The larger drawback is the low frequency of rotation; SDA motors with attached rotor blades have rotated at speeds in the range of 1 – 180 RPM [4].

Another helicopter design is the mesicopter concept MAV shown in Figure 7, which was developed at Stanford University in California [5]. This design is envisioned to operate in a swarm of many robots; each working to collect data on Earth or potentially Mars. After the conceptual design was worked out, progress was made in fabricating a centimeter-scale mesicopter which is shown in Figure 8. A magnetic induction motor is used to turn the rotors.

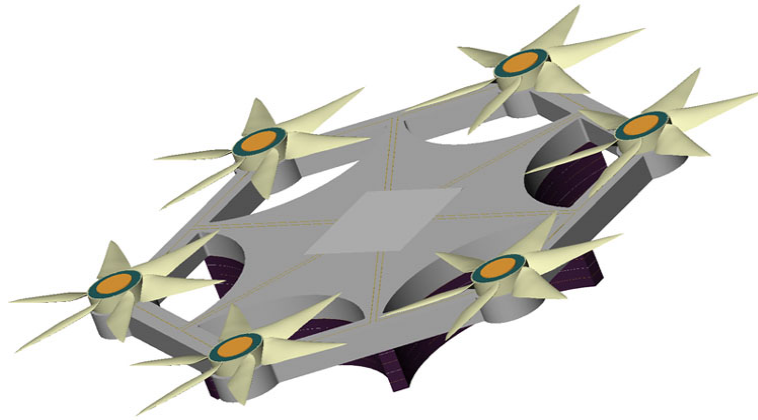


Figure 7: Initial Mesicopter concept MAV from Stanford University [5].

The required four phase alternating current generates a rotating magnetic field in the center of the stators. Inside the stators is a soft or hard magnetic core material which is turned in the rotating magnetic field. The impedance of the exterior stators is very low so the motors require high current and low voltages to operate. A key aspect of operation of these motors is that they are three dimensional; having some substantial height, which increases the amount of torque they are able to produce.

Several different off-the-shelf batteries were tested to determine which type would provide adequate power for the four motors. One motor needs 45-50 mA to operate at the required RPM. The batteries tested were composed of lithium manganese dioxide, silver oxide, or nickel cadmium. The best power density achieved was 124 mW/g after some of the exterior portions of the battery were removed by grinding and sanding. When external wires are connected to power the Mesicopter, enough thrust is generated that each motor can lift 700 mg. The motor and rotor assembly has a mass of 325 mg, leaving 375 mg per motor that can be used for airframe and batteries [7]. The Mesicopter is not yet flying under battery power.

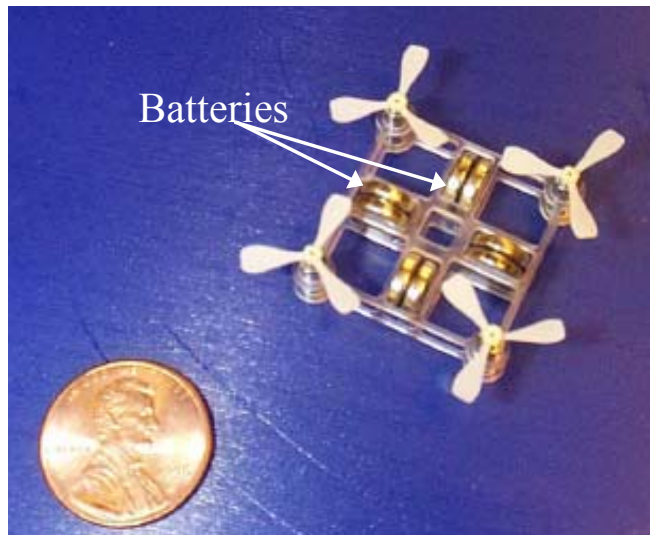


Figure 8: Mesicopter powered by eight batteries, has 1.5 cm diameter rotors [6].

2.3 Flapping Robots

The microrobot shown in Figure 9 was designed at the Air Force Institute of Technology. Using the inherent residual stress in PolyMUMPs for the Poly2/gold layer, the wings deflect upward at room temperature. Materials with different coefficients of thermal expansion when in contact expand at different rates, causing deflection. A pulsed 40 mW laser is focused on the center of the robot to generate heat. The gold layer on the top expands more than the Poly2 layer, thus causing the wings to deflect downward. When the laser pulse is off, the wings cool and return back to the original ambient temperature position. The wing experienced $9\text{ }\mu\text{m}$ of downward deflection when approximately 12 mW of power was absorbed from the laser [8]. The remainder of the power from the laser beam was either reflected or transmitted through the material. This design only weighed $1.34\text{ }\mu\text{g}$ which is approximately 123 times lighter and less than half the diameter of the Miki rotating device [1],[8]. Wing beats were achieved in the 1 to

4.69 kHz frequency range. This flapping microrobot design did not achieve lift, but theoretically it could if the robot's mass was reduced or if it could flap 5 times faster, the device could achieve lift.

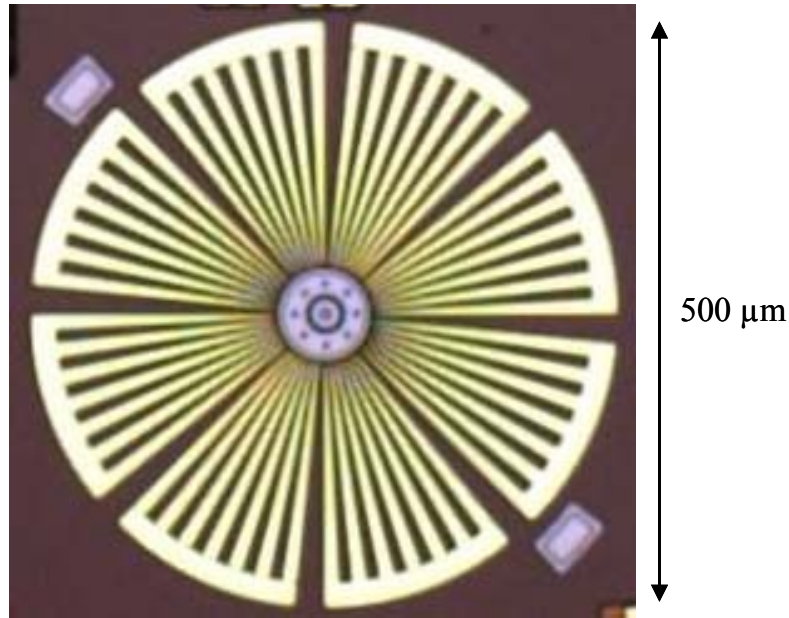


Figure 9: Laser powered flapping design fabricated out of polysilicon and gold with a 500 μm diameter [8].

The Micromechanical Flying Insect (MFI) thorax developed at the University of California, Berkeley used four piezoelectric actuators and fiber-reinforced composites in an attempt to achieve lift [9]. The device pictured in Figure 10 is 25 mm in the largest dimension and weighs 30 mg. Wing beats have been accomplished at 170 Hz but it requires a 250 V power source to operate the actuators. Fine gold wires connected to an external power source are required for the device to operate. The MFI thorax has not been able to achieve un-tethered liftoff with the current design.

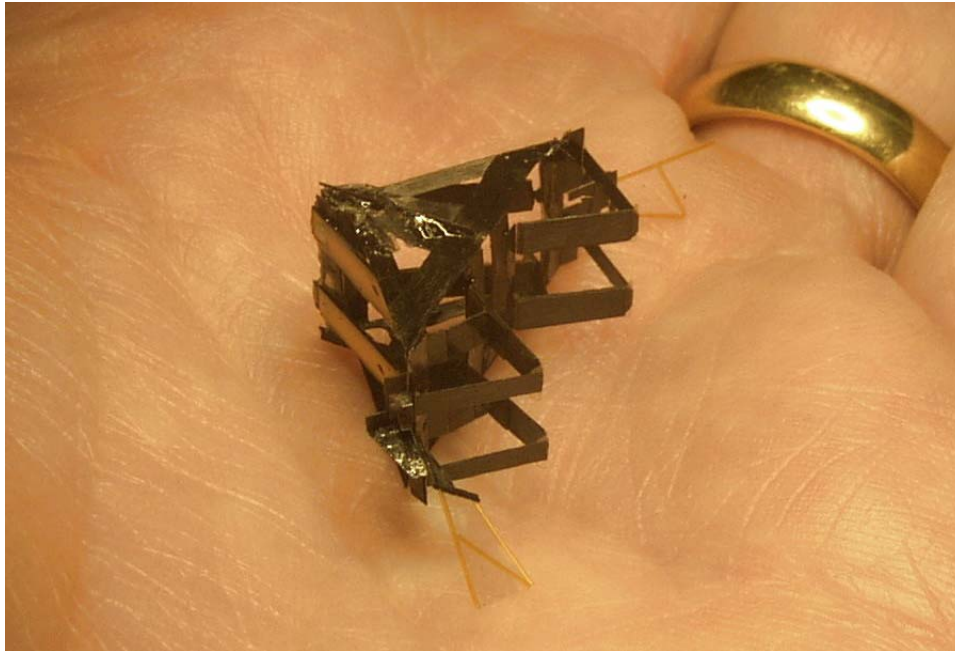


Figure 10: Flying Insect Thorax developed at the University of California at Berkley measures only 25 mm from wing tip to wing tip [10].

The image in Figure 11 depicts a proposed flying microrobot designed by Chan *et. al.* [11]. They looked at a wide range of insects making comparisons of mass to wing beating frequency and surface area of the wing. They chose to fabricate the flapping mechanism out of thermal actuators and parylene. With a 6 V power source, fairly large deflection in the actuator was achieved. The current needed was not explicitly stated, but each actuator has a 1 k Ω resistance, so the current through each actuator is about 6 mA. In the proposed design there are 36 actuators on the robot, meaning the robot would need ~ 1.296 W of power, which is very high for a micro-size device. The dimension of each actuator was $1,000 \times 100 \times 0.8 \mu\text{m}^3$ and could beat at a frequency of 200 Hz. The dimensions are comparable in size to that of an insect and it was determined that a flapping silicon-based microrobot could theoretically fly if a 1.3 W power source was on

board which wouldn't significantly increase the robot's mass. The flapping actuators were fabricated and tested, but the final flying micro structure was not completed.

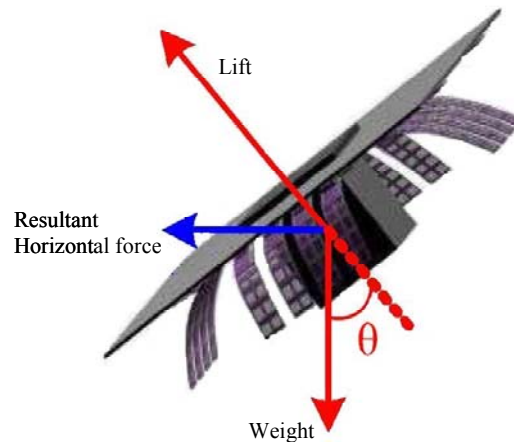


Figure 11: Theoretical flying micro structure which uses flapping motion [11].

The Entomopter, pictured in Figure 12, is the largest flapping style design that will be discussed in this section. The flapping motion is generated by the reciprocating chemical muscle (RCM) actuator now in its fourth generation. The chemical reaction requires no ignition source, combustion, or oxygen from the atmosphere. This method of locomotion is attractive because RCM can function under water or in an atmosphere that doesn't have oxygen available for standard combustion reactions. Information is scarce on the exact inner workings of the RCM due to the process being patented.

Various scale wings designs on the Entomopter could be created for flight on Earth or even on Mars. The atmosphere and gravitational force greatly affect the physical requirements for flight. The Martian atmosphere is roughly less than 1 % the density of the atmospheric pressure here on earth and the force of gravity is 37 % that of the Earth's gravitational force. The advantage of the flapping design of the Entomopter

is that the forward speed of motion required for flight is much slower than an airplane style robot. The surface of Mars is very rocky, collecting and returning samples to a Mars rover would be nearly impossible with a standard airplane style robot.

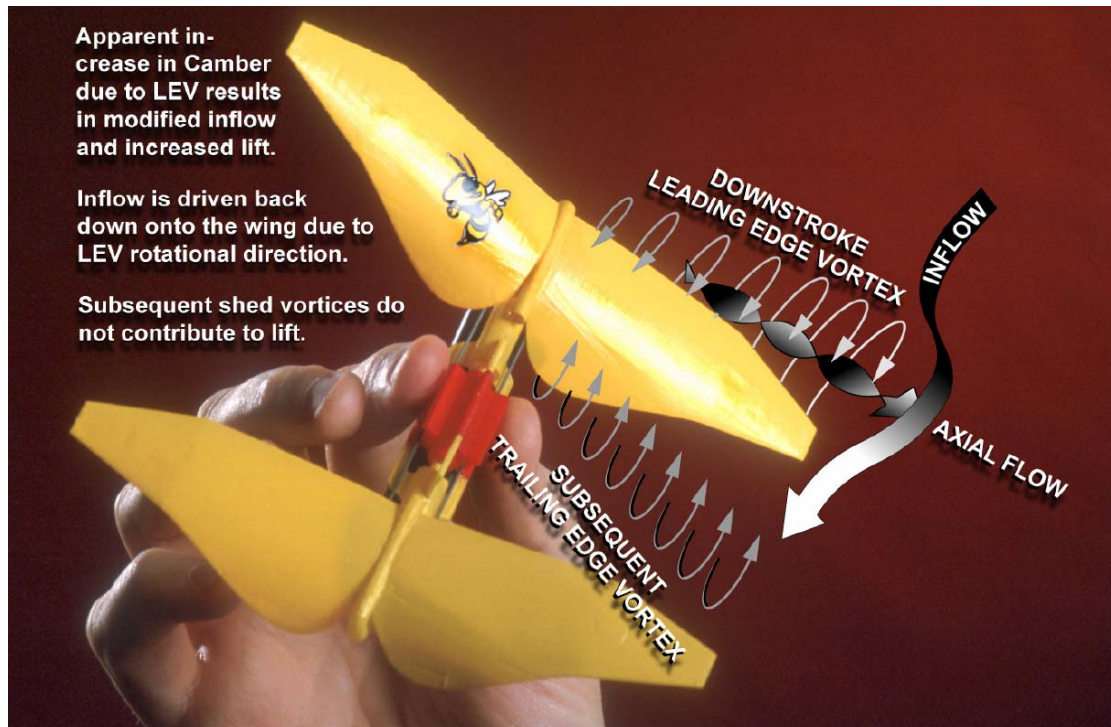


Figure 12: The Entomopter is a flapping style robot which uses a reciprocating chemical muscle to actuate the wings [12].

Some interesting power scavenging and utilization techniques have been implemented on the Entomopter. The RCM powers the wing flapping motion while the exhaust gasses act as gas bearings between all movable surfaces. The exhaust gasses can also be controlled when vented to aid in flight control. Thermoelectrics are used to generate electricity from the RCM waste heat to power onboard sensors.

2.4 Airplane-Style Robots

Many airplane-style MAVs have been produced to date. They range in capability from flights of under a minute to 30 minutes or more. The aircraft could be remote controlled or have GPS guided internal flight paths programmed in prior to or during mid-flight. Other semi-autonomous micro planes have onboard collision avoidance programs to navigate simple obstacles.

Two of the smaller MAVs that were found are pictured in Figure 13. The craft shown in Figure 13 (A) was developed at the University of Arizona (UA) and has a 6 in wing span. It is radio controlled and has a camera which can store the still images onboard. In flight tests, the UA MAV was able to fly for over eight minutes [13].

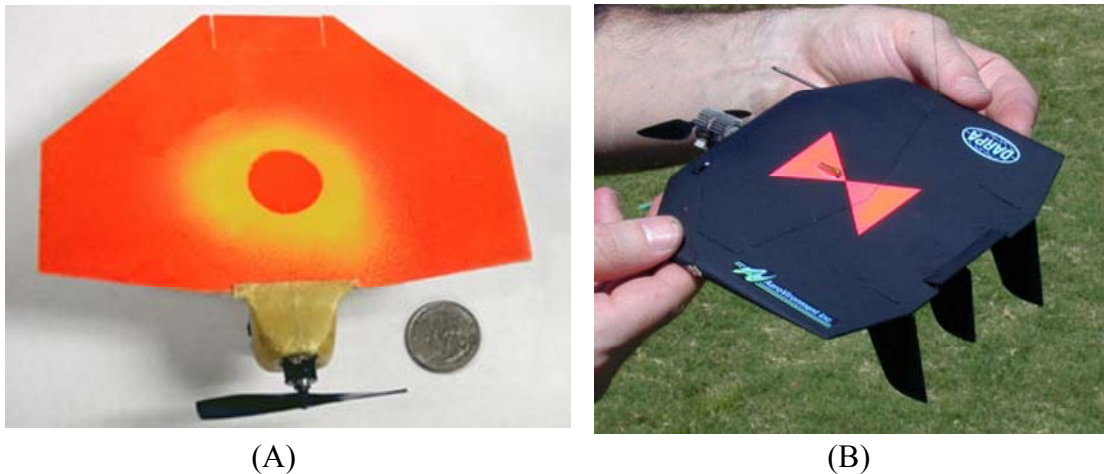


Figure 13: The MAV shown in (A) had a 6 in wing span and was developed at the University of Arizona [13]. The Black Widow in (B) has the same wing span and was developed by AeroVironment Inc [14].

The Black Widow shown in Figure 13 (B) is the same size, but has several more advanced features. Color video from the craft is transmitted via downlink to the operator with a range of up to 1.8 km and can fly for just over 30 minutes. A small avionics suite

is incorporated into the video feed, displaying: magnetic heading, altitude, air speed, debugging information, and battery status. The Black Widow is the smallest, radio controlled MAV with some limited autonomous operation. It is able to autonomously maintain, altitude, speed, heading, or yaw when directed [14].

Another MAV created at the University of Arizona, shown in Figure 14, is able to change the camber of the wings. Camber is defined as the asymmetry between the top and bottom curvatures of an airfoil [15]. A larger camber in the wing allows for more lift at slower speeds, while a small camber requires faster speeds through the air to achieve the same amount of lift. The variable-camber allows the UAV to fly at speeds ranging from 11 to 33 mph, allowing it to arrive at a target rapidly and then observe the target at a slower speed. In the current configuration, the plane is radio controlled and there is no on board camera, but the ability to operate at slower speeds would produce superior quality video footage [16].

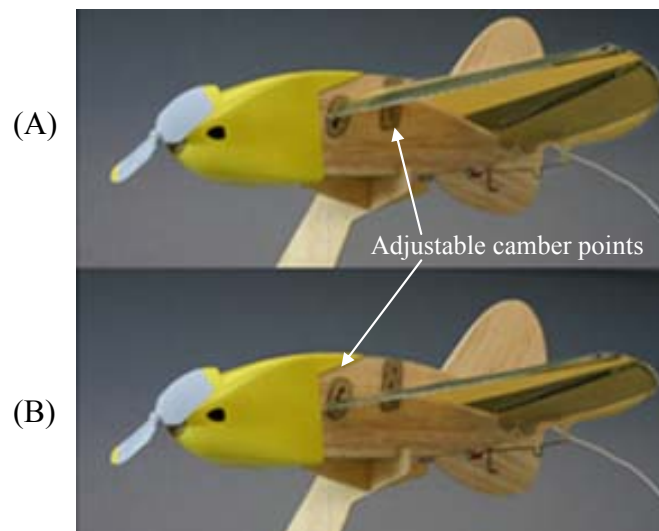


Figure 14: This variable-camber MAV in image (A) shows the wing configured for flight at low speeds with a high camber, while image (B) shows the configuration for maximum speed with the low camber setting [16].

The BATCAM (Battlefield Air Targeting Camera Autonomous Micro-air-vehicle) shown in Figure 15 is the largest and most capable airplane style robot that will be discussed. It has a 21 in wing span and has two onboard cameras; one forward/down looking and the other looking out the left side. Live images, video, or stills from the cameras can be transmitted back to the control laptop during the flight, similar to the Back Widow MAV. Unlike the Black widow, the BATCAM can have flight paths programmed before flight or changed mid-flight if there is a line-of-sight to the control laptop. The BATCAM has GPS and inertial navigation systems onboard allowing it to follow programmed way points. It can be flown via radio control or autonomously with a range of three kilometers [17].



Figure 15: BATCAM, developed by the Munitions Directorate of AFRL, has a wing span of 21 inches and has two cameras; one forward/down looking and the other looking out the left side [18].

The wings are made of a flexible material capable of folding around the fuselage, allowing the BATCAM to be backpack portable and weigh less than 400 g. It uses

batteries to power the electric motor and can fly missions for approximately 18 minutes. BATCAMs are currently used by US forces overseas.

2.5 Current MEMS Motors

Many different types of MEMS motors have been fabricated in recent years. The microengine, developed at Sandia National Labs, is partially shown in Figure 16. Two sets of orthogonal comb drive resonators (one is shown in Figure 16 (A)), operate 90° out of phase, to turn the drive gear in the upper right corner of Figure 16 (B). Similar fabricated devices were able to rotate at speeds up to 200,000 RPM while driving multiple gears [19]. The comb drives could drive gears, with a 90 V square wave, over a large range of drive frequencies, ranging from 0.5 Hz to 3.33 kHz.

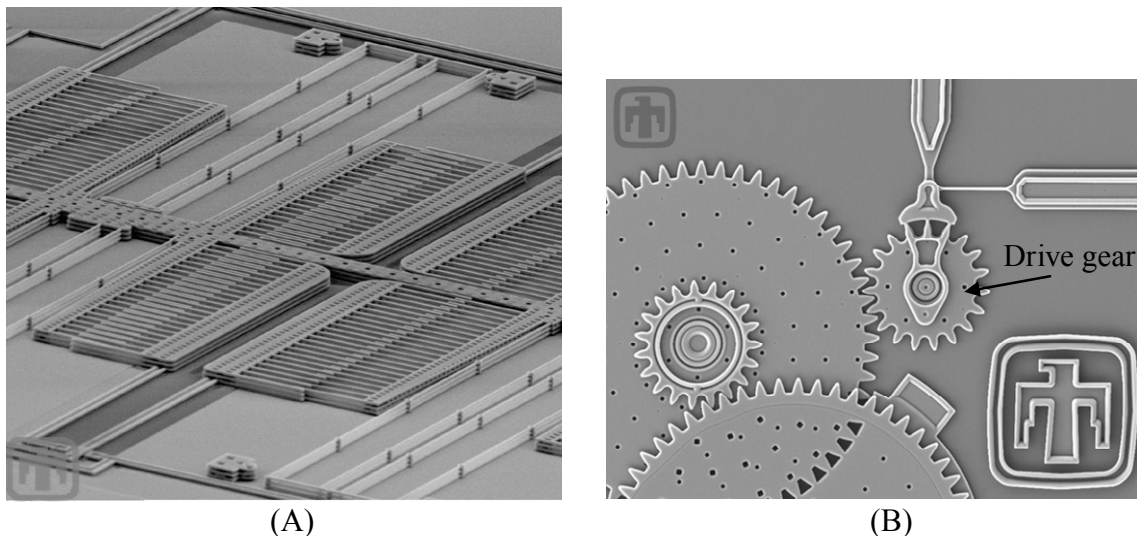


Figure 16: Two comb drive resonators, like the one shown in (A), was used to drive the 10:1 gear system shown in (B). This design was fabricated by Sandia National Labs using the SUMMiT process [20].

The large frequency range of operation means the electrostatic force between the comb fingers is causing the motion in the small gear, not the spring force. The springs

are acting like a guide to ensure the inter-digitized comb fingers do not short out. One microengine demonstrated the ability to rotate a 1,600 μm diameter optical shutter; surmounting a potentially problematic large surface from suffering stiction issues [19].

Another form of electrostatic actuation which has been demonstrated is the circular electrostatic motor. The electrostatic motor in Figure 17 (A) was fabricated in the SUMMiT process and possesses four stator banks just outside the pie-shaped wedges. The four stators produce six times the capacitive force compared to a planar electrostatic motor, which allows the drive voltage to be less than 6 V. The motor operates using four phases, with only one line on at a time. The paper published by Krygowski *et. al.*, did not reveal a maximum achieved rotational frequency [21].

The three phase electrostatic motor design shown in Figure 17 (B) was fabricated using the PolyMUMPs process. Similar designs had internal stator diameters of 120 μm and were able to rotate at speeds ranging from 50 to 500 RPM [22]

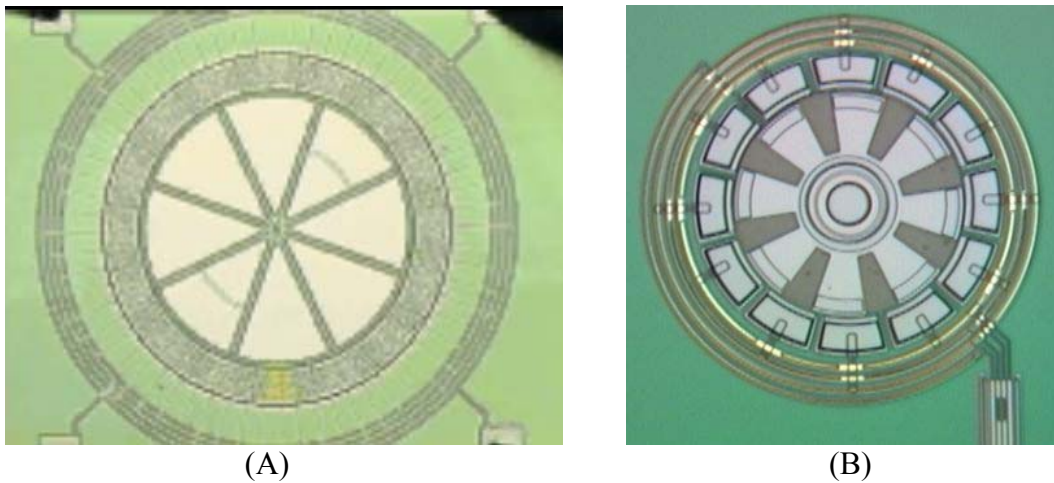


Figure 17: Image (A) is a multi-stator bank electrostatic motor, which operates at less than 6 V. The motor is composed of four stator banks just to the outside of the central pie-shaped wedges [23]. The electrostatic motor shown in (B) was fabricated using the PolyMUMPs process and should operate in the range of 150-300 V.

2.6 Applications of Solar Cell Technology

Solar cell technology is rapidly increasing from less than 10% efficiency to over 36% efficiency in the last 30 years. The theory of solar cell operation will be covered in detail in Chapter 5, while this section highlights two examples of the best performers. Two high voltage, low current solar cells have been fabricated by placing small solar cells in series.

The solar cell shown in Figure 18 was fabricated using triple junction a-Si (amorphous silicon) and achieved an efficiency of 12%. The goal of the research was to create a packaged MEMS device that was strictly powered by a solar cell. The voltage generated by the solar cell was used to control the amount of deflection of a MEMS Si mirror.

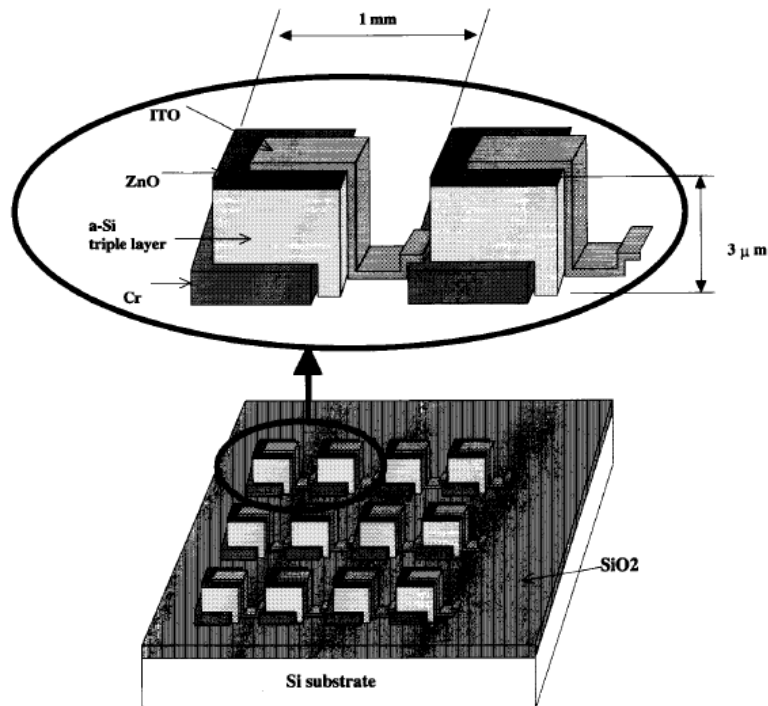


Figure 18: The triple junction a-Si solar cell above placed 100 cells in series, creating an open circuit voltage of 150 V and a short circuit current of $2.8 \mu\text{A}$ on a 1 cm^2 wafer [24].

The edge deflection of the mirror was able to be controlled in a repeatable fashion over a range of 55 μm . The amount of deflection experienced by the mirror was controlled by varying the intensity of light incident on the solar cell. On a 1 cm^2 area of a wafer, 100 single solar cells were connected in series to produce an open circuit voltage of 150 V and a short circuit current of 2.8 μA . Indium tin oxide (ITO) is optically transparent and is used to connect the top surface of one solar cell to the bottom electrode of the next cell [24].

Another example of a high voltage solar cell integration was demonstrated on a walking robot, developed at the University of California, Berkeley is shown in Figure 19. The solar cell could produce an open circuit voltage of 50 V and generate 100 μW of power.

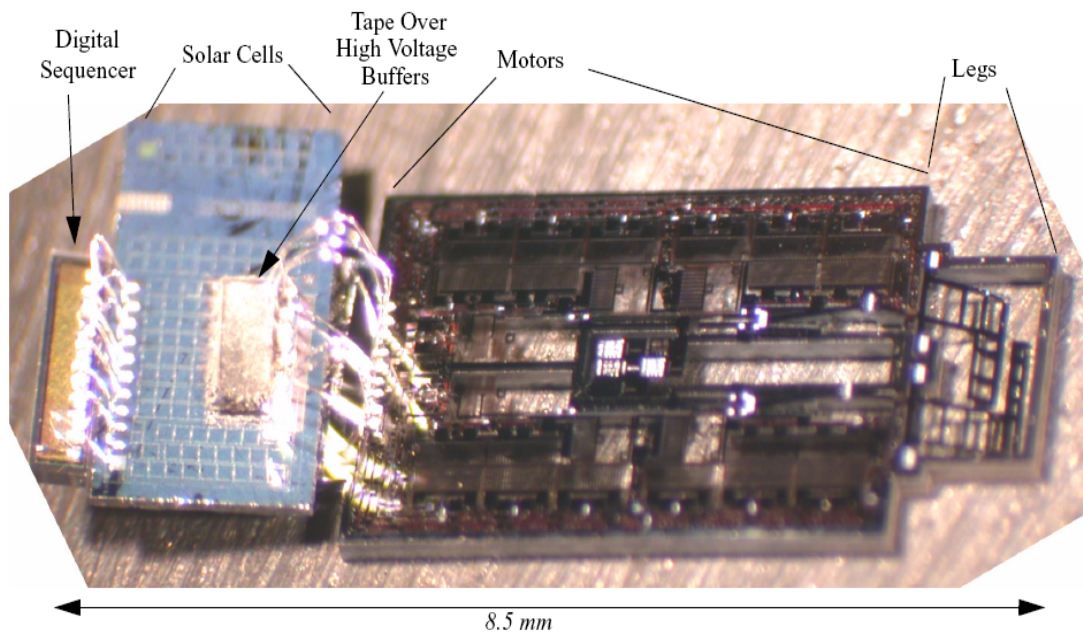


Figure 19: This 10 mg robot used a 2 mm^2 solar cell to produce an open circuit voltage over 50 V, enough to power the actuation of the electrostatic based inchworm motors [25].

To achieve the high voltage needed, 90 single solar cells were connected in series, and occupied a total area of 2 mm^2 . A small signal sequencing circuit was used to control the voltages to meet the requirements of the different processes on the robot. The robot did not walk forward as intended, but it did move laterally, rotating to the right.

2.7 Chapter Summary

In this chapter many MAV designs were reviewed, which included rotary, flapping, and airplane styles. A review of current MEMS motors and high voltage solar cell technology was also conducted. The design by Miki *et. al.* was the smallest rotary flying device measuring just over 2 mm from tip-to-tip and was powered by an alternating magnetic field. The Entomopter designed by Michelson *et. al.* looks to have the greatest potential for flapping style designs. While the Black Widow was the smallest, most advance airplane style design, having a wing span of only 6 inches.

As for the review of micromotors, the largest rotational frequency came from the microengine by Sniegowski and Garcia. The microengine was able to turn multiple gears at a rate of 200,000 RPM. The smallest integrated high voltage solar cell was done by Hollar *et. al.* and generated 90 V with an area of only 2 mm^2 .

This concludes the Literature Review of current MAVs and some of the enabling technology they have incorporated. In the next chapter, relevant theories of operation for MAVs will be discussed.

III. Theory

3.1 Chapter Overview

The purpose of this chapter is to discuss the relevant theories of flying millimeter scale robots. An important topic that needs to be covered is the theory of aerodynamics on the millimeter scale. From the analysis of aerodynamics, a rotor could be designed which can generate the required force to lift the mass of the entire structure. The method used to turn the rotor could come from several different mechanisms; there are many avenues that could be taken to achieve this objective.

Since the PolyMUMPs and SUMMiT V processes are readily available commercial MEMS fabrication foundries; a brief description of the layer structure for each process will be presented before specific designs are discussed. Having a clear understanding of the specific fabrication process will clarify some of the design intricacies presented later.

Circular scratch drives, electrostatic motors, comb drive resonators or micro-engines are all potential mechanisms to drive the rotors. So the next important topic in this section will be the theory of operation for each of the potential drive mechanisms previously mentioned. Each prospective drive mechanism will be analyzed to determine its potential maximum rotational frequency and the torque it can produce. Suitable driving mechanisms for the millimeter sized robot are discussed in depth beginning in Section 3.5.

Rotor blade deflection is a critical parameter for a rotary micro air vehicle. The theory for residual stress between Poly2/gold in the PolyMUMPs process will be

analyzed to predict vertical deflection of rotor blades. Finally in this chapter, a vision of the MAV will be presented.

3.2 Aerodynamics

To gain a better appreciation for flight on the millimeter-scale, it is beneficial to briefly review the principles of flight for macro scale air vehicles such as planes and helicopters. The basic airfoil used on airplanes is illustrated in Figure 20. As the wing moves through the air, the flow of air is divided at the leading edge and goes over either the top or bottom of the wing. Air particles that were divided on the leading edge want to meet up again at the trailing edge of the wing. For the air particles to meet again at the trailing edge, the particles that flowed over the top surface have to move faster because they have a larger distance to cover due to the top curvature of the wing. Based on Bernoulli's Principle, the increased velocity causes separation between the particles which reduces the air pressure over the top of the wing. Particles under the wing move in a relatively straight line and experience less displacement, therefore, the relative velocity and pressure of the air particles remains the same. The pressure differential between the top and bottom of the wing provides the lift force for the standard airfoil.

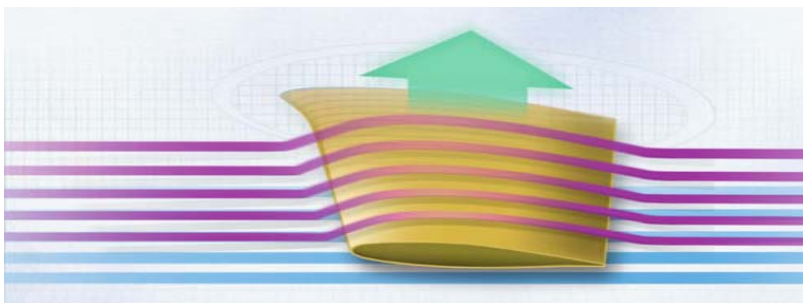


Figure 20: Example aircraft wing shows the flow of air over the airfoil. The reduced pressure on the top surface of the wing generates lift. [26].

The typical airfoil, used for modern day flight as described in the previous paragraph, depends on the laminar flow of air. Too much turbulence in the air over the wing would result in a reduction of the amount of lift produced. As the speed of the wing through the air increases, the amount of lift generated also increases; assuming the wing maintained the same angle of attack. Airplane style craft thrust-to-weight-ratios can be less than one, because the wings provide the lift force opposing gravity and the propellers pull the aircraft forward through the air. In helicopter style designs, the thrust to weight ratio needs to be greater than one.

The size and shape of an airfoil play a critical role in how it generates lift. In the case of rotary wings, the radius of the blade and chord length are two of the important factors. The Reynolds chord number is the ratio of inertial forces (ρv) to viscous forces (μ/c) for airfoils traveling through a fluid and is given by

$$\text{Re}_c = \frac{\rho v c}{\mu} \quad (1)$$

where ρ is the density of air, v is the mean velocity of the airfoil through the fluid, c is the chord length, and μ is the dynamic fluid viscosity. The density of air and the dynamic fluid viscosity are constant values for a given altitude and humidity level. The designer has control over two of the parameters, the velocity through the air and the chord length. Figure 21 shows a plot of the Reynolds number verses mass for various aircraft. At very low Reynolds numbers, the wing tip vortices and turbulent effects over the wing play an important role in generating lift [27].

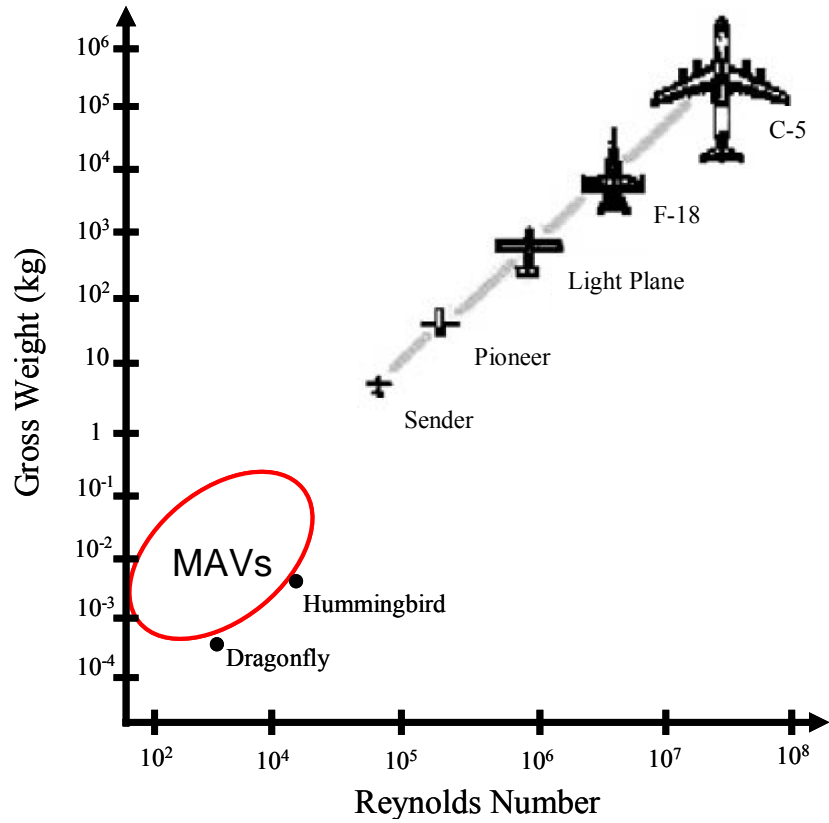


Figure 21: Plot shows the mass of the aircraft versus Reynolds chord number for a vast range of air vehicle types [28].

The thrust generated by a rotary design micro air vehicle can be describe as

$$T = \frac{2}{3} \pi^2 \rho b c f^2 R^3 (C_l + \phi C_d) \quad (N) \quad (2)$$

where ρ is the density of air, b is the number of rotor blades, c is the chord length, f is the frequency of rotation, R is the radial length of the rotor blade, C_l is the coefficient of lift, ϕ is the induced angle, and C_d is the coefficient of drag [1]. Through experimental findings done by Miki *et. al.*, the $(C_l + \phi C_d)$ term remained relatively constant at 1.4 for rotor blades with a radius of 4.5 to 8 mm [1]. For designs with a 4 mm or less radius, the $(C_l + \phi C_d)$ term varied, it increased and then decrease. It was determined that the term

increased due to vibrations in the setup. The $(C_l + \phi C_d)$ term was found to be 0.74 for the flight mechanism shown in Figure 1. Most likely the $(C_l + \phi C_d)$ term will decrease even more for smaller rotor designs.

Another interesting comparison that should be analyzed is the relative vehicle mass, radius, and rotational rate or rotors for different sized helicopters. Table 2 illustrates a comparison of the three previously mentioned parameters. Scaling down in size from the Chinook helicopter, to the Xcell-60, to the design done by Miki *et. al.*, the required rotational rate increased an order of magnitude each time. The mass was reduced by almost 1,400 times from the Chinook to the Xcell-60 and 2.3 million times lighter from the Xcell-60 to the Miki design. While the radius of the rotors decreased an order of magnitude from the Chinook to the Xcell-60 and two orders of magnitude from the Xcell-60 to the Miki design. When scaling down the size to smaller flying vehicles, the mass must be greatly reduced and the frequency of rotation must be increased.

Table 2: Comparison of mass, radius, and rotational frequency for three different helicopter designs.

	Mass (kg)	Rotor Radius (m)	Frequency (Hz)
Chinook Helicopter	11,340	9.144	3.75
Xcell-60 RC Helicopter	8.16	0.762	28.33
Miki 2.5 mm design	0.0000035	0.0025	500

3.3 PolyMUMPs Process

PolyMUMPs, a commercial fabrication process, is a three-layer polysilicon surface micromachining method which is available to universities and professionals in industry. Seven masks are used to define the different layers or features in the PolyMUMPs process. Figure 22 is a cross-section of an electrostatic motor with the

various layers and thickness labeled. The top two layers are releasable, meaning they can be free standing after the sacrificial oxides are removed, while the bottom layer is always connected to the surface of the wafer. The PolyMUMPs fabrication process is a cost effective means of producing proof-of-concept MEMS devices. A basic overview of the fabrication sequence will be covered to create a better understanding of the MEMS structures presented later in this document.

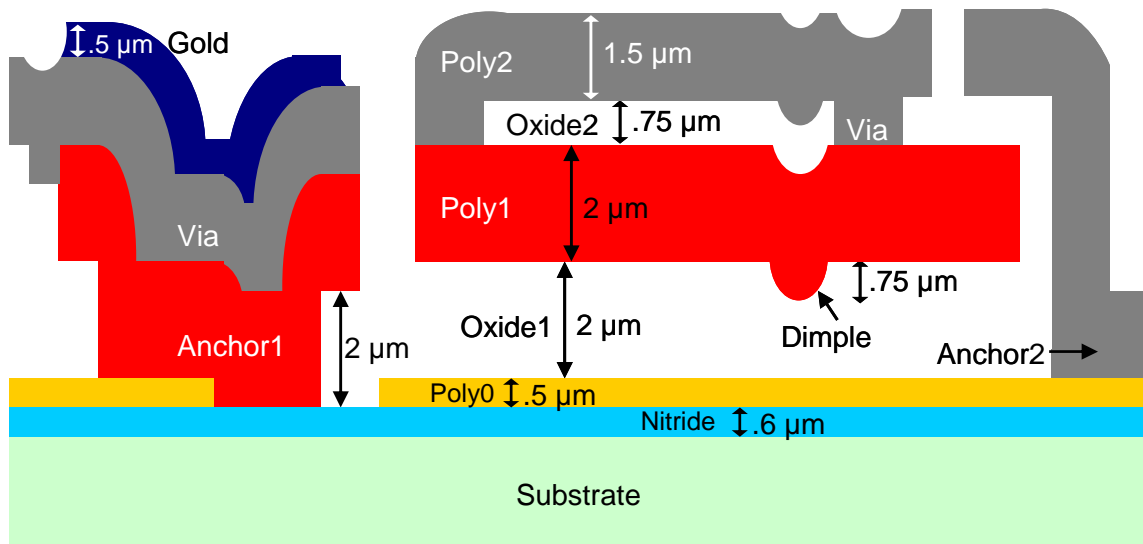


Figure 22: Cross-section of an electrostatic motor design illustrating the various layers and thicknesses.

The fabrication process starts with a clean 100 mm diameter, (100) orientation n-type silicon wafer. First, a 0.6 μm layer of silicon nitride is deposited via low pressure chemical vapor deposition (LPCVD), which acts as an electrical insulating layer. Next, a 0.5 μm layer of polysilicon, called Poly0, is deposited on top of the nitride. Standard photolithographic steps are carried out using the Poly0 mask to define where the Poly0 layer will remain by covering those regions with photoresist. Then the unwanted regions of Poly0 are removed via etching in a reactive ion etch (RIE) system. The next step is to

deposit, via LPCVD, a 2 μm layer of phosphosilicate glass (PSG), which will be used as a sacrificial layer called Oxide1. The wafer is then annealed for one hour at 1050 $^{\circ}\text{C}$ in argon. The wafer is annealed to allow the phosphorous atoms in the PSG to diffuse into the Poly0 layer, reducing the Poly0 resistance.

Two mask and etch steps are then completed to remove portions of Oxide1 where the Dimples are formed followed by an Anchor1 etch. The Dimple etch removes a 0.75 μm deep portion of the oxide layer while the Anchor1 etch removes the entire thickness of the Oxide1 layer to provide an attachment location for the Poly1 structural layer. The next step is to deposit a layer of polysilicon called Poly1. Then a 0.2 μm layer of PSG is deposited on top of the Poly1 and the wafer is annealed again for one hour at 1050 $^{\circ}\text{C}$ in argon. Doping the polysilicon using PSG and annealing causes dopant level gradients and produces internal stress in the polysilicon layers. The thin 0.2 μm PSG layer is then masked with the Poly1 mask, to form a hard mask for the Poly1 RIE etch.

After the Poly1 etch is complete, a 0.75 μm layer of PSG is deposited called Oxide2 and again the wafer is annealed. Two more etches are possible over Oxide2, the Poly1_Poly2_Via etch or the Anchor2 etch. The Poly1_Poly2_Via is used to remove Oxide2 and the Anchor2 etch is used to remove both Oxide1 and Oxide2. Now, the last polysilicon layer is deposited, called Poly2. Again the 0.2 μm layer of PSG is deposited on top of Poly2, annealed and then acts as a hard mask for the Poly2 etch.

The final steps of the process are to remove the 0.2 μm layer of PSG and lithographically pattern the wafer for metal deposition. A 0.5 μm layer of gold is evaporated onto the wafer and then metal liftoff is accomplished to remove the unwanted

portions of metal. The metal will only adhere to the surface of Poly2, making it the only layer it can be placed on [29].

The wafers then have a protective coating of photoresist applied so the wafers can be diced into 1 cm by 1 cm chips. Users of the PolyMUMPs process receive 15 nearly identical copies of the original design that was submitted approximately two months prior.

Once the chips are received, they are typically sent out again to be sub-diced into smaller chips. Depending on the number of people that submitted designs, chips have been typically sub-diced into: quarters, ninths, sixteenths, or twenty-fifths. Chips smaller than a third of a centimeter prove difficult to handle.

Releasing the MEMS structures is a straight forward process. First the chips are washed with acetone in two different containers for 5-10 minutes, which removes the protective photoresist layer from the factory. The chips are then placed in a 48 % concentration solution of hydrofluoric acid (HF) to remove the two sacrificial layers, Oxide1 and Oxide2. The etch time in HF ranges between 1 ½ to 5 minutes, depending on the lateral distance under a sheet of polysilicon that needs to be etched. At this point the MEMS structures in Poly1 and Poly2 have been fully released and the chips need to be placed in deionized (DI) water to stop the etching process. Great care must be taken in handling the chips, too much agitation in the liquids will result in the MEMS structures being ripped off the surface. After five minutes in the DI water they are placed in either isopropyl or methanol for the drying process.

Two common drying methods are used on MEMS structures, baking the chips on a hot plate or placing them in a CO₂ critical point dryer. Isopropyl is used if the chips are to be dried on a 110 °C hotplate for 10-15 minutes. Methanol is used if the chips are going to be dried in the CO₂ dryer, which takes about 40 minutes per run. The critical point dryer typically does a better job drying MEMS chips, stiction is reduced and the chip surfaces are cleaner.

3.4 SUMMiT VTM Process

The SUMMiT VTM (Sandia Ultra-planar Multi-level MEMS Technology V) process is a five-layer surface micromachining fabrication process available to universities and industrial companies. The SUMMiT VTM process uses 14 masks to define the polysilicon and oxide layers which are shown in Figure 23.

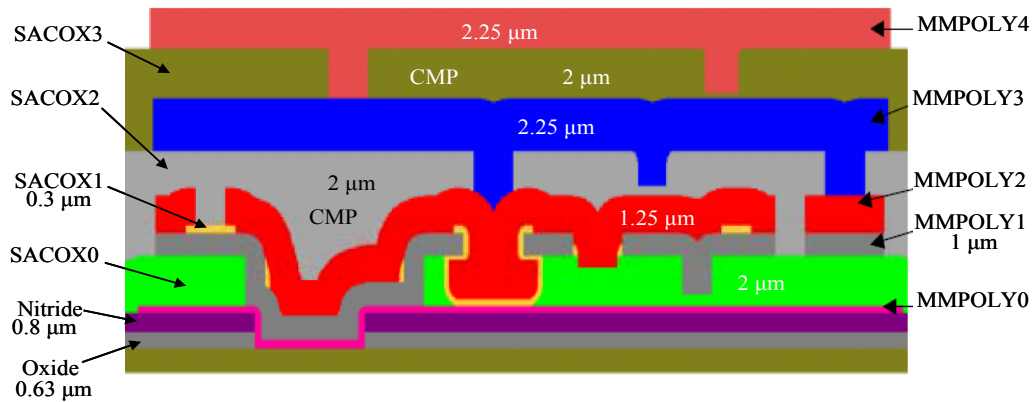


Figure 23: The cross-section of the SUMMiT VTM fabrication process shows some of the realizable structures [30].

There are four total releasable layers and the one layer which is always connected to the surface of the wafer. The polysilicon layers are deposited starting with MMPOLY0 and ending with MMPOLY4. The sacrificial oxide layers are named

SACOX1 through SACOX4. Two insulating dielectric layers are deposited initially, a 0.63 μm thermal oxide followed by a 0.8 μm layer of silicon nitride. The thicker dielectric layers allow for a higher breakdown voltage, which allows the devices to operate at higher voltages than in the PolyMUMPs process.

The large improvement made in the SUMMiT VTM process has been the planarization of the top two oxide layers. The top two oxide layers are planarized using a chemical mechanical polish (CMP) method developed at Sandia labs. This process has relieved the top two layers from the underlying topography, allowing for more free movement in those layers.

There are some notable differences between the PolyMUMPs and SUMMiT fabrication processes. In the SUMMiT process the polysilicon layers are most likely deposited via some type of chemical vapor deposition method where the dopant is added in-situ. This method of polysilicon crystal growth creates a very low internal stress, making the top two layers extremely flat. There is no metal layer available in the SUMMiT V process. Some post processing would be required if a metal layer needed to be added. The sacrificial oxide layers in the SUMMiT V process are much harder than the PolyMUMPs oxide layers. Over an hour in HF acid is required to free the releasable layers in the SUMMiT V process [30]. Pin joints can be made where MMPOLY2 is backfilled under the underlying MMPOLY1 layer, making gear designs easier to layout.

The SAMPLES (Sandia Agile MEMS Prototyping Layout Tools, Education and Services) program produces 100 identical modules, which are 2.8 x 6.3 mm². The price

is now \$11,200 for the design module space with the additional cost of \$1,000 to release and dry half of the samples.

3.5 Circular Scratch Drives

Circular scratch drives or rotary scratch drive actuator (SDA) motors operate at voltages ranging from 30-150 V [4]. The scratch drive in Figure 24 was drawn in L-Edit, with the primary components and the normal direction of rotation identified. The drive signal is passed to the rotating portion of the SDA using the outer ring of Poly0. The outer circle and inner circle ride on a thin ring of polysilicon created by the dimple etch, to minimize friction over the Poly0 layer. The substrate is connected to ground by breaching the nitride layer and creating a probe pad contact of Poly2 and gold.

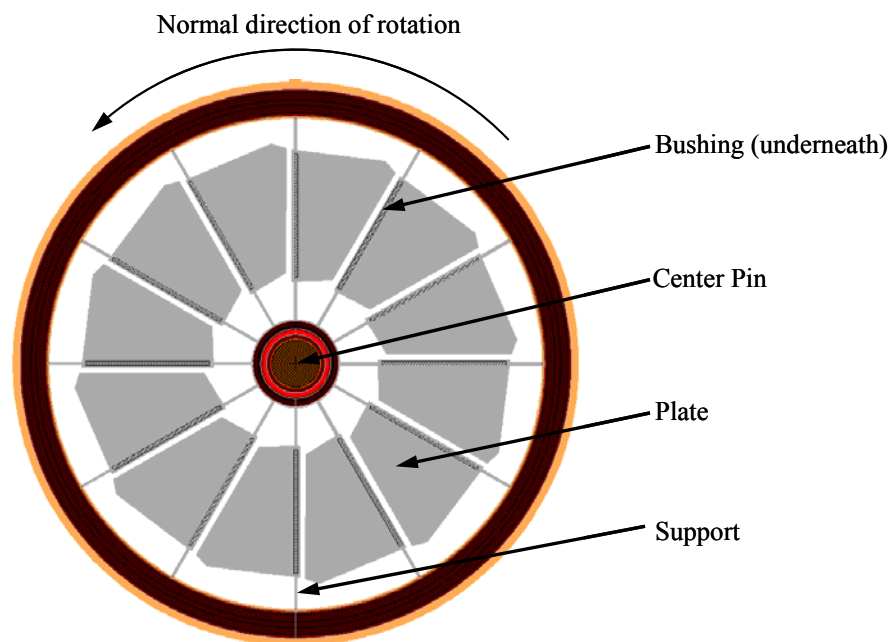


Figure 24: Scratch drive actuator drawn in L-Edit identifies the primary components and the normal direction of rotation.

Figure 25 shows a three dimensional view of a SDA plate, bushing, and support arm. When the scratch drive is being actuated, the positive charged plates are attracted to the grounded substrate. The nitride layer acts as an insulator ensuring the charge interaction between the plate and the substrate is capacitive in nature. As the stepping voltage reaches the maximum, the bushing is pushed forward slightly as illustrated in Figure 26. As the voltage decreases, the bushing returns to its normal shape, pulling the SDA around. When the driving voltage oscillates between the priming and stepping voltages very rapidly, the SDA rotates. The higher the driving frequency, the faster the SDA will rotate until it reaches its limit where it will then cease functioning. The maximum frequency of operation is believed to be due to squeeze-film dampening effects [4].

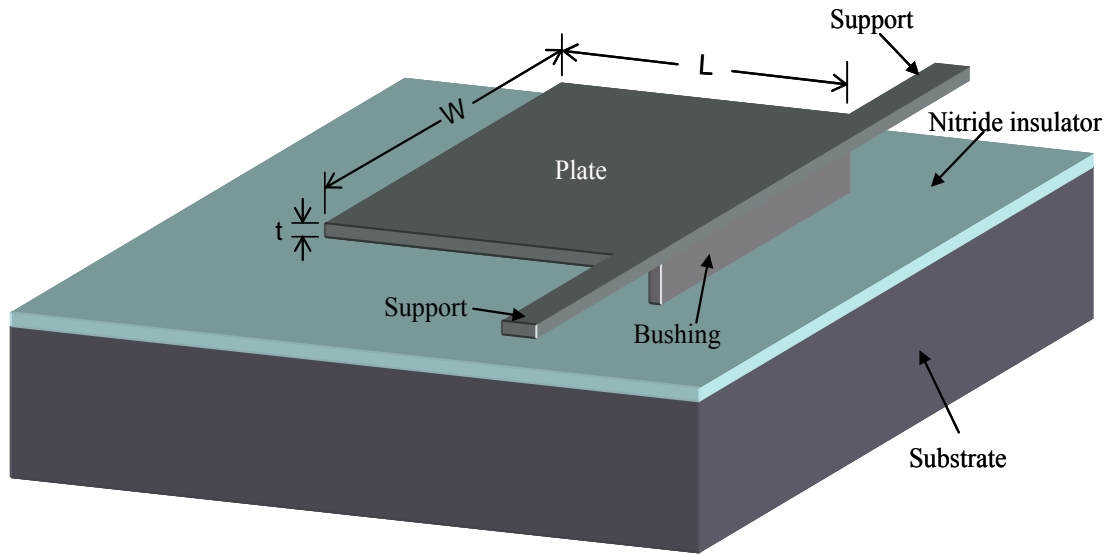


Figure 25: The typical structure of a scratch drive actuator plate is pictured with important regions labeled.

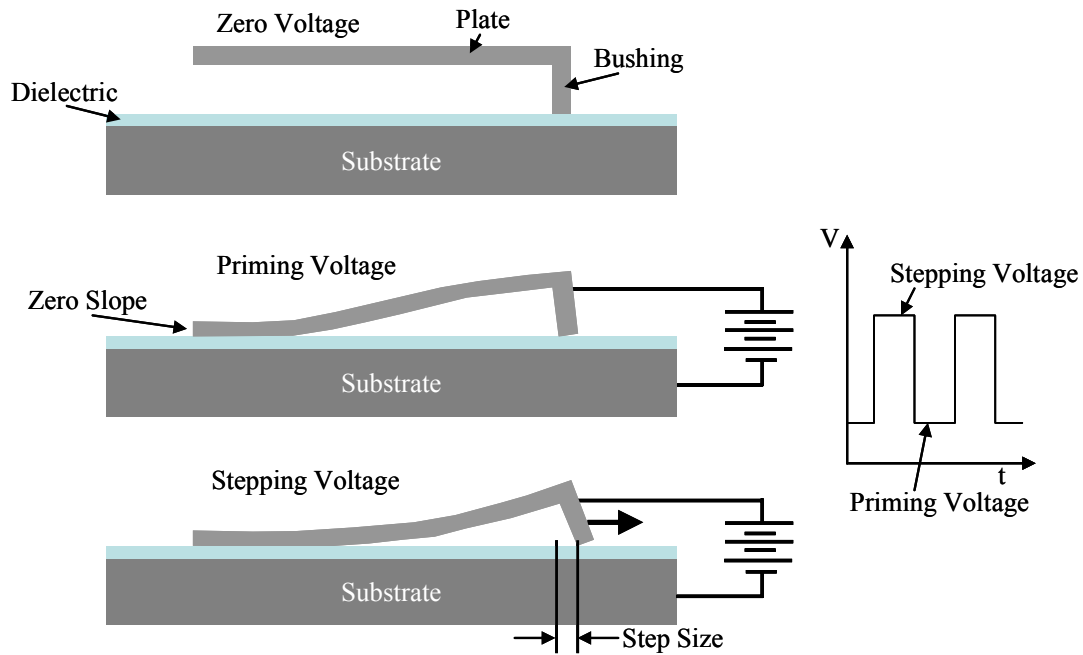


Figure 26: Shows the cross-sectional view of operation for the SDA. For forward motion, the drive signal operates between the priming voltage and stepping voltage [4].

3.6 Electrostatic Motor Design

Two different electrostatic motors will be discussed here, one available through the PolyMUMPs process and the other through the SUMMiT V process. The amount of capacitive interaction plays a large role in the required drive voltage. The PolyMUMPs motor is limited to having a planar design, and can only have an exterior electrode height of $3.5\ \mu\text{m}$. Planar motors, like the one pictured in Figure 27, operate at very high voltages ranging from 150 to 300 V. A similar design could be created in the SUMMiT V process where the exterior electrode height could be over $9\ \mu\text{m}$. The required drive voltage would be much lower than a similar design done in PolyMUMPs process.

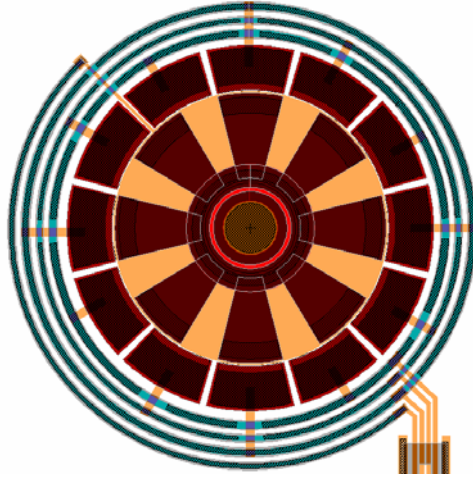


Figure 27: Planar electrostatic motor designed in the PolyMUMPs process. The capacitive interaction to cause rotation only occurs at the electrode-stator interface where the thickness of the electrode is 3.5 μm thick.

The multi-stator motors fabricated by Krygowski *et. al.* rotated with a drive potential less than 6 V, meaning the forces of friction in the hub were very low [21]. That was accomplished by using four sets of exterior stators, not just one. The amount of area for capacitive interaction was greatly increased.

The torque produced by an electrostatic motor is

$$\tau(\theta) = \frac{1}{2} V^2 \frac{d}{d\theta} C(\theta) \quad (3)$$

where τ is the generated torque, V is the applied voltage, and $dC(\theta)/d\theta$ is the derivative of the capacitance C with respect to the angle θ of overlap. The capacitive increase between the stator and rotating electrode is given by

$$C(\theta) = -n \frac{2t\theta\epsilon_0}{\ln\left(\frac{r_2}{r_1}\right)} \quad (4)$$

where t is the thickness of the rotating electrode, n is the number of electrodes, ϵ_0 is the permittivity of air, r_2 is the radius of the stator, and r_1 is the radius of the rotating electrode. To create a flying system, the motor must be able to generate enough torque to overcoming frictional force in the motor and turn an attached rotor.

3.7 Comb Drive Resonators

Comb drive resonators operate on the basic principles of a spring/mass system. The comb fingers on either side of the device use capacitive forces generated between the center resonator comb and the side comb fingers by a difference in potential voltage between them. The electrostatic force of attraction between the combs causes a displacement of the shuttle in the x-direction equal to the restoring force of the springs. A simple comb drive resonator is pictured in Figure 28 where the key features are identified. Anchor points connect the polysilicon layers to the substrate and the rest of the areas are free to move above the substrate surface.

To predict comb drive operation effectiveness, all controllable parameters must be considered to include: the spring system dimensions, shuttle mass, number of comb fingers, and structure thickness. All of these parameters play an important role in the operating frequency of the resonator. First the spring system will be discussed. To simplify the analysis, it will be assumed that each of the springs in the comb drive will be treated as a fixed end cantilever with the opposite end free with an end load force acting on it in the x-direction. Figure 29 is an illustration of the simple cantilever labeling the important dimensions.

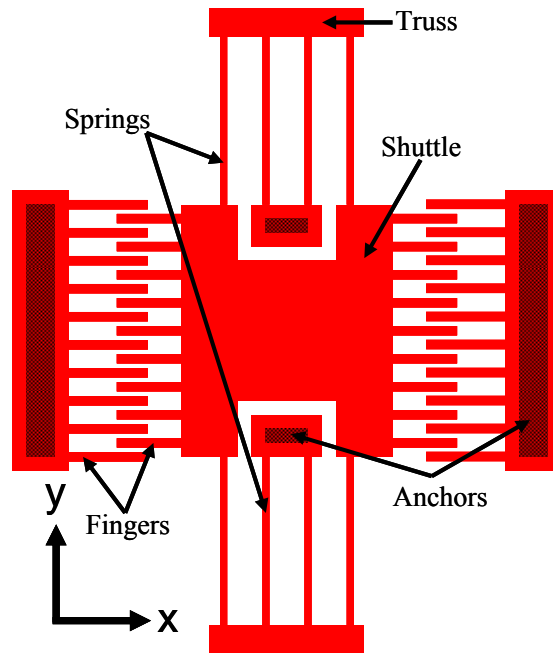


Figure 28: Simple illustration of comb drive resonator parts where the shuttle is able to move laterally in the x-direction.

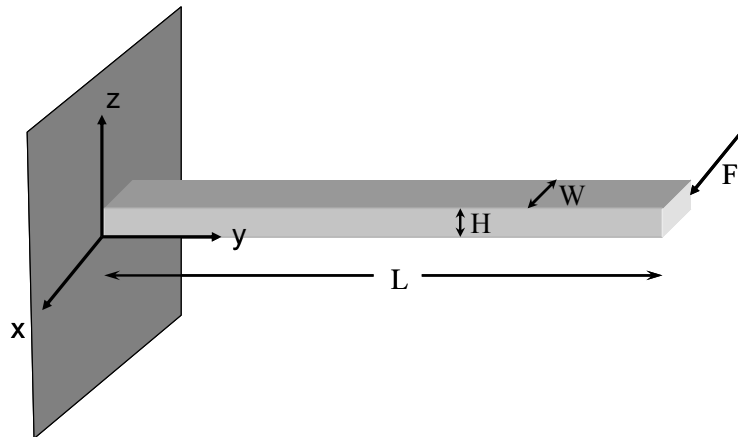


Figure 29: Simple cantilever with a fixed end on the left and a load force F acting in the x-direction on the free end.

The spring constant k for this cantilever is

$$k = \frac{3EI}{L^3} \quad (\text{kg/s}^2) \quad (5)$$

where E is Young's Modulus, I is the moment of inertia in the center of the beam parallel to the z -axis and L is the beam length. The variable I_z is defined as

$$I_z = \frac{w^3 t}{12} \quad (\text{m}^4) \quad (6)$$

where t is the thickness of the material, and w is the width of the beam. Substituting Equation (6) into Equation (5) leads to

$$k = \frac{E w^3 t}{4 L^3}. \quad (7)$$

Equation (7) then defines the spring constant for one spring in the comb drive resonator. Since there are a total of eight springs in the basic comb drive shown previously in Figure 28, the total spring constant for the system is

$$k_{\text{total}} = \frac{2 E w^3 t}{L^3}. \quad (8)$$

The critical dimensions of the comb fingers are illustrated in Figure 30. The capacitive force generated between the fingers can be expressed as

$$F = \frac{1}{2} \frac{n t \epsilon_0 \epsilon_r V^2}{g} \quad (\text{N}) \quad (9)$$

where n is the number of comb fingers on one side, t is the thickness of the fingers, g is the gap between neighboring fingers, ϵ_0 is the permittivity of free space, ϵ_r is the relative permittivity of air, and V is the applied voltage difference between the combs. The gap between the fingers is limited by the achievable resolution of the fabrication process. For example, the minimum feature spacing for the PolyMUMPs and SUMMiT V process is $2 \mu\text{m}$ and $1 \mu\text{m}$, respectively. The capacitive force increases as: the layer thickness and number of fingers increase, and as the gap between the fingers decreases.

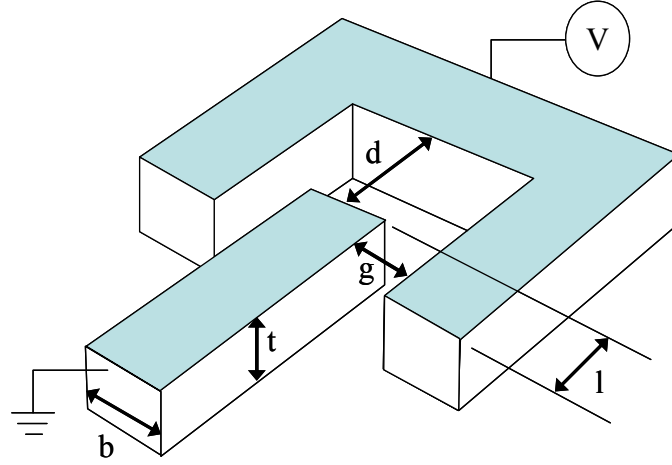


Figure 30: Relevant comb finger dimensions are labeled in the above picture. The gap between the fingers is g , t is the thickness of the material, b is the width of the fingers, l is the amount of initial overlap and d is the initial distance between the outer comb and the inner finger tip.

The force required to displace a spring a given distance is defined as

$$F = xk_{\text{total}} \quad (\text{N}). \quad (10)$$

Replacing the electrostatic force F in Equation (9) by xk_{total} , and dividing through by k_{total} , shows the displacement

$$x = \frac{1}{2} \frac{nt\epsilon_0\epsilon_r V^2}{gk_{\text{total}}} \quad (\text{m}). \quad (11)$$

Once a device has been designed and fabricated, the magnitude of the lateral displacement can be controlled by adjusting the amplitude of the voltage.

The mass of the comb drive is divided up into three sections: the main shuttle, the springs, and the folding trusses. Mass is calculated by multiplying the volume of a region by the density of the material. The volume of a region is estimated from the dimensions

taken from the L-Edit drawings multiplied by the thickness of the fabricated layers. The main shuttle mass consists of the center region and inner comb fingers. The spring mass includes just the thin beams from the center shuttle to the trusses. An accurate mass calculation is important because the mass affects the resonant frequency of operation which will be discussed next.

The fundamental resonant frequency is given by [31]

$$f = \frac{1}{2\pi} \sqrt{\frac{k_{\text{total}}}{M_p + \frac{M_t}{4} + \frac{12M_b}{35}}} \Rightarrow \frac{1}{2\pi} \sqrt{\frac{2Ew^3t}{\left(M_p + \frac{M_t}{4} + \frac{12M_b}{35}\right)L^3}} \quad (\text{Hz}) \quad (12)$$

where M_p is the mass of the main shuttle, M_t is the mass of the trusses, and M_b is the mass of the springs. The resonant frequency is important if two comb drives are coordinated to turn a gear. Knowing the shuttle displacement, frequency of oscillation, the number of teeth on the gear and tooth spacing; the frequency of rotation of the gear is easily found. For example if a gear had N teeth, the comb drive had a resonant frequency of f , and the shuttle moved n teeth per period, the gear would turn at a rate of

$$\text{Gear}_{\text{rate}} = \frac{fn}{N} \quad (\text{Hz}). \quad (13)$$

3.8 Rotor Blade Deflection

When developing a millimeter-scale robot for flight, there are two important factors that need to be considered. The first factor involves how much thrust can be generated by the rotors. The second consideration is the mass of the robot. From basic principals of physics, if the upward thrust is greater than the weight of the robot, flight

can be achieved. This section will cover the theory of achieving the desired rotor blade deflection.

Two approaches were considered to achieve the desired blade deflection in the rotor. The first method used was to take advantage of the residual stress between the Poly2 and gold layers in the PolyMUMPs process. A second approach was to use polyimide as a hinge to obtain the desired deflection as done by Miki *et. al.* [2]. In the PolyMUMPs process, the final step is depositing a 0.5 μm gold layer on top of Poly2. Metal deposition in the PolyMUMPs process is done at 383 K, which is important because the drop to room temperature is what causes the Poly2/gold beams to defect upward. Gold has a higher coefficient of thermal expansion, so it creates a large tensile force on the Poly2/gold bilayer at room temperature. The internal residual stress, σ_{int} for Poly2, is provided by the foundry process. The residual stress, σ_{res} between the Poly2/gold layers is given by

$$\sigma_{\text{res}} = \sigma_{\text{int}} + \sigma_{\text{th}} \quad (14)$$

where σ_{th} is the stress due to thermal expansion between the Poly2/gold layers. Thermal stress is given by

$$\sigma_{\text{th}} = E'_g (\alpha_p - \alpha_g) \Delta T \quad (15)$$

where E'_g is the biaxial modulus of gold, α_p and α_g are the coefficients of thermal expansion for polysilicon and gold respectively. The ΔT is the change in temperature which is the current temperature minus the fabrication temperature. The biaxial modulus for gold is defined as

$$E'_g = \frac{E_g}{1 - \nu_g} \quad (16)$$

where E_g is Young's modulus for gold and ν_g is Poisson's ratio for gold. Now the vertical deflection, $v(L)$ as a function of beam length for the Poly2/gold cantilevers can be described as

$$v(L) = \frac{3t_g \sigma_{res}}{E'_p t_p^2} L^2 \quad (17)$$

where t_g and t_p are the thicknesses of the gold and Poly2 layers respectively and L is the length of the cantilever. The biaxial modulus for polysilicon, E'_p is given by

$$E'_p = \frac{E_p}{1 - \nu_p} \quad (18)$$

where E_p is Young's modulus for polysilicon and ν_p is Poisson's ratio for polysilicon.

An analytical equation which describes the vertical deflection of a cantilever is useful to predict the amount of deflection for various beam lengths. Many of the rotor designs, which will be discussed later, are based on the Poly2/gold layer deflection. Varying the beam lengths will produce slight differences in the achievable angle of attack for the rotor designs. The results for the predicted beam and rotor blade deflections are shown in Sections 4.3 and 6.6.1.

3.9 Vision of Flying Microrobot

The vision of this research is to produce a millimeter-scale flying robot like the one pictured in Figure 31. The design would include an onboard power source, potentially a solar cell. Signal conditioning circuitry would also be required to control

the motors and sensors. The two rotor blades would need to turn in counter rotation, similar to a Chinook helicopter.

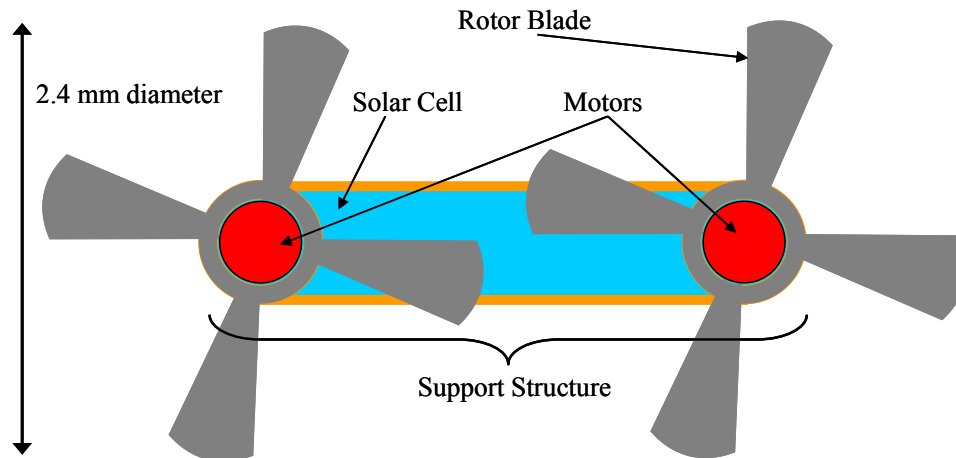


Figure 31: Double rotor concept includes solar cell and signal conditioning circuitry with the rotors placed on top of the motors.

3.10 Conclusion

In this chapter, some of the relevant theories of flight on the micro scale have been discussed. Aerodynamics for low Reynolds number aircraft and rotor blade speed were addressed. The PolyMUMPS and SUMMiT V fabrication processes were also compared, showing the SUMMiT V process had greater capabilities but at nearly four times the price.

Three different types of motors were analyzed as potential driving mechanisms to turn rotors: circular scratch drive actuators, electrostatic motors, and comb drive resonators. The four stator bank electrostatic motor fabricated in the SUMMiT V process appears to be the most promising since the torque produced increased proportionally with voltage squared; the motor will likely need to operate at upwards of 10-30 V range to turn

an attached rotor. In addition, the microengine fabricated in the SUMMiT process was also very promising because of its high rate of rotation, over 200,000 RPM.

The principles of residual stress in the PolyMUMPs process were applied to achieve rotor blade deflection. Finally a vision of a flying microrobot was presented which would be capable of independent flight. The next chapter, Modeling and Simulation, will simulate comb drives and rotor blade deflection in finite element software and numerical analysis of thrust generation calculations.

IV. Modeling & Simulation

4.1 Chapter Overview

An important part of creating MEMS structures is being able to predict the performance through computer simulations and mathematical models. CoventorWare 2005 is a finite element modeling (FEM) software program used to analyze MEMS devices. The two primary structures that are able to be modeled in this research using CoventorWare are the comb drive resonators and deflection of the Poly2/gold layer rotor blades. Some mathematical calculations are also done to predict the lift generated by different rotor blade designs based on the basic dimensions and frequency of rotation. The following sections will cover comb drive resonator performance, rotor blade deflection, and finally, thrust generation of different rotor blade designs.

4.2 Comb Drive Analysis

The primary concerns that will be addressed for the comb drive resonators are values for the spring constants and the electrostatic force generated in the comb fingers. These values are directly related to the amount of achievable lateral displacement in the shuttle. The comb drive equations from Chapter 3 are used to calculate the numerical results which are summarized in Table 3. Equation (8) is used to determine the spring constant for the comb drive system. Equation (9) determines the electrostatic force generated by the inter-digitized comb fingers, and lastly, the predicted shuttle displacement can be calculated by Equation (11). The detailed calculations can be found in Appendix D. The goal is to achieve at least 7 μm lateral shuttle displacement from center.

Table 3: Analytical values for comb drive spring constant, electrostatic force and shuttle displacement.

	Spring Constant (kg/s ²)	Electrostatic Force @ 200 V (μN)	Shuttle Displacement @ 200 V (μm)
Large stacked Poly1/Poly2 comb drive	0.817	7.44	9.1

The L-Edit layout of the large stacked Poly1/Poly2 comb drive used in the above calculations is shown in Figure 32. The L-Edit file needed to be imported into CoventorWare. Numerous attempts were made to import the file without simplification, to keep the model as accurate as possible, but a quality mesh could not be achieved. For computational purposes the L-Edit layout had to be simplified. Anchors, dimples and etch holes were removed prior to importing the drawing into CoventorWare.

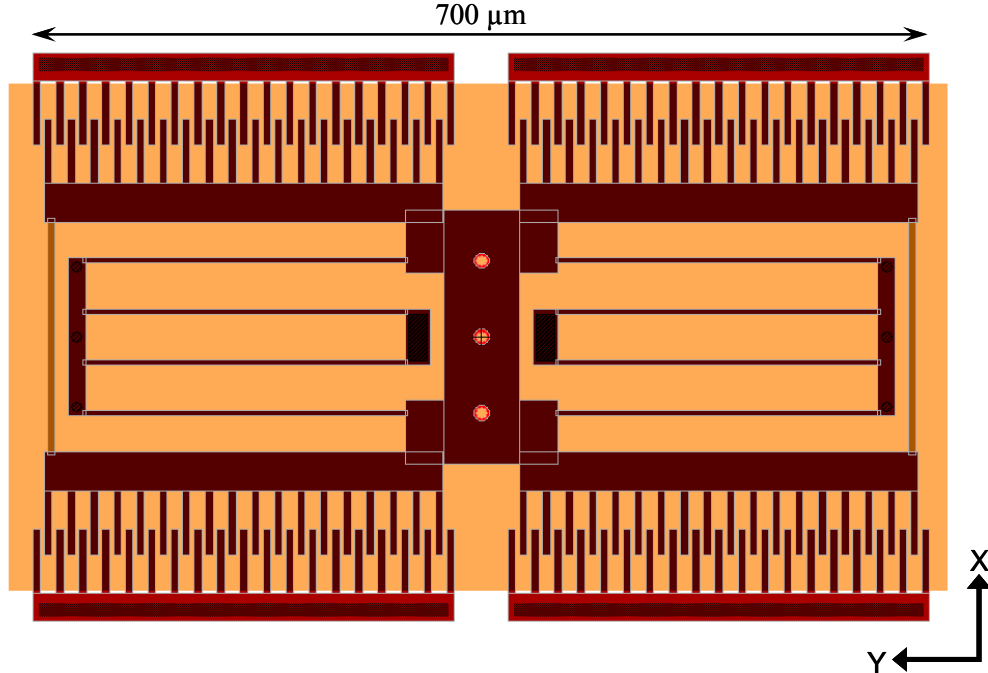


Figure 32: L-Edit drawing of the large Poly1/Poly2 comb drive resonator with stacked comb finger and spring system.

Once the simplified version of the comb drive was imported, the Manhattan brick mesh was easily implemented in the preprocessor program; the result of the mesh is shown in Figure 33. The mesh was done with resolution $(10,10,2) \mu\text{m}$ in the (x,y,z) directions. This is similar to the resolution used in the next section for the analysis of cantilever beam deflection.

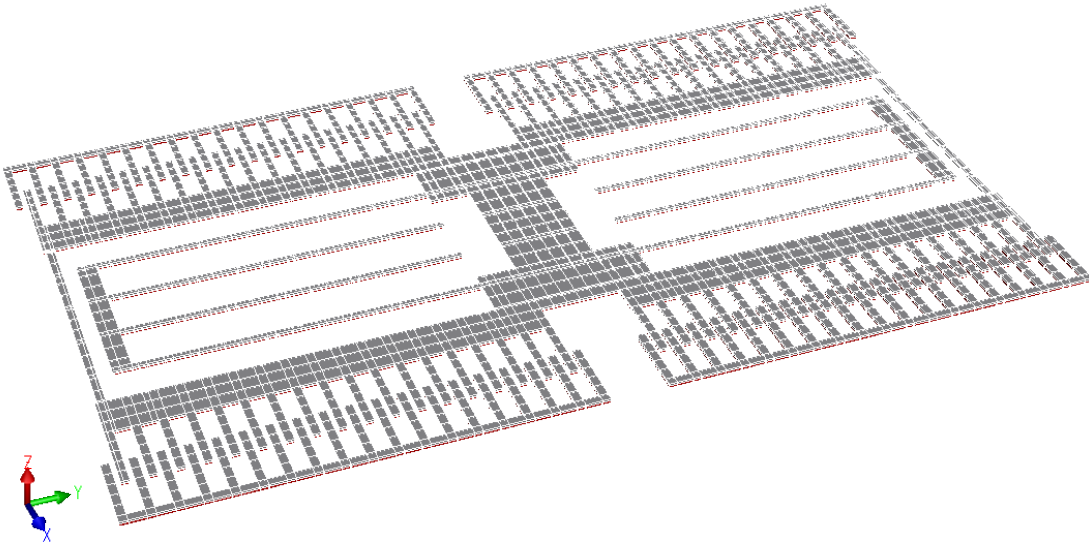


Figure 33: The Manhattan bricks mesh was applied to the large Poly1/Poly2 comb drive with resolution $(10, 10, 2) \mu\text{m}$ in the (x,y,z) directions.

The mesh file is then opened with CoSolvEM in CoventorWare, which implements electrostatic and mechanical boundary conditions. Voltages are applied to the two exterior combs on one side, ranging from zero to 250 V, in 50 V increments. The CoSolvEM program runs for approximately three hours, stepping through the six increments in voltage. An example of the results taken from the CosolvEM simulation is shown in Figure 34. When the exterior combs on one side were held at a 200 V potential, the shuttle was displaced $7.2 \mu\text{m}$.

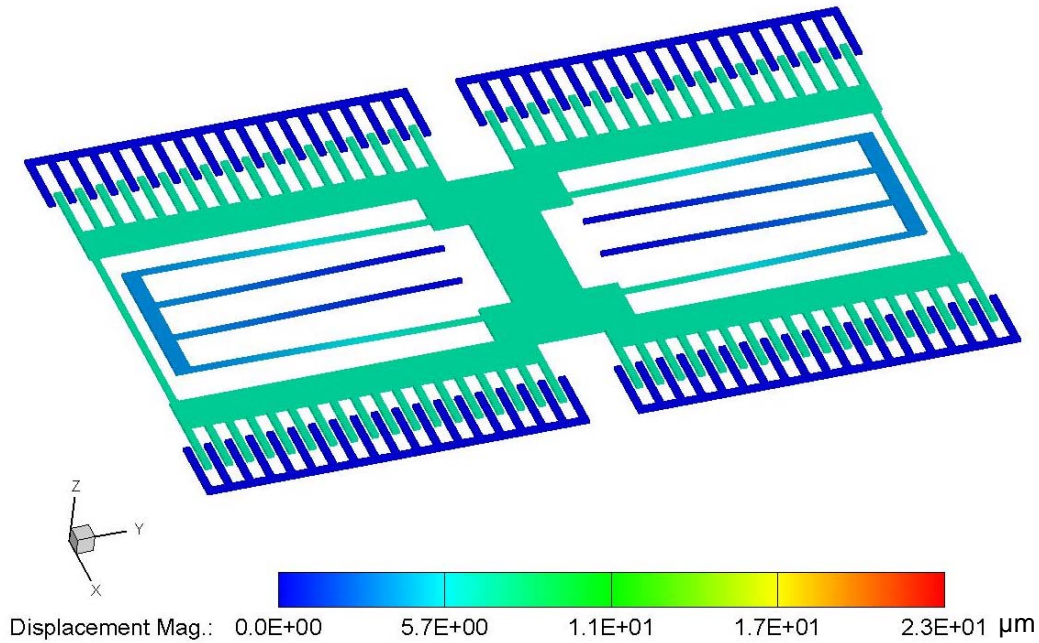


Figure 34: Results of the CoSolvEM simulation for the large Poly1/Poly2 comb drive resonator shows a lateral shuttle displacement of $7.2 \mu\text{m}$ when 200 V are applied to the bottom two out combs.

A comparison of the shuttle displacement FEM and analytical model results are shown in Figure 35. The two models are in very close agreement up to 75 V, after which the shuttle displacement predictions start to slowly diverge. At 200 V, the analytical model predicts 26.4 % more displacement will be achieved than the FEM. To achieve the desired goal of at least $7 \mu\text{m}$ shuttle displacement, the predicted operating voltage ranged from approximately 180 to 200 V. The modeled predictions will be compared to the experimental results for the comb drives in Section 6.5.

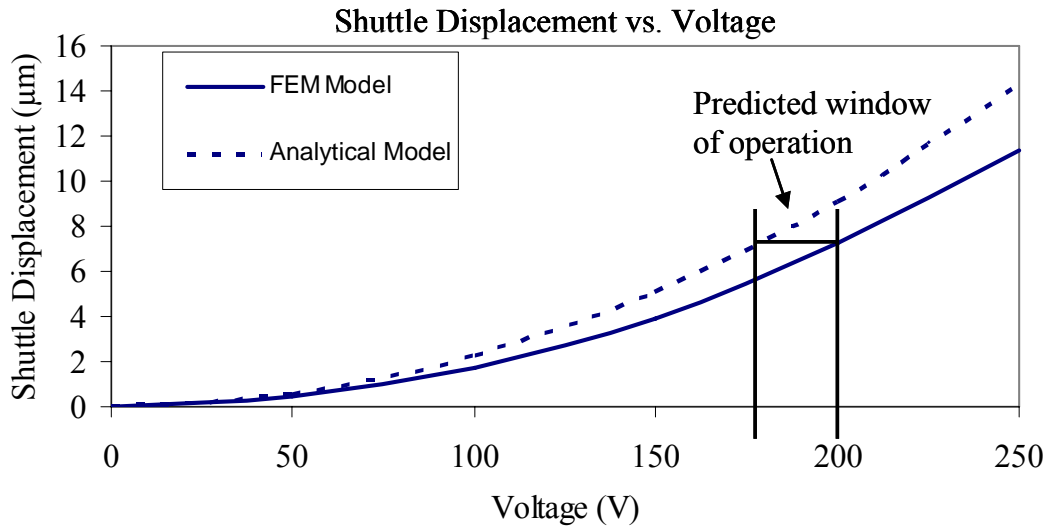


Figure 35: Lateral shuttle displacement as predicted by the CoventorWare FEM and the analytical equations for the large comb drive resonator. The predicted window of operation to achieve 7 μm of lateral displacement ranged from 180 V to 200 V.

4.3 Rotor Blade Deflection

The rotor blade designs attempt to make use of the residual stress between the Poly2/gold layers. This section compares the FEM and analytical model of bending due to residual stress between two different materials. First, simple Poly2/gold cantilever designs are modeled to obtain a basic framework of the deflection. CoventorWare 2005 is used to analyze the Poly2/gold beams shown in Figure 36. The cantilevers shown in Figure 36 have a length of 50 μm to 250 μm in 50 μm intervals. The mesh resolution used for this example was (10, 10, 5) μm which makes for fast, accurate simulations.

All the material properties given by the PolyMUMPs process were entered into the FEM software. Many simulations were conducted where the stress of the gold layer was varied until the simulated results matched the experimental data. The simulated results very closely match the experimental data, but the software had to be “calibrated”

to achieve these results. It was found that the stress in the gold layer had to be 6.1 times the value given by the PolyMUMPs fabrication data to make the modeled data match the experimental results.

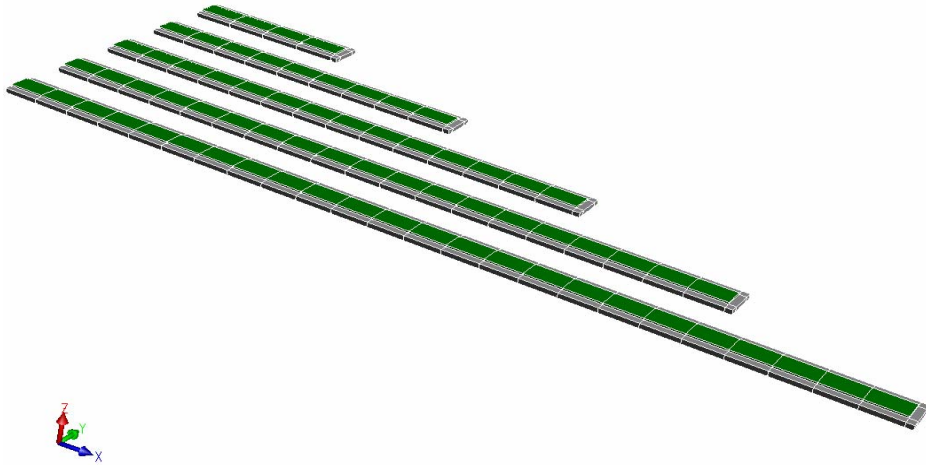


Figure 36: A sparse 3-D mesh model of cantilever beams with a resolution of (10, 10, 5) μm in the (x,y,z) directions.

The result of this simulation is shown in Figure 37. There are many variables or combinations of variables which could have been modified to achieve the desired results, but for simplicity only the stress in the gold layer was modified.

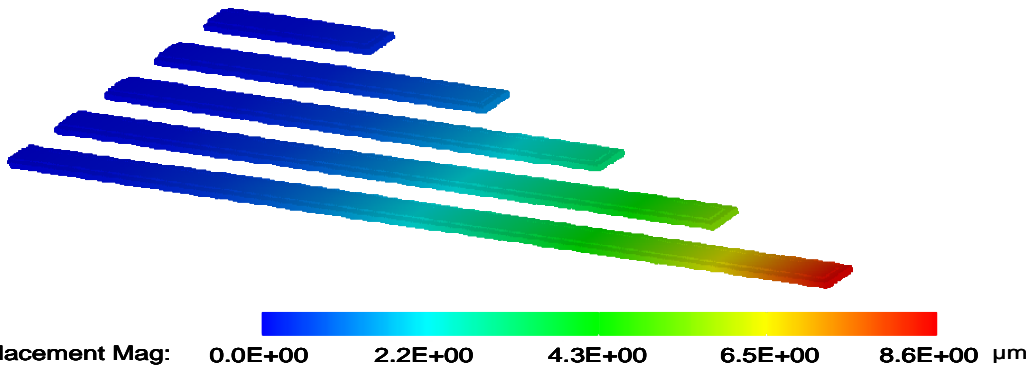


Figure 37: CoventorWare simulation shows the vertical deflection of Poly2/gold beams of various lengths ranging from 50-250 μm at increments of 50 μm .

Now that the FEM software has been calibrated, the various wing designs can be modeled. Figure 38 shows the five different rotor blade designs, drawn in L-Edit and later fabricated in the PolyMUMPs process.

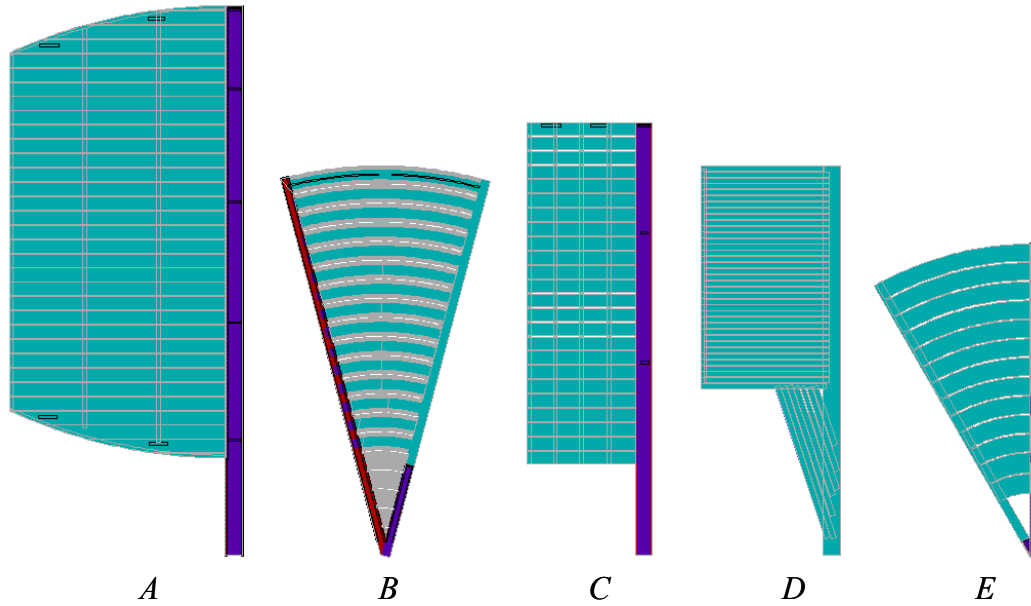


Figure 38: These are the five wing designs that were fabricated using Poly2/gold in an attempt to achieve the desired deflection.

Rotor blade model-*A* from Figure 38 was imported into CoventorWare first, however, a decent mesh model could not be completed due to some of the odd geometries and curves present in the design. The simulation of the wing shown in Figure 39 is a simplified rotor with squared ends. This version was done to allow the software to complete the mesh model with simpler geometries while having little impact on the original design. In Figure 39, when the chord length was 500 μm , the FEM simulation showed a predicted vertical deflection of nearly 50 μm .

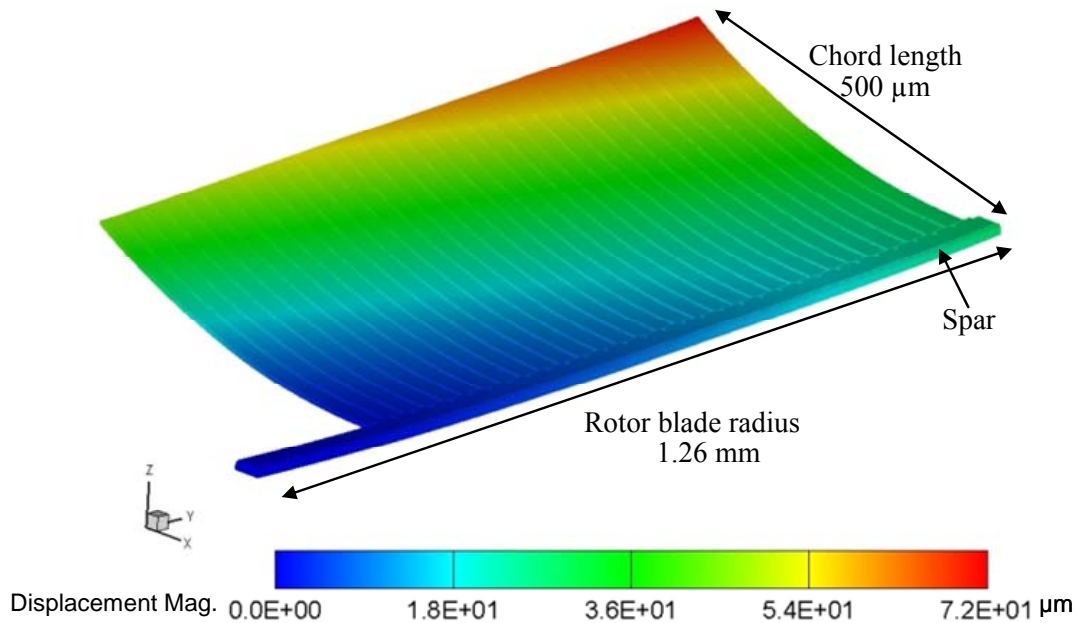


Figure 39: The CoventorWare simulation of a simplified model-A rotor shows a predicted vertical deflection of nearly 50 μm when the chord length was 500 μm long.

Nearly 50 μm of deflection along the 1.26 mm main spar of the rotor blade is perhaps excessive. A similar result is shown in Figure 40 of rotor model-C, where the chord length was 250 μm and the predicted vertical deflection of 6 μm .

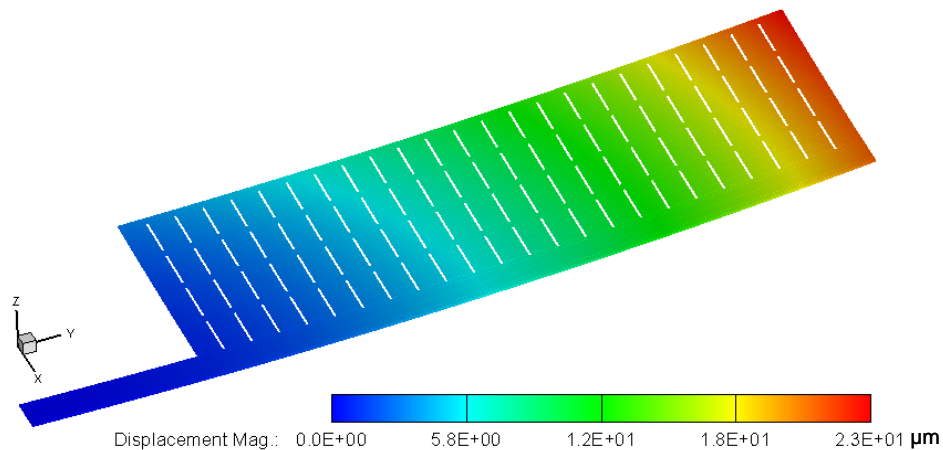


Figure 40: Rotor blade model-C modeled in CoventorWare.

The main spar is comprised of Poly1, trapped Oxide2, Poly2 and gold; making the spar region $4.75\text{ }\mu\text{m}$ thick. The foundry process file in CoventorWare implements a step in which all the oxide layers are removed, leaving only the polysilicon and gold layers. The deflection in the spar is higher than expected because the Oxide2 is not present in the model. To ensure all the rotor blades could be compared equally, two connected segments from each design were simulated at the same time as shown in Figure 41.

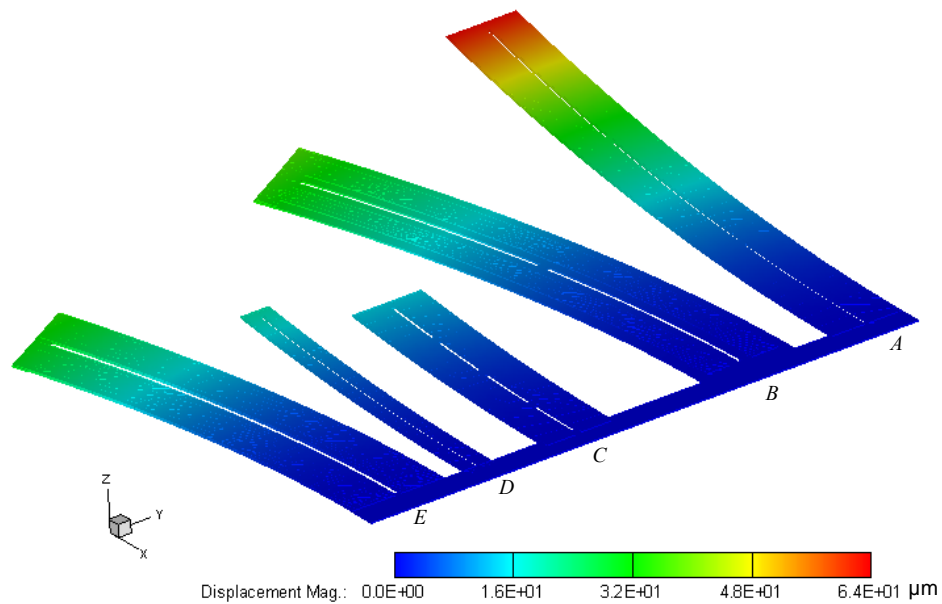


Figure 41: Result of simulating two sections of each rotor design when the residual stress value of gold is set to 25 MPa tensile.

A summary of the predicted deflections achievable from the FEM and numerical analysis of the rotor blades, including the induced angle of attack is provided in Table 4. The deflection values used in the FEM column were taken from the results of the simulation run in Figure 41 where all five designs were completed. Equation (17) from Chapter 3 was used to numerically calculate the deflection for the different rotors.

Calculations for designs that had curves were simplified by using the chord value for the total length.

Table 4: Comparison of the FEM and numerical calculations for rotor blade deflection and angle of attack.

Model	FEM		Numerical		Difference
	Deflection (μm)	Angle (deg)	Deflection (μm)	Angle (deg)	Angle (deg)
<i>A</i>	62.3	7.1	36.04	4.1	2.99
<i>B</i>	36.8	4.3	31.57	3.7	0.61
<i>C</i>	13.81	3.2	9.01	2.1	1.09
<i>D</i>	18.95	3.4	11.62	2.1	1.31
<i>E</i>	32.1	4.7	20.38	3.0	1.71

The residual stress values used from the PolyMUMPs foundry were calculated using Stoney's equations for thin film stress. During the fabrication process, the wafer bow caused by the applied thin film was measured. The calculated stress over the wafer is going to be slightly different than the localized stress values on micron-length cantilever beams. The difference in the macro-scale stress on the wafer to the micro-scale stress on the devices is small but it will affect deflection calculation. The difference in the predicted angle of deflection will be addressed more toward the end of Section 6.6.1.

4.4 Thrust Generation of Rotor Blades

A numerical analysis was done to demonstrate the predicted thrust of the rotor blade designs. Equation (2) from Chapter 3 describes the thrust generated by a rotor as a function of the design parameters and rotational frequency. In the work done by Miki *et al.*, the 2.5 mm radius rotor had the $(C_1 + \phi C_d)$ term equal to 0.74. The rotor designs done in this work are over a millimeter shorter in radius, thus, the $(C_1 + \phi C_d)$ term is

most likely smaller. Various extrapolation techniques were used on the results done by Miki *et. al* and found that the $(C_l + \phi C_d)$ term could potentially be between 0.3 and 0.6. For the thrust calculations can be accomplished, the $(C_l + \phi C_d)$ term was set equal to 0.55, just less than the highest extrapolated value. With that assumption in mind, Figure 42 shows the result of the calculated thrust for each rotor blade design as a function of frequency.

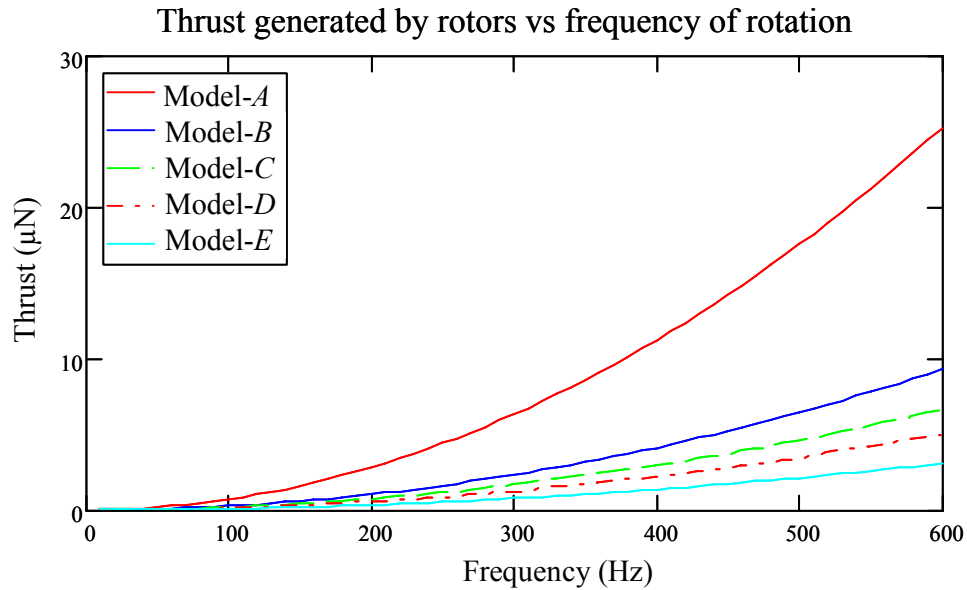


Figure 42: Graph shows the thrust generated by each rotor design when the $(C_l + \phi C_d)$ term was assumed to be 0.55.

Assuming a motor was available to turn the rotors at a 250 Hz rate, the predicted thrust performance per rotor can be concretely compared. Refer back to Figure 31; the vision of the flying robot was composed of 2 rotors. Table 5 summarizes some important lift calculations. The thrust generated by each motor at 250 Hz determined the total mass of the flying device when two rotors are used. Then the mass of the two rotors is

subtracted from the total mass of the flying device, yielding the mass available for the motor, power source, and sensor package. From the previous calculation of mass available, the volume of the support structure can be determined based on the density of the material used.

Table 5: The thrust generated for each rotor design operating at 250 Hz is shown. The other listed parameters are derived from the thrust calculation.

Model	Thrust/rotor (μN)	Mass supportable by 2 rotors (μg)	Mass of 2 rotors (μg)	Mass available for motor, power, & sensor (μg)
<i>A</i>	1.289	262.79	55.82	206.97
<i>B</i>	0.473	96.56	23.43	73.13
<i>C</i>	0.338	69.02	28.65	39.42
<i>D</i>	0.255	52.06	9.866	42.19
<i>E</i>	0.156	31.84	14.26	17.58

The support structure below the rotor blades, identified previously in Figure 31, needs to be at a minimum length to separate the rotor blade tips. For simplicity of the design, it would be easier to keep the rotor tips separated by 100 μm , than try to allow the blades to intermesh as they rotated. Assuming the motor has a 500 μm diameter, the width of the support structure could be 510 μm . The density of silicon is 2.33 g/cm^3 , therefore thickness of the support structure can be calculated and the possible area for the solar cell can be found. The results for these calculations are shown in Table 6

Table 6: Support structure minimum dimensions based on the thrust generated by each.

Model	Length (mm)	Area (mm^2)	Thickness (μm)	Area available for solar cell (mm^2)
<i>A</i>	3.22	1.642	54.10	1.14
<i>B</i>	2.48	1.265	24.82	0.76
<i>C</i>	2.76	1.408	12.02	0.91
<i>D</i>	2.48	1.256	14.32	0.76
<i>E</i>	2.12	1.081	6.98	0.58

Rotor blade model-*A* produced the most thrust, allowing a two rotor system to have a support structure thickness of 54 μm . The support structures for other rotor blade designs were less than half that thickness.

4.5 Chapter Summary

In this chapter, numerical and finite element models were completed for the comb drive and rotor designs. Based on the dimensions of the comb drive, predictions were made as to how much lateral displacement would be achievable over a range of applied voltages. Rotor blade deflection was analyzed, predicting the angle of attack for various chord lengths. Model-*A* from Figure 38 predicted the largest, most consistent deflection along the length of the rotor blade, of 36 to 62 μm .

A numerical model was accomplished to predict the thrust generated by the five different rotor blade designs. After knowing the amount of thrust generated by each rotor, calculations were done to show how large the support structure for each could be. Simulation results showed that the best performing rotor blade was model-*A*, shown in Figure 38. Model-*A* had the largest radius and largest chord length, so it should be able to generate the most thrust.

V. Power Sources

5.1 Chapter Overview

Many possible power scavenging schemes should be considered when looking for a viable source of energy to be used with MEMS robots. Ultimately the power source or sources must be small enough to fit onboard the robot, supply enough energy for untethered locomotion and last long enough to complete the mission. Many possible powering schemes will be discussed and analyzed for implementation possibilities. Some potential sources of power to be considered include: solar cells, radioisotopes, thermoelectrics, and chemical batteries. In this thesis work various power sources are discussed for potential applications only. External power sources were used to test the MEMS motors designed as described in Section 6.2.

5.2 Solar Cells

A large portion of this section will focus on solar power devices since the sun could provide a large source of power. The sun expends over 4×10^{26} W of power during its thermonuclear fusion processes, of which only 844 W/m^2 reach the earth's surface under air mass 1.5 (AM1.5) conditions [32]. As shown in Figure 43, AM1.5 light condition is commonly used when discussing solar cell performance and conversion efficiency. The condition when the sun is directly overhead, passing through "one atmosphere" is AM1. When the sun is 45° off vertical, the light is traveling through more of the atmosphere; this is called AM1.5 condition.

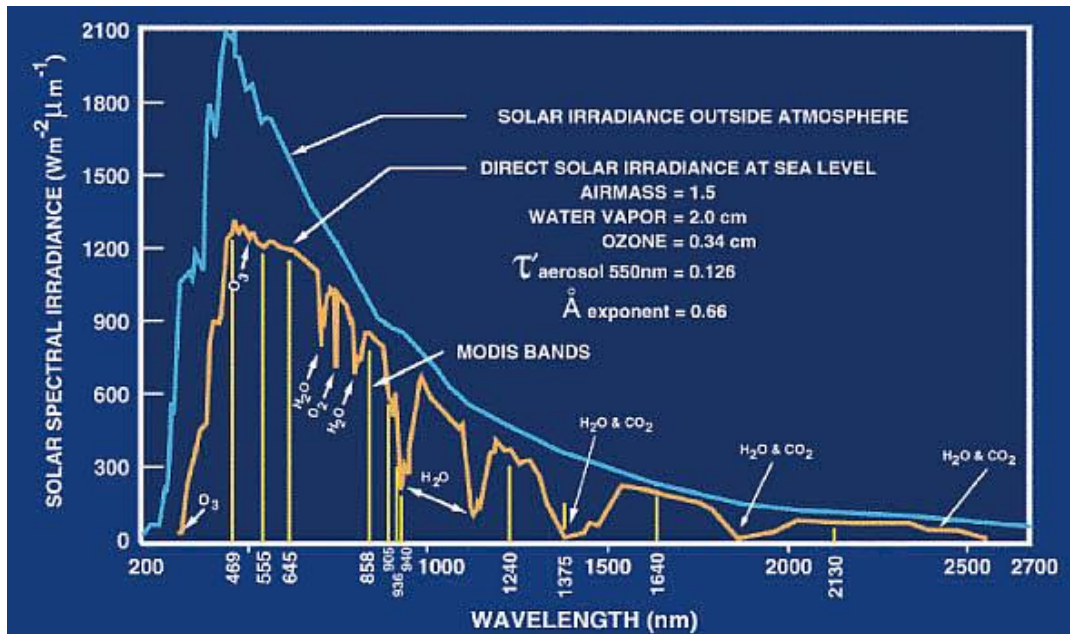


Figure 43: Solar spectral irradiance of sunlight incident on the earth's surface and upper atmosphere [33].

One method of converting the sun's photons into usable electricity is through the use of semiconductor materials creating p-n junction solar cells. Semiconductor solar cells, and in particular tandem solar cells, will be the main focus of this portion because of their higher conversion efficiencies and greater power output. In particular, triple junction solar cells have achieved efficiencies over 36.9 % as seen in Figure 44.

Once a solar cell has generated energy it can be stored in a battery or used by a system that requires DC current. Satellites for example, use batteries to store power for times when they are in the shadow of the earth. Integration of solar cells and thin-film batteries would be an ideal way to power a MEMS robot. Both the solar cell and thin-film batteries could theoretically be fabricated in a layer less than 30 μm thick. Building a thin-film energy harvesting and storage system is the focus of four major universities at this time. The University of Washington, University of Colorado, University of

California–Los Angeles, and Virginia Polytechnic Institute are funded by the Air Force Office of Scientific Research (AFOSR) to conduct research on energy harvesting and integration to aero vehicles over the next five years.

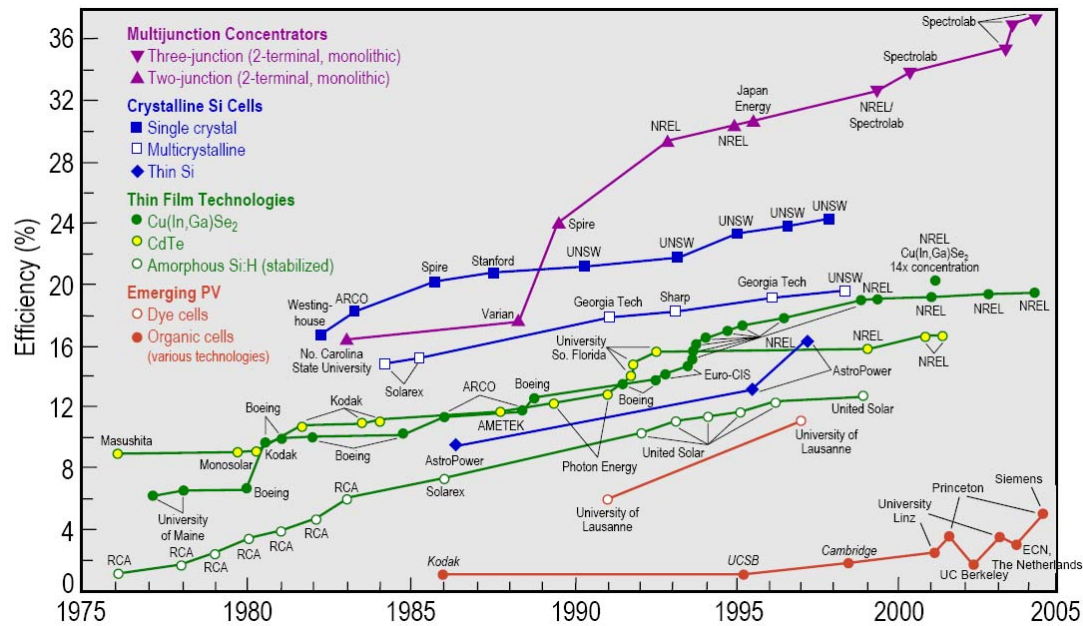


Figure 44: Solar cell efficiencies have greatly increased over the last quarter century [34].

Figure 45 shows a depiction of a thin-film energy harvesting scheme which could be used on the surface of a UAV wing, which could produce and store power. The University of Washington has chosen polymer solar cells over multi-junction semiconductor solar cells because polymers are much more flexible. Multi-junction solar cells are very efficient but they are also very brittle and would crack under the stresses experienced on the skin of an airplane wing.

The premise behind the operation of solar cells is the generation of electron-hole pairs in a semiconductor material which causes a net flow of carriers through the cell via

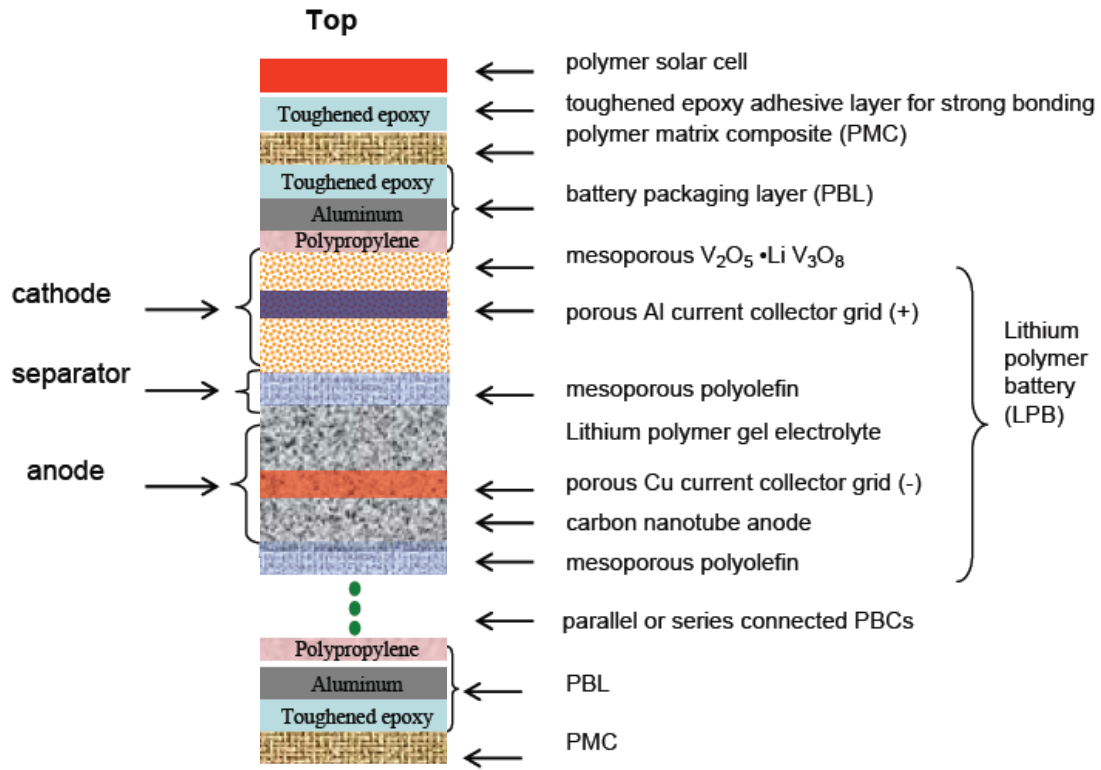


Figure 45: Proposed energy harvesting and storage system which will be made of polymer solar cells and lithium polymer batteries [35].

diffusion across the p-n junction. Photons have different energies depending on the specific wavelength of light. The equation for the energy of a photon of light is given by

$$E = h\nu \quad (19)$$

where E is the energy in eV, ν is the frequency in s^{-1} and h is Planck's constant, 4.135×10^{-15} eV·s. If the photon has energy greater than or equal to the bandgap, an electron in the valence band could absorb the photon, exciting the electron into the conduction band. A photon with energy less than the bandgap will not be absorbed and will pass through the semiconductor. If a photon is absorbed with energy greater than the bandgap, the extra energy is dissipated as a phonon in the crystal lattice as the electron

relaxes to a lower energy level in the conduction band. Figure 46 is an energy band diagram of a simple open circuit p-n junction under solar illumination.

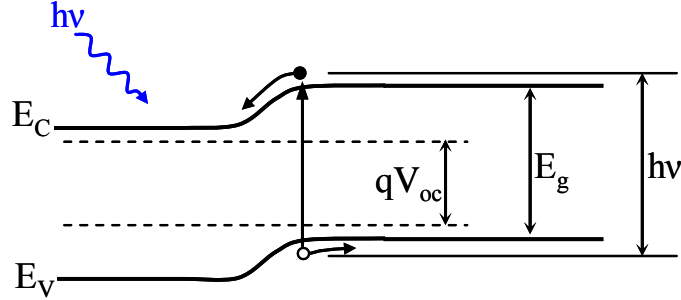


Figure 46: Energy band diagram of a simple p-n junction under solar illumination showing the generation of an electron hole pair when the photon was absorbed [36].

The p-n junction shown in Figure 46 is under a forward bias condition induced by the generated carrier separation, which creates an open circuit voltage of V_{oc} across the device. The amount of band bending experienced in Figure 46 is caused by the open circuit voltage qV_{oc} , in electron volts. When a photon is absorbed by an electron and is excited to the conduction band, an electron-hole pair is generated. The electron in the conduction band is then a minority carrier in the p-type material.

The electron has a specific lifetime which is governed by the amount of dopant and the temperature of the semiconductor. The minority carrier diffusion length L_n is given by

$$L_n = \sqrt{\mu_n \frac{kT}{q} \tau_{no}} \quad (20)$$

where μ_n is the electron mobility, k is the Boltzmann constant, T is the temperature in Kelvin, q is charge, and τ_{no} is the minority carrier lifetime. Only electron hole pairs that are generated from the incident radiation within the depletion region will participate in

current production for the solar cell as seen in Figure 47. Electron hole pairs generated within a diffusion length of the depletion region could potentially contribute to power production but their contribution is minimal.

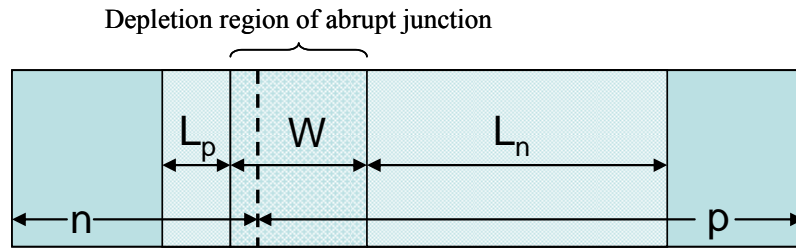


Figure 47: The depletion region has a specific width, W which is the active region for current productive photon absorption.

Electron-hole pairs which are generated outside those previously mentioned two zones will recombine and not play a role in current generation. Typically the p-type region is 5-40 times thicker in monolithically growth tandem solar cells because it is the most desirable region for the photons to be absorbed. The p-type region is not doped as heavily as the n-type region allowing the minority carrier electrons to have a longer lifetime and a higher mobility. The majority of the volume of the depletion region is on the p-type side due to the lower dopant concentration, so it has the larger volume for photon absorption.

Figure 48 is a diagram of a simple circuit with a solar cell connected to a load resistance. The incident photons generate the electron-hole pairs in the depletion region and within a diffusion length of the p-n junction. The electron diffuses from the p-material across the junction to the n-type material where it sees a lower potential in the n-type material conduction band. This process causes a current I_L to flow through the

circuit across the load resistance R_L . The voltage drop across the load resistor is V_L , since $V=I \cdot R$. Kirchhoff's voltage law states, "the sum of the voltage drops around a circuit will be equal to the voltage drop for the entire circuit" [37]. Kirchhoff's law shows that the voltage drop across the load resistor must be equal to the voltage drop across the solar cell. The voltage drop across the load resistor forward biases the solar cell, which causes the bands to bend by the amount qV_L .

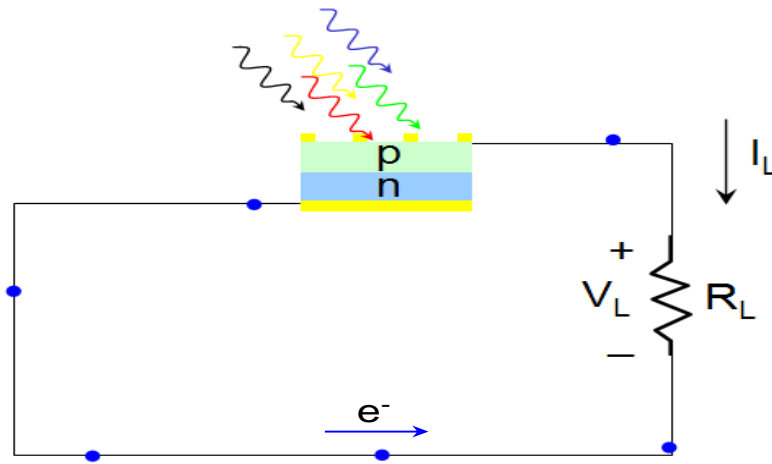


Figure 48: Example solar connected to a load resistance. Note the current flow is in the direction of reverse saturation current.

Important plots to examine when evaluating solar cell performance are the I-V curves they produce. Figure 49 shows an I-V curve of a sample solar cell where the maximum current I_m and maximum voltage V_m are labeled, which is the point where the maximum power can be generated.

The current voltage relationship in solar cells comes from the equation

$$I = -J_s A (e^{\frac{qV}{kT}} - 1) + J_L A \quad (A) \quad (21)$$

where I is the current through the solar cell, V is the voltage across the solar cell, J_s is the reverse saturation current density, J_L is the current density of the load, and A is the

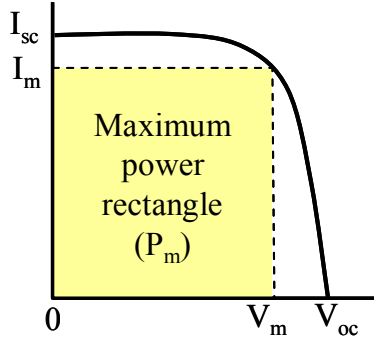


Figure 49: I-V curve for a solar cell showing the maximum power square [36].

surface area of the solar cell. The power curve P is found by multiplying I by V . The value V_m is found by taking the first derivative of P with respect to V , where

$$\frac{d}{dV}P = \frac{d}{dV} \left[\left(-J_s A (e^{\frac{qV}{kT}} - 1) + J_L A \right) V \right] = 0. \quad (22)$$

Solving Equation (22) for V , and then substituting into Equation (21) determines I , determining the maximum power for the solar cell.

The open circuit voltage V_{oc} is important because it gives the maximum voltage the solar cell can attain, at which point there will be no net current flow through the solar cell. The maximum voltage used for power generation will always be less than V_{oc} . The open circuit voltage is defined by

$$V_{oc} = \frac{kT}{q} \ln \left(\frac{J_s}{J_L} + 1 \right) \quad (V). \quad (23)$$

Now that all the basic parameters for solar cells have been defined, some of their figures of merit can be discussed. The power conversion efficiency η of a solar cell is defined as

$$\eta = \frac{I_m V_m}{P_{in}} \quad (24)$$

where P_{in} is the total power incident on the solar cell, which is approximately 844 W/m^2 under AM1.5 conditions [32]. Another important indicator of cell performance is the fill factor, FF where

$$FF = \frac{I_m V_m}{V_{oc} I_{SC}}. \quad (25)$$

The fill factor is a ratio comparing the maximum power P_m over the power that would be created if V_{oc} and I_{SC} were multiplied together.

The same basic principles of operation that were previously discussed for single junction solar cells still apply to multi-junction solar cells. Tandem solar cells just have a few extra layers that are needed to enhance performance. A sample triple junction solar cell is shown in Figure 50 which achieved efficiencies of 32% under AM1.5 at one sun concentration and 35.2% under 66 sun concentration via lens focusing [38].

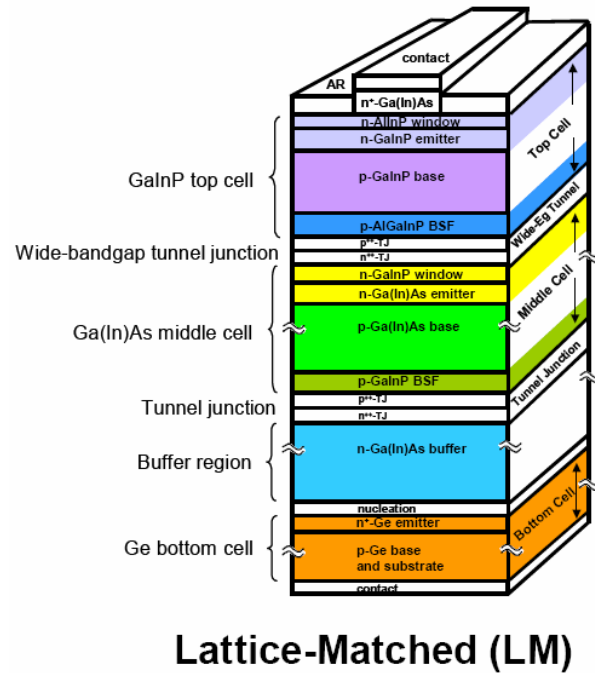


Figure 50: Triple junction lattice-matched solar cell with labeled layers, produced by NREL [38].

The tunnel junction in tandem solar cells is of utmost importance because it allows carrier flow between the top and bottom cells. Multi-junction solar cells would not function at all without tunnel junctions. Both layers of the tunnel junction are typically on the order of 10 nm thick and are always degenerately doped. These very thin highly doped layers have an extreme amount of band bending as shown in Figure 51.

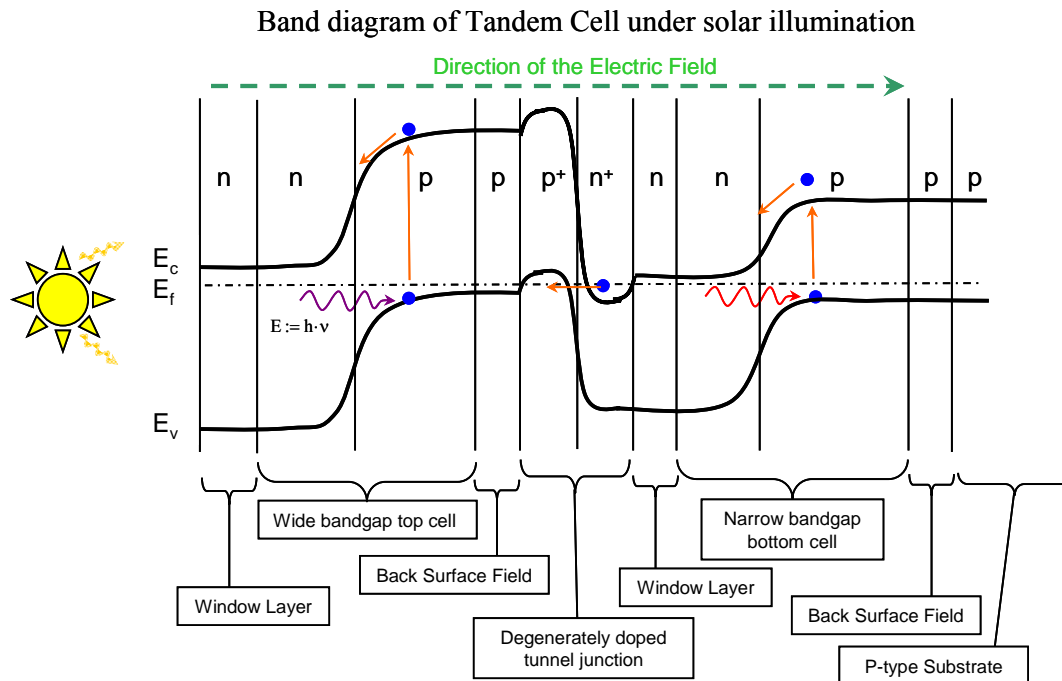


Figure 51: Band diagram of a typical two junction tandem solar cell structure.

This bending in the band diagram brings the conduction band in the n⁺-type material very close to the valence band of the p⁺-type material which allows carriers to easily tunnel through to the other side. Electrons will tunnel from the n⁺ to p⁺, and holes will move from p⁺ to n⁺ regions. Researchers are also developing hetero-tunnel junctions which would require less dopant to get a similar amount of band bending. The layers

above and below the tunnel junction also act as diffusion controllers, inhibiting ion diffusion during the fabrication process.

Table 7 discusses some of the factors that reduce solar cell efficiency. The previous equations discussed up to this point have been the ideal functions. Degradations of cell efficiency are mostly due to surface recombination, Shockley-Read-Hall recombination, and some series resistance.

Table 7: List of factors that reduce solar cell efficiency.

Problem	Cause	Effect
Surface recombination	Dangling bonds at a surface	Reduces electron-hole pairs available for current production, lowers power output.
Shockley-Read-Hall recombination	Impurities or lattice defects	Reduces electron-hole pairs available for current production, lowers power output.
Series Resistance	Metal contact resistance, Bulk semiconductor resistance from low dopant	Reduces the open circuit voltage, thereby reducing efficiency and power output.

5.3 Radioisotopes as a Power Source

Radioactive materials are used in many applications such as large scale power generation, medical treatments, industrial processing, and in miniature batteries. There are three main types of particles that can be emitted from radioactive material: alpha (α), beta (β), and gamma (γ). Each type of particle has different characteristics.

Alpha particles are made up of protons and neutrons, very similar to the nucleus of a helium atom. Alpha particles have a positive net charge and are relatively massive, approximately 7,344 times heavier than an electron. The penetrating power of an α

particle is very low; a sheet of paper can stop them. The hazards posed when using α particle emitting materials is that they are harmful if ingested. Alpha emitters are the “safest” radioactive material to handle.

Beta particles are electrons which are emitted from a radioactive material and have moderate penetrating power. The amount of energy the β particle has depends on the velocity at which it was emitted. Typically β particles can be stopped by a sheet of metal 20-500 μm thick, depending on the velocity. These particles are very hazardous because they will cause burns on the skin and are harmful if ingested. Beta emitters are more difficult to handle; they require more stringent controls for shielding due to their increased health risks.

Gamma particles are photons of electromagnetic radiation emitted from certain radioactive materials. Gamma rays have a very high energy, a high frequency and a very short wavelength. They are the most dangerous because it takes several cm of lead to stop the photon. Shielding used for gamma emitters is usually a combination of lead, steel, and concrete. Concrete is the least effective at stopping the gamma radiation, but it is cheap to use when a large volume of containment is needed. Due to the health risks, gamma emitting sources are a poor choice as a power source for a flying microrobot.

A popular area of research in recent years has been in studying betavoltaics. Betavoltaics use radioactive isotopes that emit β particles which interact with a semiconductor p-n junction generating power much like solar cells. The surface area for β particle interaction with the p-n junctions has been increased by fabricating micro cavities, which has improved the betavoltaic power density. Alpha emitters are not

commonly used in this configuration because the large α particles can displace atoms in the crystal lattice creating defects. Defects in the semiconductor crystal would greatly reduce the efficiency of the p-n junction over time.

In the work done by W. Sun *et. al.*, tritium gas was used as the isotope for power generation. Tritium is an isotope of hydrogen with a half-life of 12.3 years [39]. Gaseous tritium has a low toxicity and is the most benign radioisotope known [39]. The shielding required for the tritium showed that the beta particles had a maximum diffusion length of 4.3 μm , so in theory the radiation should be contained in the packaging if the surrounding silicon is thicker than the maximum diffusion length. The I-V curves for their fabricated devices which showed a maximum power of 30 nW/cm². In comparison to the best triple junction solar cells, the tritium battery produced 1×10^6 less power per square centimeter. The power produced by betavoltaics could be much higher, but the toxicity of the isotopes used would also greatly increase.

5.4 Thermoelectrics

Thermoelectric power generation takes advantage of the Seebeck effect which is the conversion of temperature differences directly into electricity. A diagram of a thermoelectric generator is seen in Figure 52. The p-type and n-type legs generate a current flow when there is a temperature gradient. The electrical current produced is proportional to the temperature gradient between the hot and cold junctions. This technology has been used on deep space probes like Cassini-Huygens [40]. The heat produced for the hot junction is generated by a radioactive material inside the spacecraft and the cold junction is exposed to the exterior of the spacecraft. Smaller thermoelectric

devices, $1.15 \times 1.15 \times 0.2 \text{ in}^3$, have been made that can produce 2.5 W of power at 3.3 V when there is a 200 °C temperature gradient [41]. Most thermoelectric devices have efficiencies around 5 %.

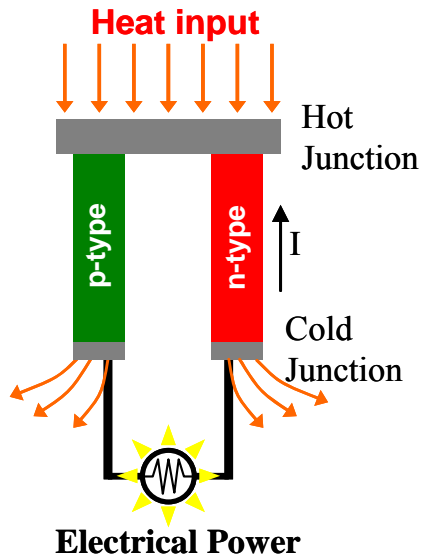


Figure 52: Diagram of a thermoelectric device generating power from the temperature gradient [42].

Polonium 210 is a radioactive metalloid which emits α particles and could be used in a thermoelectric device. This metalloid has a half life of 138.4 days and releases 140 W/g during its radioactive decay. Just a half a gram of contained ^{210}Po will reach temperatures over 500 °C, creating a 200 °C temperature gradient [43]. Using 1 mg of ^{210}Po in a thermoelectric converter setup with 5 % conversion efficiency would produce 56 mW of power. The high temperatures associated with the use of ^{210}Po may cause structural changes in a millimeter-scale MAV, but it could be used in larger MAV designs.

5.5 Chemical Batteries

Chemical batteries are another means of supplying power to a MAV. Batteries store chemical energy, when the battery completes a circuit, the reaction makes the energy available in an electrical form. The positive and negative terminals do not come into contact; rather a solid or liquid electrolyte is used between them. The electrolyte contains ions which react with the electrodes. Batteries can be divided into two categories, rechargeable and non-rechargeable. The chemical reaction is reversible in rechargeable batteries by applying current from an external source. Non-rechargeable or disposable batteries are one time use; once the chemicals needed for the reaction are depleted, the cell is rendered useless. Disposable batteries are a poor choice for an operational micro air vehicle application. The short life span and large number of replacement batteries required to operate the MAV would be a hindrance. Some form of a rechargeable battery is more desirable.

Batteries being designed and fabricated at the University of Washington-Seattle are making great advances in battery power density. Figure 53 is a graph of the specific power and specific energy of four different power source types. The performance results of the nanorods, nanotubes, and core-shell nanocables used as electrodes in lithium (Li) batteries and are shown in Figure 53 are represented by the X's. These batteries are better because they display larger storage capacity and fast transport kinetics [44].

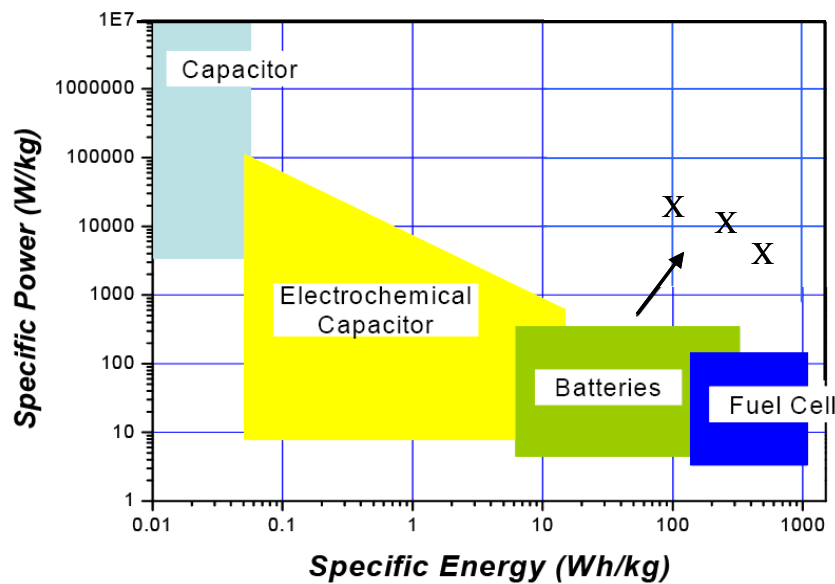


Figure 53: Graph of power density and specific energy for different types of power sources, specifically performance of the nanostructured electrode Li batteries highlighted by the X's on the graph [44].

5.6 Chapter Summary

Tandem solar cells have higher efficiencies because they absorb photons more effectively. The wider bandgap top cell makes better use of the higher energy photons while the lower energy photons are allowed to pass through to the lower cell. Less energy is converted to phonons and more energy is used for voltage production. The key parameters that an engineer has control over are material choice, dopant concentrations and the layer thickness; by optimizing those three choices the solar cell efficiency can be maximized.

Trends for future research are heading toward four, five, and even six layer multi-junction solar cells. Figure 54 shows a future prediction of where solar cell efficiency and technology are headed. With increased efficiency, there will be more power generated per unit area.

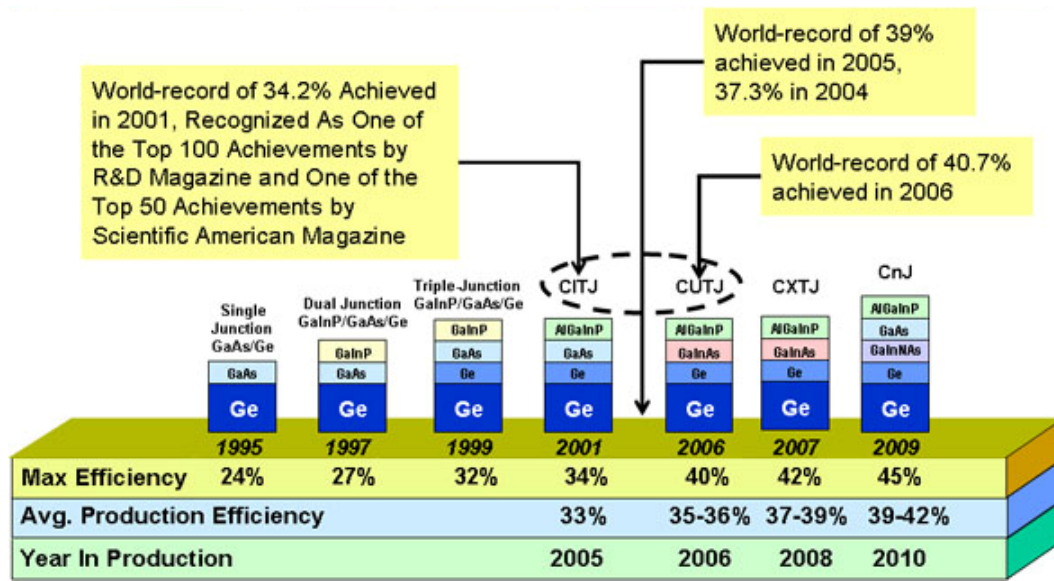


Figure 54: Trend in research is heading toward six junction solar cells with higher efficiencies [45].

A major drawback for the use of radioisotopes in MEMS devices is having hundreds of insect sized robots flying around with radioactive particles of material in them. There could be dire consequences if the radioactive robots were ingested by humans or animals.

Chemical batteries would only be a realistic possible power source for a MAV if they were rechargeable and have the means available to be recharged on board. A triple junction solar cell used in conjunction with a thin film rechargeable battery seems to be the safest power source for a MAV. Millimeter-scale solar cells have demonstrated the capability to generate over 100 V, but thin film batteries unfortunately have not on the millimeter-scale.

VI. Experimental Setup and Results

6.1 Chapter Overview

This chapter will discuss many of the successes and lessons learned which were encountered during the course of this thesis effort. Three types of motors and five different rotor designs were successfully fabricated and tested using the PolyMUMPs process. First, the setup used to power the motors will be examined followed by the results for each motor design. Second, the wing deflection from each design will be studied and compared to determine the greatest potential for generating lift.

6.2 Signal Generation

Signal generation can be broken down by the three categories of motors tested: scratch drives, three phase motors, and comb drive resonators. The signal requirements for each motor will be discussed in the aforementioned order.

The scratch drive was able to turn at the lowest applied voltage of the three types of motors tested and also, unfortunately, the slowest. The output of a function generator was connected to the input of a Krohn-Hite high voltage amplifier. The AC input signal to the amplifier was amplified and a DC bias could be applied to achieve a maximum peak voltage of 200 V. For the scratch drives, a square waveform was used.

The three phase electrostatic motors that were tested required a relatively high voltage power source, requiring a range from 150 V to 300 V. Three square wave signals were required to operate the motors, and a 120° phase shift between each of the three signals was necessary. LabVIEW was used to produce the required phase shifts in the signals and an external circuit was used to provide the high voltages required. The

illustration in Figure 55 shows a simple diagram of the experimental setup used to generate the three phase signals. The LabVIEW software was used to control the National Instruments USB-6259 Digital Acquisition (DAQ) card, which had a total of four analog outputs available, of which only three were used here.

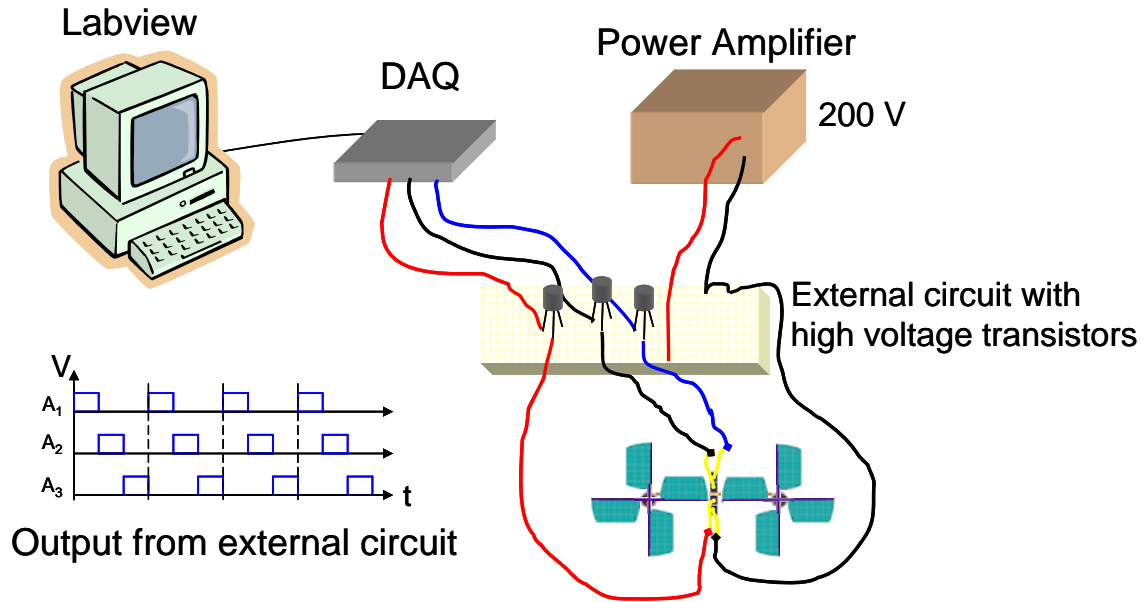


Figure 55: Experimental setup for generating the signals required to run the three phase electrostatic motors.

Each analog output from the DAQ was connected to V_{in} on an individual external circuit, like the one shown in Figure 56. PMOS transistors were used in the circuit so the gate to source threshold voltage ($V_{GS\ th}$) had a range of -2 V to -4 V, so V_{in} was typically set to be a ± 2.5 V peak-to-peak square wave. The LabVIEW code used to generate the signals can be seen in Figure 89 and Figure 90 of Appendix C along with one of the external circuits used is shown in Figure 91.

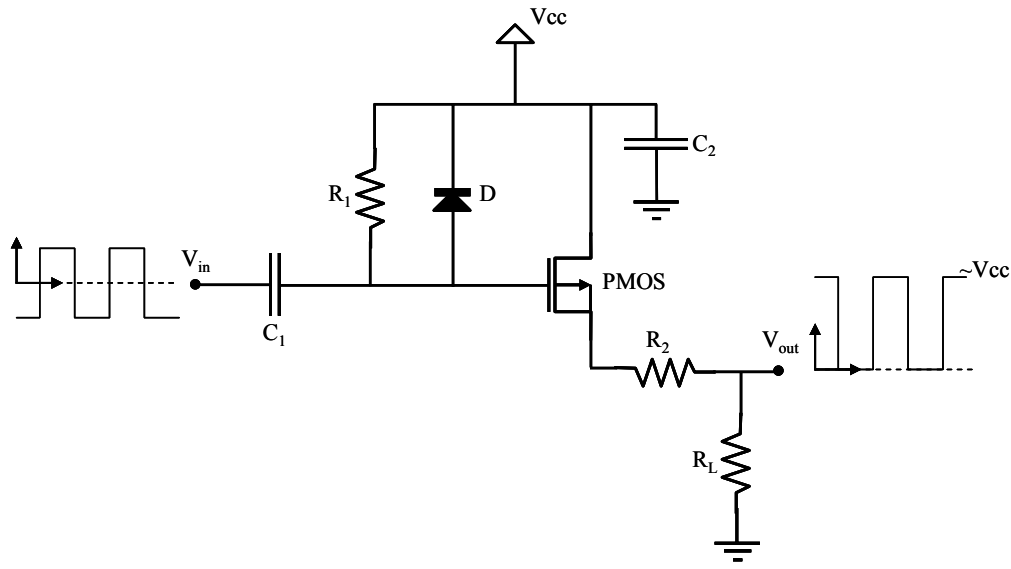


Figure 56: External circuit that is used to produce square waves with high peak voltages nearly equal to V_{cc} .

Finally, independent comb drive resonators could be driven by either a function generator connected to a Krohn-Hite amplifier or by LabVIEW and an external circuit. When two comb drive resonators are connected orthogonally to turn a gear, LabVIEW and two external circuits should be used, with a 90° phase shift between the two signals. When the external circuit is used to create the voltage signal, it can only generate a square waveform. When the function generator and Krohn-Hite amplifier are used, the resonators can be driven by square, sine, or saw tooth waveforms, up to 200 V.

Figure 57 shows the experimental setup in the lab with the LabVIEW program controlling the DAQ, signaling the external circuit. The outputs from the external circuit are then connected to the micro-manipulators on the probe station.

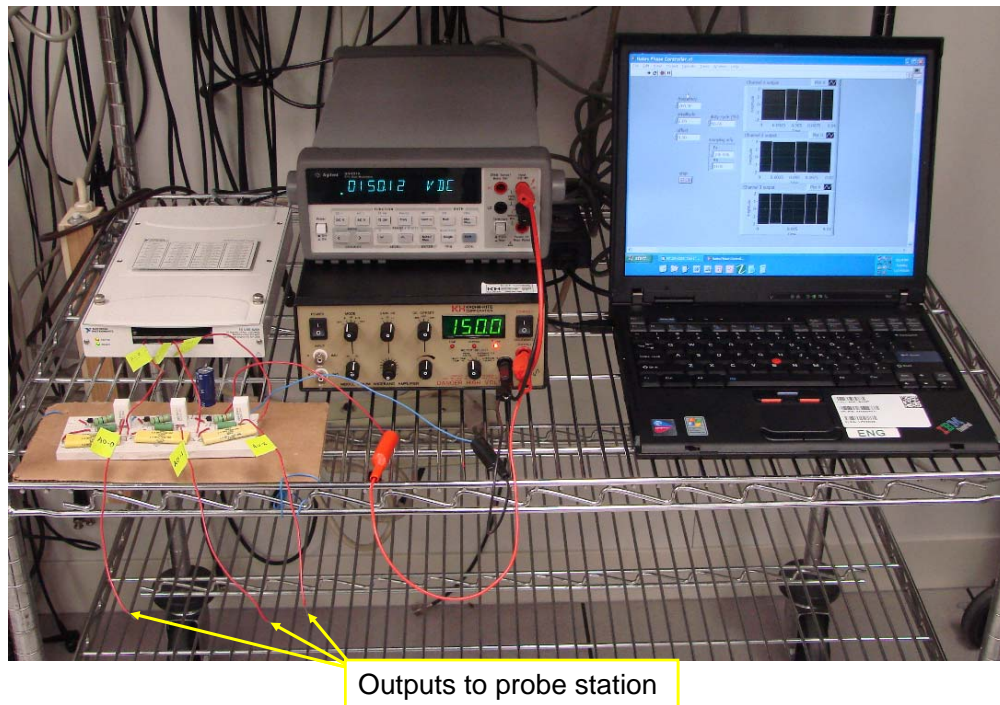


Figure 57: Experimental setup showing the LabVIEW software controlling the DAQ card which is signaling the external circuit which will drive the electrostatic motors.

6.3 Circular Scratch Drives

Many different sized circular scratch drives were fabricated in PolyMUMPs run 71 and are shown in Figure 76 of Appendix A. The variations included different plate lengths, drive diameter, and the number of plates per drive. In theory, the more plates there are in the circular scratch drive, the more torque the scratch drive actuator (SDA) will be able to produce. The SDA in Figure 58 used the pictured plate design to maximize the number of plates and attempt to reduce the drive voltage with the longer plate length. Longer plate designs require lower AC signal bias voltages for operation [46].

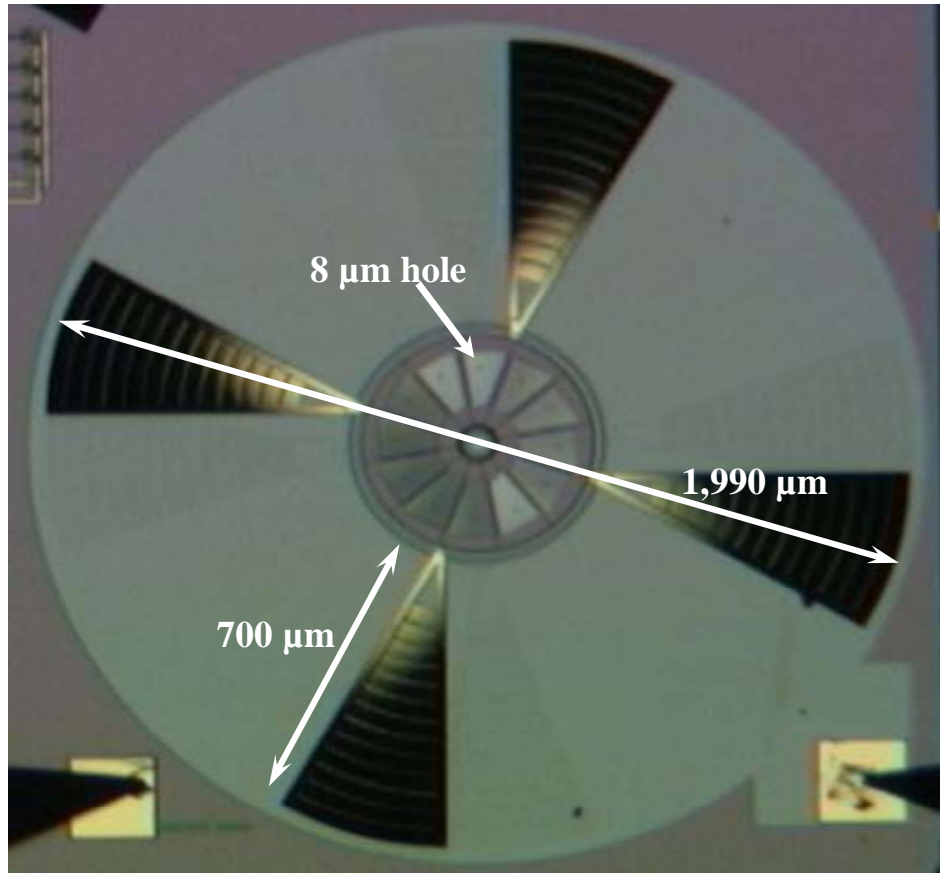


Figure 58: This scratch drive with attached 700 μm long rotor blades was fabricated in PolyMUMPS[®] run 74 and rotated at a rate of less than 3 RPM when the 9 kHz drive frequency was applied.

The SDA pictured in Figure 58 operated at drive frequencies ranging from 100 Hz to 9 kHz. At the maximum achieved drive frequency of 9 kHz and 85 V, the resulting rotational rate of the rotors was less than 3 RPM. Numerous attempts were made to drive the device at higher frequencies over a range of voltages, but rotation did not occur. To achieve a rotational rate of 250 Hz, this device would need to turn almost 800 times faster.

There are several design features that differentiated this work from that done by Linderman *et. al.* on the micro rotary fan. The SDA plate length on this design was

105 μm long where as Linderman *et. al.* used an 80 μm long plate. The longer plate length was used in an attempt reduce the required drive voltage. Unfortunately the longer plate length and larger radius of the SDA also reduced the achievable rotational frequency. Secondly, the rotor blade deflection process was simplified by using Poly2/gold residual stress rotor blades. The amount of deflection achieved was much less, but the mass of the system was reduced by not using solder spheres. On several of the SDA motors tested with the attached rotor blades, stringers of gold could be seen dragging from the underside of the blades. In an attempt to maximize deflection in the Poly2/gold blades, the gold was only 1 μm away from the edge of Poly2 which caused the gold stringers to form. The additional friction of the gold stringers and the underside of Poly2 touching the Poly0 surface must be a hindrance to the achievable rotational speed.

Since each actuation of the SDA plate only produces minute forward motion, on the order of nanometers per cycle, the radius of the SDA motor is important. The radial distance from the center of the motor to the middle of the bushing in the plate should be minimized to produce faster rotation. While the torque τ produced by the motor is shown by

$$\tau = F \cdot r \quad (26)$$

where F is the force generated by the plates and r is the distance from the center of the motor to the middle of the bushing in the plate. The larger radius motors can produce more torque assuming the plate designs remained the same.

This design could be optimized, but the needed frequency of rotation would not be achievable. The low frequency of rotation for this particular SDA motor design seems to preclude it from being a viable choice for a motor in a flying microrobot.

6.4 Three Phase Electrostatic Motors

The three phase electrostatic motor performance up to this point has been inadequate. Thirty six variations of motors were designed in PolyMUMPs runs 71 through 75. The DAQ card, which was controlled by the LabVIEW software program, did not arrive until 15 September 06 so the first motor designs were not tested until a few days later. Having not tested any motors until mid September 06, the basic design of the motors had remained virtually the same for PolyMUMPs runs 71 through 74.

Figure 59 (A) shows one of the electrostatic motors from PolyMUMPs[®] 71 before power was applied. Figure 59 (B) shows the same motor after the three phase 150 V signals were applied. The inner rotor did not move and the device has shorted out, the melted wiring can be seen just left of the probe contact pads. After this motor failed to operate as desired, it was placed in the scanning electron microscope (SEM).

The SEM image shown in Figure 60 illustrates some of the shortcomings in the design and fabrication problems. The mask alignment of the Poly2 layer was off by approximately 1.5 μm , causing the Poly2 stringers to form. When the high voltages were applied, the Poly2 stringers and other loose fragments of polysilicon shorted between the exterior stators and the Poly0 ground plate. The ripples in the polysilicon center rotor are from the high current that passed through the center of the device when it shorted out.

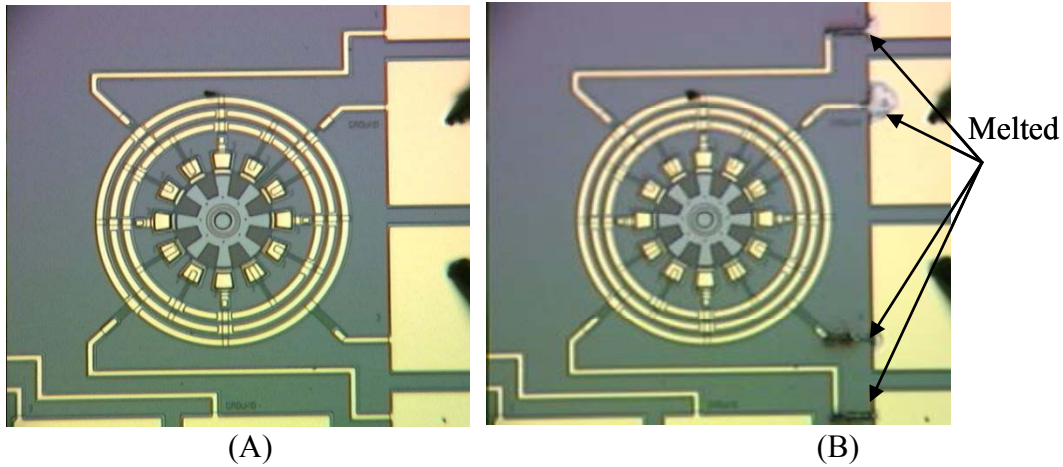


Figure 59: Image (A) is an electrostatic motor from PolyMUMPs® run 71 before power was applied. Image (B) is the same motor after the three phase 150 V signal was applied. The only visible sign of shorting out that can be seen under the optical microscope is where the wires connect to the probe pads.

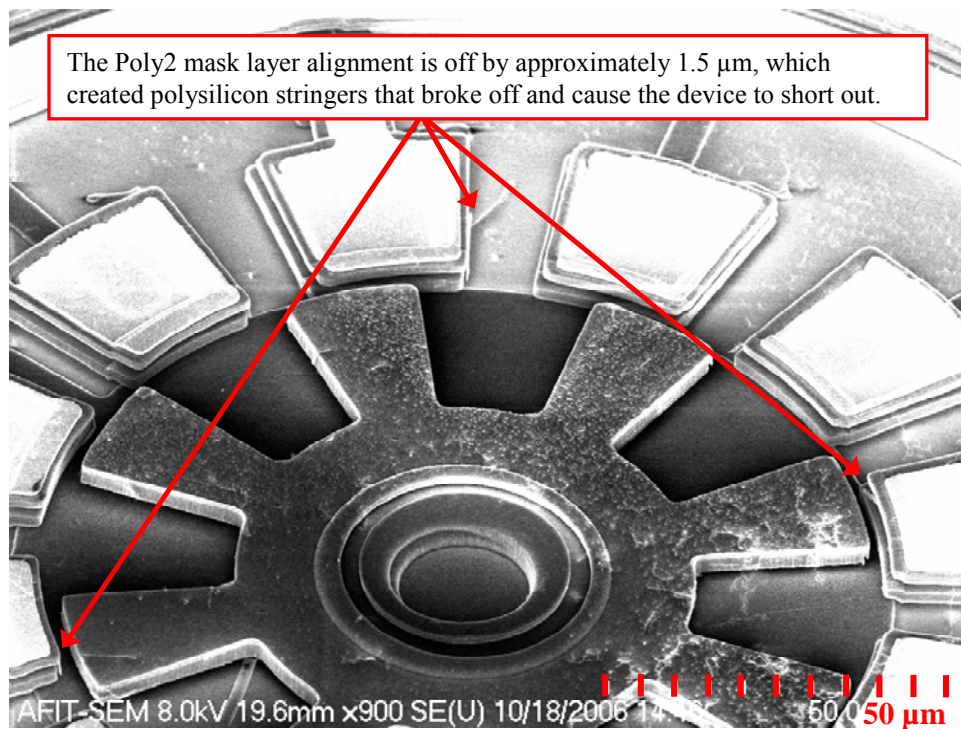


Figure 60: SEM image of an electrostatic motor design from PolyMUMPs run 71 after being tested with 150 V signals and then shorted out due to the polysilicon stringers.

One of the motors tested from PolyMUMPs run 71 did turn one sixteenth of a rotation before shorting out. That slight rotation was the extent of the success achieved with the electrostatic motors from run 71 through run 74. Improvements to the designs submitted for PolyMUMPs run 75 created vertical side walls and no polysilicon stringers.

Figure 61 illustrates the SEM image of the fabricated motor on the left and the original L-Edit drawing on the right. In an effort to maximize the capacitive interaction of the inner rotor and exterior electrode, a smooth stacked Poly1/Poly2 layer structure is desired. The L-Edit image on the right in Figure 61 shows the Poly1/Poly2 stacked layers are connected by a Via etch of the exact same dimensions. The resulting fabricated structure on the left in Figure 61 shows many polysilicon stringers on the rotor which would cause the device to short out.

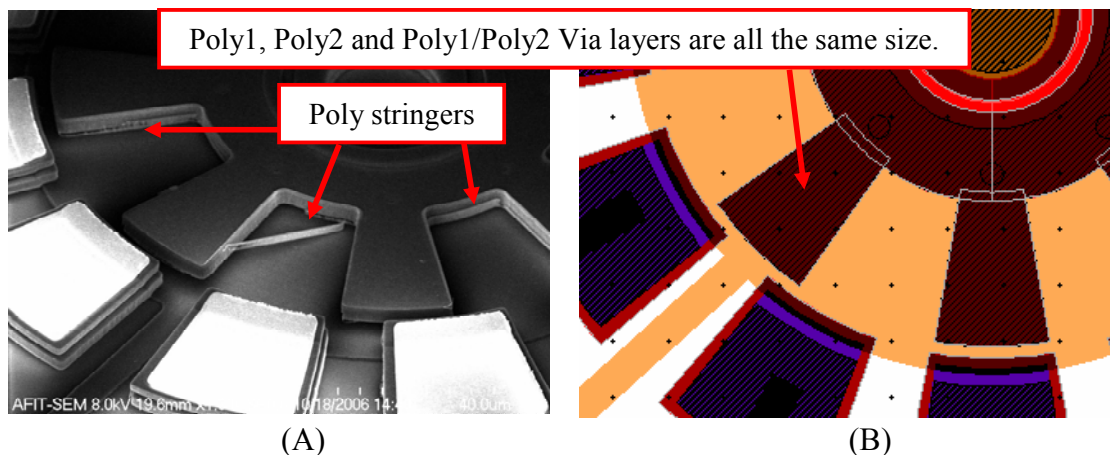


Figure 61: The SEM image shown in (A) has Poly stringers created from having the stacked Poly1, Poly2 layers and the Poly1/Poly2 Via all the same size which is shown in the L-Edit drawing in (B).

The previously mentioned problems with the polysilicon stringers have been corrected in the designs for PolyMUMPs run 75. Figure 62 shows the improved L-Edit design and an SEM image of the electrostatic motor with stacked Poly1/Poly2 layers.

The Poly1 material that is exposed by the Via etch and is not covered by Poly2 will be etched away by the Poly2 etch. This procedure creates nearly vertical edge stacked Poly1/Poly2 structures, which is a vast improvement over previous designs.

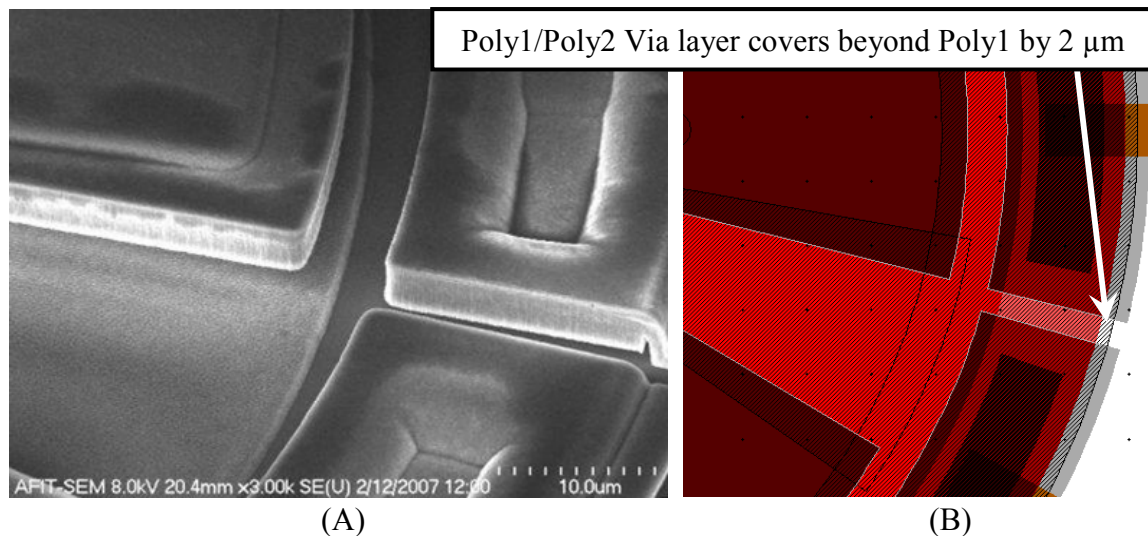


Figure 62: The SEM image of an electrostatic motor shown in (A) from a design in PolyMUMPS run 75 was taken at a 45° angle and does not have any Poly stringers. L-Edit drawing (B) shows that the Poly1/Poly2 Via extends beyond the Poly1 region by 2 µm. Poly1 material that is exposed by the Via and is not covered by Poly2, will be removed by the Poly2 etch, ensuring vertical sidewalls on the stacked poly layers.

Only three electrostatic motors were tested by the end of December when PolyMUMPS® run 75 chips were received back from the foundry. A problem with the external circuit board shorted out the DAQ card, which had to be sent away for repairs. The replacement DAQ card was not received back from the manufacturer until 23 January which greatly limited the time available for further tests.

Had the electrostatic motors worked properly, Figure 63 illustrates one way to physically connect the rotor blades to the motor. To mount the rotor on top of the motor, two spacer rings are required to ensure the rotor spar has sufficient clearance over the

exterior stators. Two fitting collars were made to interlock together and center the rotor over the motor. Another method devised could use a mask to pattern SU-8 photoresist on top of the center rotor. Both methods require epoxy to bond the rotor in place on the photoresist or circular collars. The mask designed for connecting the rotor is shown in Appendix B, Figure 88.

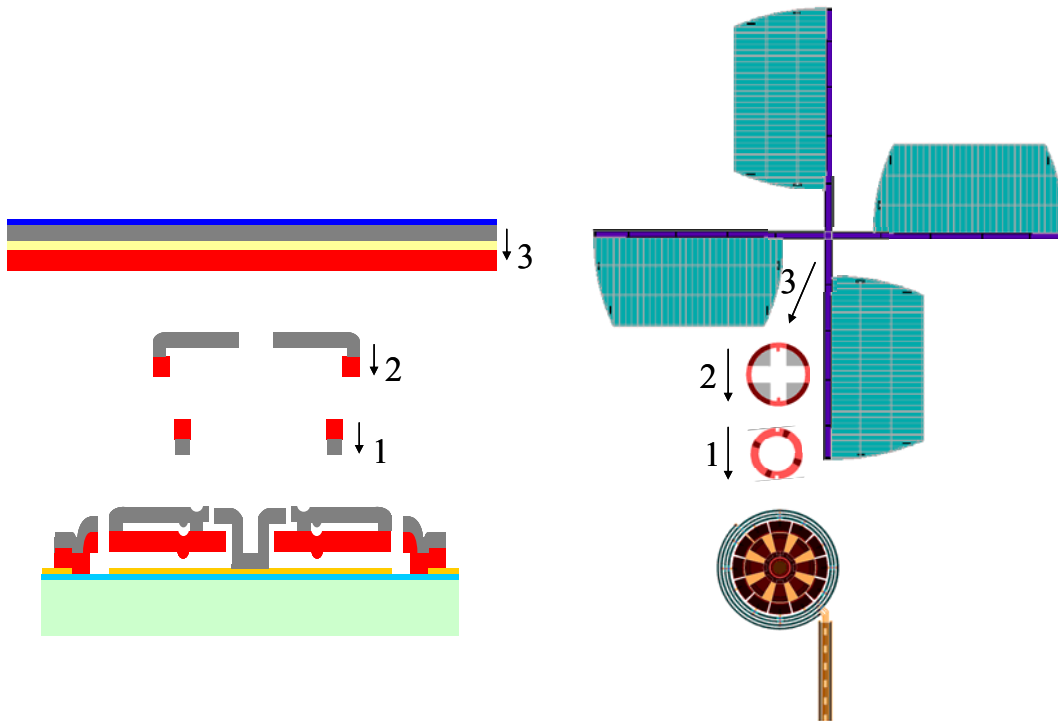


Figure 63: Plausible method for mounting the rotor blade to the electrostatic motor is illustrated above. The cross-sectional view, shown on the left, illustrates stacking the mounting collars onto the electrostatic motor and the top view is shown on the right.

6.5 Comb Drives

Comb drive (CD) designs were only fabricated on PolyMUMPs run 75, the last scheduled fabrication available. All of the comb drive designs worked as desired as stand alone devices. The finger thickness of $3.5\ \mu\text{m}$ and the gap between fingers of $3\ \mu\text{m}$ is

limited by the PolyMUMPs fabrication process. The width of the fingers and gap between them is illustrated in the SEM image in Figure 64. The other important dimensions for the comb drive are summarized in Table 8.

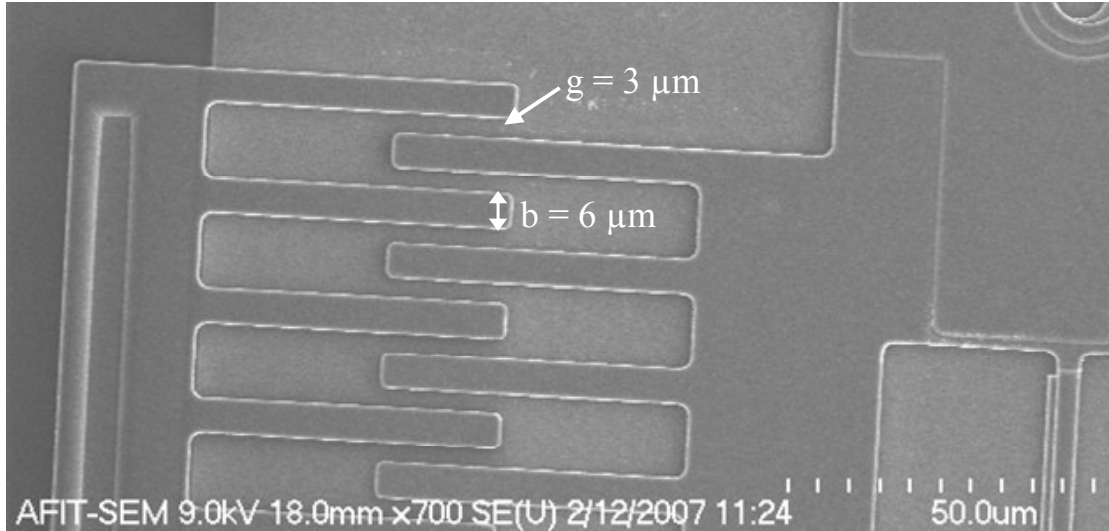


Figure 64: SEM image illustrates the important dimensions of the fabricated comb drive fingers.

Table 8: Important comb drive dimensions for the fingers and springs.

Finger Dimensions (μm)	
Width	6
Thickness	3.5
Gap	3
Length	50
Overlap	20

Spring Dimensions (μm)	
Length	250
Width	4
Thickness	3.5

Figure 65 (A) shows the large Poly1/Poly2 spring design at rest before a bias signal is applied. Figure 65 (B) shows the same resonator which oscillated at 7,510 Hz with a 0 V to 200 V saw tooth waveform applied to the right hand side combs. With the

200 V waveform applied, the shuttle achieved a lateral displacement of approximately $\pm 13 \mu\text{m}$ from the equilibrium position.

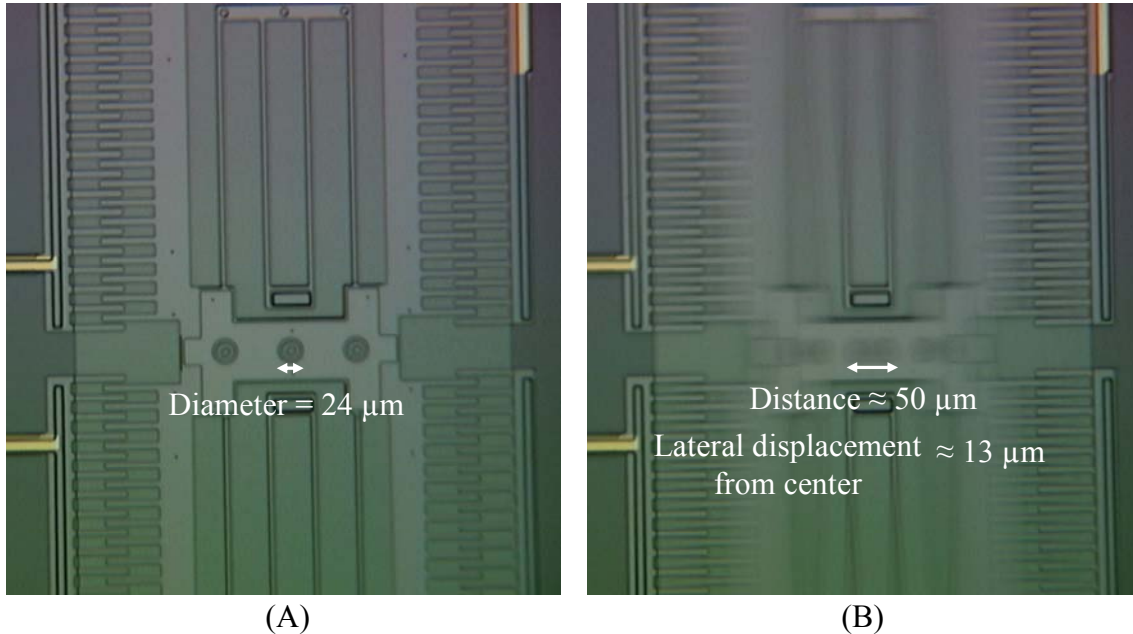


Figure 65: Image (A) is the large Poly1/Poly2 spring system CD with a $24 \mu\text{m}$ diameter etch hole labeled. Image (B) shows the same structure oscillating at $7,510 \text{ Hz}$ with a 0 V to 200 V saw tooth wave being applied to the right hand side combs.

Another Poly1/Poly2 large CD shown in Figure 66 (A) is at rest and in Figure 66 (B) the CD is under an $11,310 \text{ Hz}$ drive frequency of a 0 to 200 V saw tooth waveform. At this applied frequency, the shuttle displacement was approximately $\pm 26 \mu\text{m}$ from center. For clarification, the frequency of oscillation of the shuttle was not verified, just the driving frequency was used for the calculations.

The amount of displacement in the shuttle ranged from $13\text{-}26 \mu\text{m}$ depending on the frequency and type of waveform used. This is over double what was predicted by the analytical and FEM calculations which were done in Section 4.3. The discrepancy in the predicted verses experimental results could have come from releasing the structures too

long in HF. The springs would have thinned, reducing the spring constant. The FEM and analytical calculations are also more of a steady state prediction of performance; the frequency of operation is not part of the equations.

The total displacement magnitude of $26\text{ }\mu\text{m}$, shown in Figure 65, is desirable for the design where there are two comb resonators linked together orthogonally to rotate a geared wheel. The toothed “pusher” design principle can be seen in Figure 67.

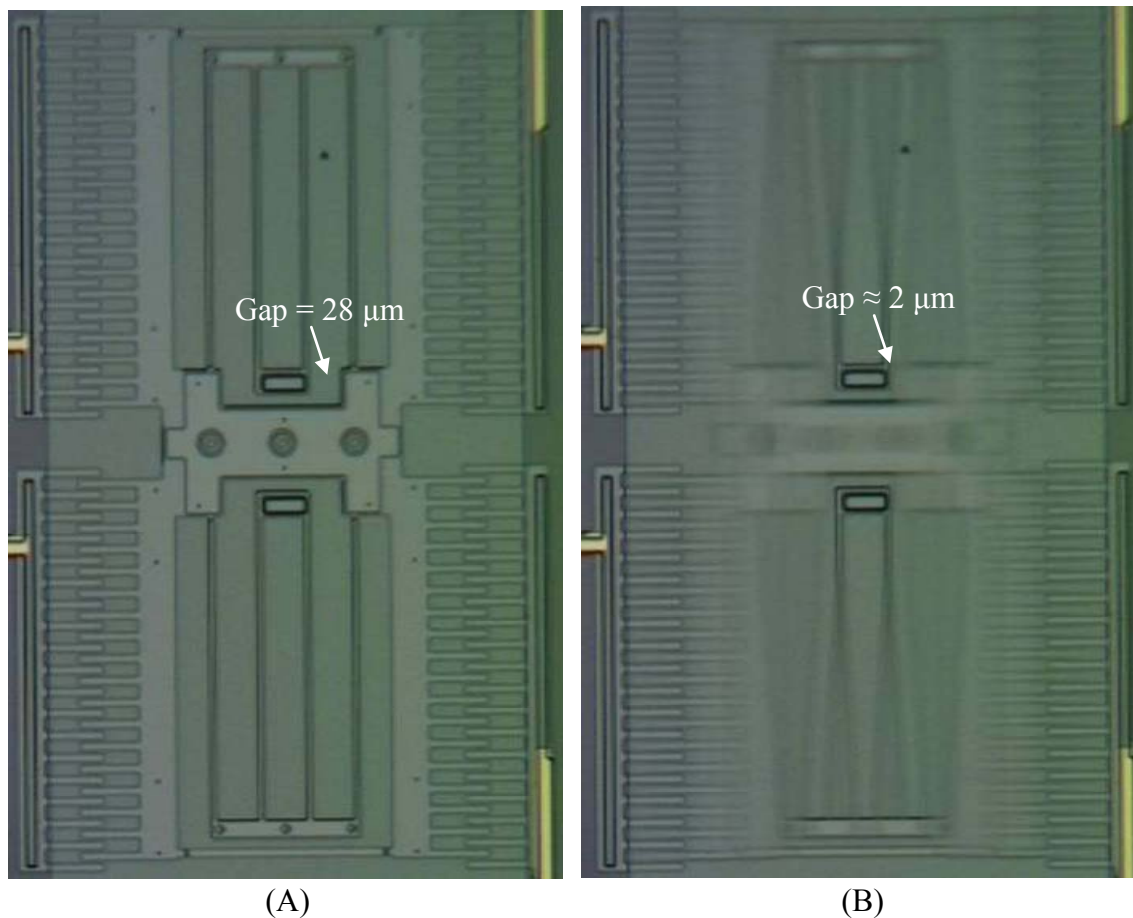


Figure 66: Image (A) is the large Poly1/Poly2 spring system CD with a $28\text{ }\mu\text{m}$ gap between the shuttle and the anchor. Image (B) shows the same structure oscillating with a drive frequency of $11,310\text{ Hz}$ with a 0 V to 200 V saw tooth wave applied, causing $\pm 26\text{ }\mu\text{m}$ of displacement from center.

Travel in the “pusher” of $26\text{ }\mu\text{m}$ would allow the wheel to rotate 2 teeth per period. If the two linked resonators oscillated at the same frequency, so the “pusher” and the “clutch” were 90° out of phase, the geared wheel would turn at a rate of 250 Hz. Following the similar example, the comb drive shown in Figure 66 with $52\text{ }\mu\text{m}$ travel in the “pusher” would allow for the geared wheel to turn 4 teeth per period. Two orthogonal drives could rotate the geared wheel at a rate of 754 Hz.

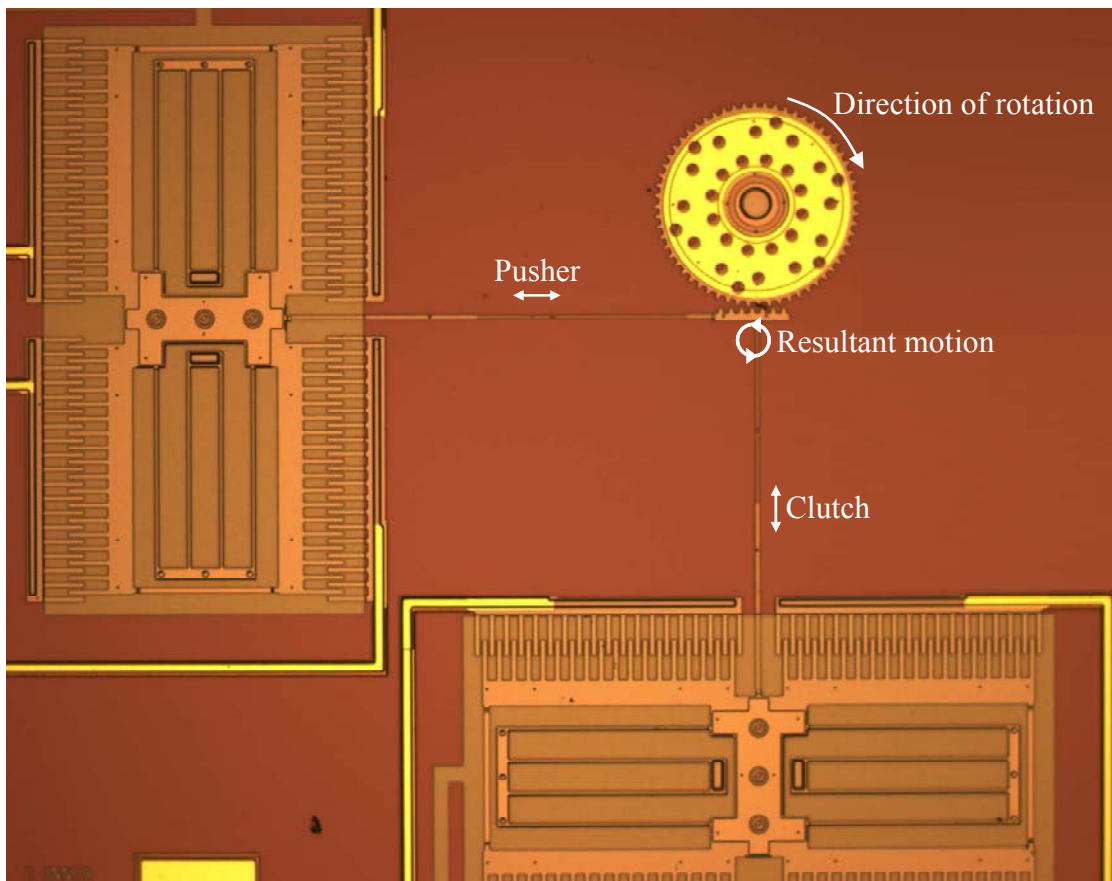


Figure 67: Orthogonally linked comb drives should operate 90° out of phase to turn circular gear.

When the comb drives are connected to each other via the toothed “pusher” link, unexpectedly, they do not operate as desired as shown in Figure 67. When the high

voltage waveform was applied to the probe pads, the substrate is also biased to a high potential. On newly released previously unbiased chips, a continuity check was performed between the high voltage and the substrate probe pads. The multimeter registered the contacts as an open circuit. Then the same chip was tested at the 200 V driving signal and the continuity check was re-performed. Between the high voltage and the substrate probe pads, unfortunately, a measurable resistance was found. This is problematic because the toothed “pusher” is linked to the main shuttles of the two comb drives which are held at a 0 V potential. The difference in potential between the toothed “pusher” and the substrate causes a large capacitive force of attraction, preventing the comb drives from oscillating. After troubleshooting, it was concluded that the dielectric layer of Si_3N_4 broke down.

In Figure 68 the 200 V drive signal is applied and then the probe tip is used to move the toothed pusher to the pictured position. When the probe tip was moved away, the toothed “pusher” stayed in its placed position due to the capacitive attraction to the substrate. When the driving voltage was turned off, the links to the toothed “pusher” returned to their original straight shape. The Poly0 layer, which was under the shuttle, should have continued out under the linked pusher arms and under the gear. That would ensure that every moving piece was on the same surface plane and the same potential, eliminating the attraction to the substrate.

After the L-Edit drawings were inspected, it should be noted that all the anchor layers in the wiring were within 2 μm of the poly layer edges. On previous design runs, this dimension had not been a problem. The design rules require the edge of the anchor

layer be 4 μm inside the poly layer edge. On page 34 of the *PolyMUMPs Design Handbook, Rev 10.0*, an overlapping Anchor1 plus Poly1_Poly2_Via, removing Poly1, and placing Poly2 on top of this configuration can cause a substrate breach, which is possibly what occurred here. Continuity checks were performed on the unreleased die sights fabricated in PolyMUMPs run 75, all chips had no unwanted short to the substrate prior to biasing. Based on the work done by Sniegowski *et. al.*, when the spring force is small, the comb drive can operate over a wide range of frequencies [19]. Future designs should increase the electrostatic force of the combs and have extremely low springs constants.

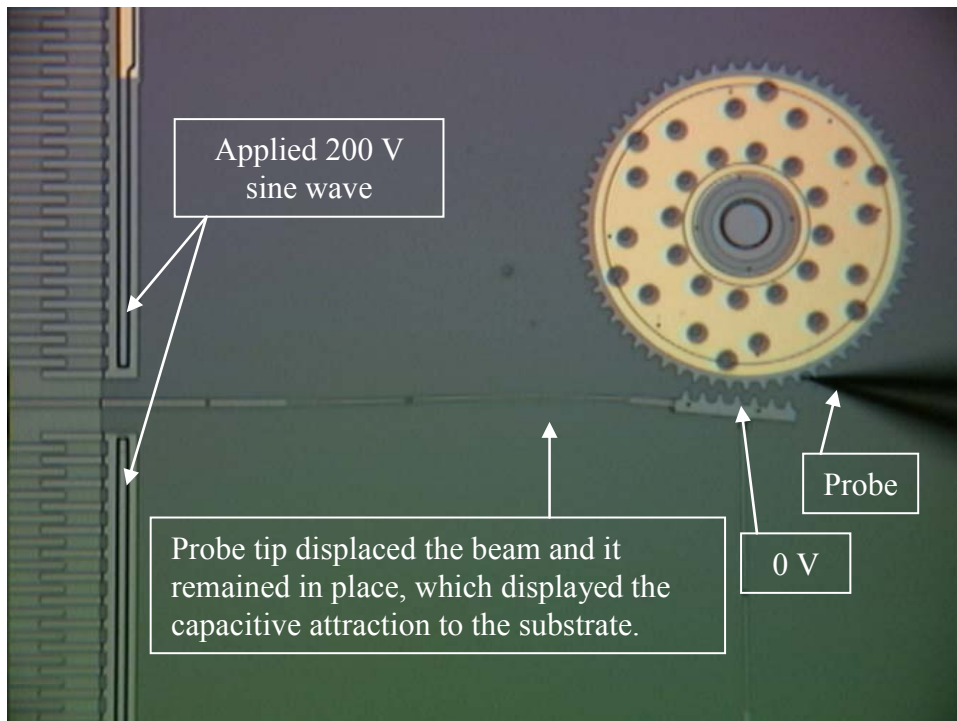


Figure 68: Due to a possible drawing/fabrication error and nitride break down, the substrate is being biased to some positive potential. The toothed “pusher” is held at a 0 V potential and is attracted to the substrate; thereby not allowing the comb drive to oscillate.

6.6 Rotor Blade Designs

Two different methods were used in attempts to achieve a desirable amount of rotor blade deflection. One method used the residual stress between the Poly2/gold layers and the other attempted to use photoresist to act as a hinge. The results of the Poly2/gold beams and rotor blades will be discussed first, followed by the photoresist hinge research.

6.6.1 Poly2/gold Rotor Blades

Before the experimental rotor designs are presented, the simple cantilever beam designs will be analyzed. As previously shown in the modeling Section 4.3, the FEM software had to be calibrated in order to produce accurate simulations. Figure 69 shows a comparison of the results obtained through analytical calculations, calibrated FEM simulations, and experimental measurements.

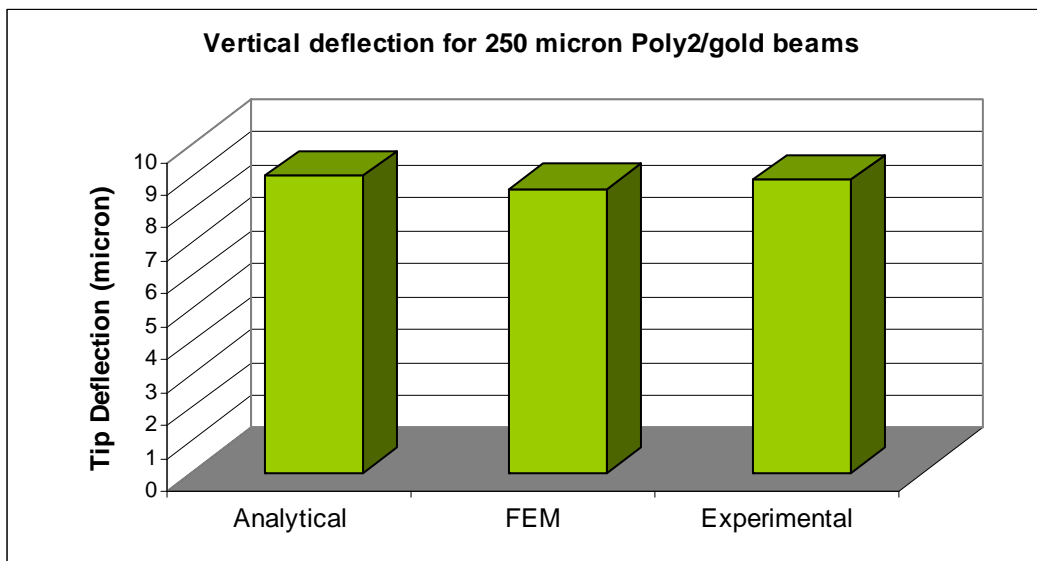


Figure 69: Graph of the three different results obtained by experiment, FEM and analytical calculations.

The analytical and FEM results very closely match the experimental results. The analytical expression was only 1.2 % higher than the experimental value. The calibrated FEM prediction was only 3.4 % lower than the measured values. Errors in the analytical expression and FEM results could have come from several places. Material properties such as the thermal coefficients of expansion for gold and Poly2, and Young's modulus for gold could be off. Another possible source of error comes from one of the assumptions made in the derivation of the equation. It is assumed that the devices are much longer than they are wide, so the stress along the width direction is assumed insignificant in comparison to the stress along the length. The aforementioned assumption worked well for the 250 μm cantilevers. Layer thickness is also an important parameter in the equations, and too much time in the HF acid releasing the structures can cause them to thin slightly.

The rotor blade deflection will now be discussed. The results for rotor model-C in Figure 38 will be discussed first. Results for the Zygo measurements are shown in Figure 70. Data provided by the software indicated a total vertical deflection of 13.1 μm and creating an angle of 3.03°. Notice the image in Figure 70 (B) is over saturated in most of the region where the light reflects directly back into the Zygo off the gold. A cross-sectional line had to be positioned directly over the polysilicon region to obtain a deflection reading. Low Reynolds number airfoils require an angle of attack between 30-45° [26]. Due to these findings, future designs must attempt to increase the angle of attack.

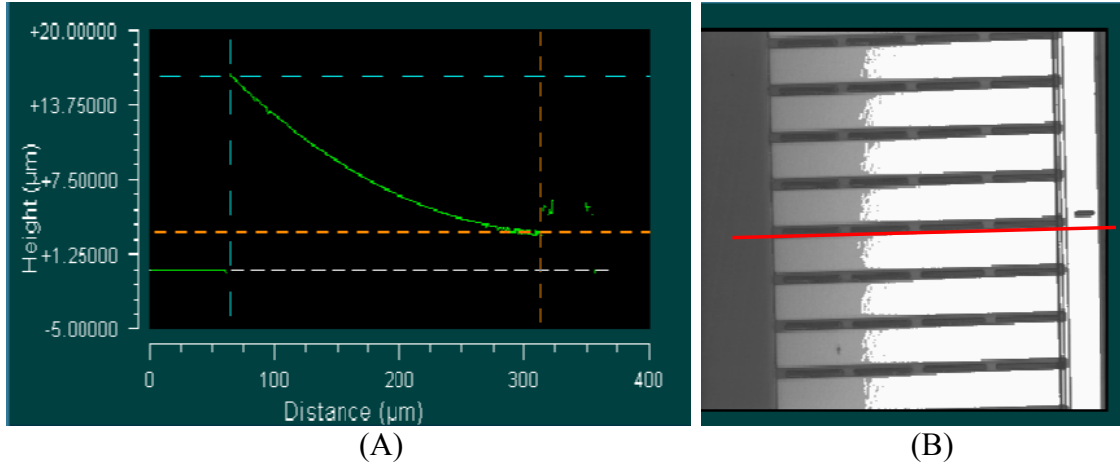


Figure 70: Deflection curve for rotor blade with a cord length of 250 μm is shown in image (A). The red line in image (B) shows the location on the wing where the cross-sectional plot was taken.

The other rotor designs could not be measured using the Zygo due to the large angle of deflection and the large amount of gold on the surfaces. Instead, the optical microscope was used to estimate the deflection of the rotor blades by using the fine focus knob and reading the scale on the dial. To ensure this practice was reasonable, deflection measurements were made using the Zygo on the Poly2/gold cantilevers and the model-C rotor blade. With a baseline established, the same devices were measured under the optical microscope. The lowest point on the Poly2/gold structure was brought into focus and the reading on the dial was logged. The highest point on the tip of structure was then brought into focus and the number on the dial was logged. Several readings were taken per structure and the results were averaged. The averaged measurements were within approximately $\pm 1.5 \mu\text{m}$ of the Zygo measurements. Table 9 shows the results of the measured deflection for each of the rotor blade designs.

Table 9: Measured vertical deflection of the rotor blade tips versus predicted.

Model	FEM Deflection (μm)	Equation (17) Analytical Deflection (μm)	Experimental Deflection (μm)	% Difference between experimental value	
				FEM vs Exp	Analyt. vs Exp
<i>A</i>	62.3	36.04	50.0	20	28
<i>B</i>	36.8	31.57	23.9	35	24
<i>C</i>	13.81	9.01	13.1	5	31
<i>D</i>	18.95	11.62	9.33	51	20
<i>E</i>	32.1	20.38	~ 10	69	51

The large disparity between the experimental and predicted deflections can be contributed to several factors. The predictions for deflection of the Poly2/gold cantilevers worked well because they were relatively short and the gold covered 80% of the 10 μm wide Poly2 beams. The rotor blade designs had Poly2 widths of 20 to 40 μm , and the gold had covered 75 to 95 % of the width. The different percentage of gold coverage on the rotor blades is not taken into account for the analytical equations. The curvature of the rotor blades made them very difficult to measure, if there is some slight dip before the blade starts to deflect upward, that portion of displacement was lost in the measurement.

Using the deflection measurements, the deflection angle or the angle of attack for each rotor blade design can be calculated. The amount of deflection θ was roughly calculated using

$$\theta = \arctan\left(\frac{O}{A}\right) \quad (27)$$

where O was the measured vertical height of deflection and A was the linear chord length of the rotor blade. The results and comparison of the deflection angles are shown in Table 10.

Table 10: Comparison of the experimental angle of deflection versus predicted.

	FEM	Analytical	Experimental	% Difference between	
Model	Angle (deg)	Angle (deg)	Angle (deg)	FEM vs Exp	Analy. vs Exp
<i>A</i>	7.1	4.1	5.7	20	28
<i>B</i>	4.3	3.7	2.8	35	24
<i>C</i>	3.2	2.1	3.0	5	31
<i>D</i>	3.4	2.1	1.7	51	20
<i>E</i>	4.7	3.0	1.5	69	51

The difference between the predicted and experimental deflection can partially be contributed to the method used to measure the deflection. The calibration check for measuring deflection only yielded errors of a few micron, but the deflection heights were not that large to begin with. The experimental results clearly show that the achieved angle of deflection is too small. Another method must be used to achieve the required angle of deflection, 30 to 45°.

6.6.2 Photoresist Hinge for Rotor Blade Deflection

A large angle of rotor blade deflection was attempted using photoresist (PR) as a hinge, similar to the work done by Miki *et. al.* On PolyMUMPs run 73, one rotor design was fabricated to implement a photoresist hinge and can be seen in Figure 83 of Appendix B. The leading edge spar is made of stacked Poly1/Poly2/gold and trapped Oxide2 to make it as rigid as possible. The blade portion is made of Poly1, to have more rigidity than Poly2 and yet lighter than a stacked Poly1/Poly2 blade. The Poly1 blade is connected to the spar by thirteen 2 μm wide by 5 μm long Poly1 tethers.

The processing steps used to apply the PR hinge will now be discussed. First the PR from the MUMPs foundry is removed by soaking the chip in acetone for 5-10 minutes, and rinsed in another acetone bath. Now the Oxide2 needs to be removed so the

PR can be in direct contact with the Poly1 blade and the spar. The chip was dipped in HF acid for 10 seconds, then into deionized water for 5 minutes. The chip was then rinsed off with methanol and blown dry with nitrogen (N₂) gas. Under the optical microscope, it was confirmed that all of Oxide2 had been removed from the Poly1 surface.

Four layers of Rohm & Haas 1818 photoresist was then applied to the chip at 4,000 RPM for 30 seconds. Between each application of PR, the chip was baked on a 110 °C hot plate for 75 seconds to dry the PR. With the four layers of PR applied, the PR thickness is approximately 2 μm. The chip was then placed in the Karl Süss MJB3 UV mask aligner using the mask shown in Figure 88 of Appendix B. The second largest width of the cross shapes was used to cover most of the spar and nearly an equal amount of the Poly1 blade. The chip was aligned under the mask and was exposed for 40 seconds at 275 W/cm² ($\lambda_0 = 405$ nm). Then the chip was placed in 351 Developer:DI solution (1:5 by volume) for 40 seconds with agitation. After rinsing in DI, the chip was dried with the N₂ gas and inspected under the microscope.

The exposure and development steps needed to be repeated and the results after the first and second sequences are shown in Figure 71. The chip designs fabricated in PolyMUMPs run 73 were squares 3.3 mm across. The edge bead created when spinning on PR was also rather wide relative to the overall size of the chip. Some remaining edge bead can be seen near the very top of image (B) in Figure 71. The next step was to release the remaining oxide by placing the chip in HF for five minutes and then rinsing with DI. The chip was then soaked in isopropyl and baked on the hot plate at 110 °C for 5 minutes.

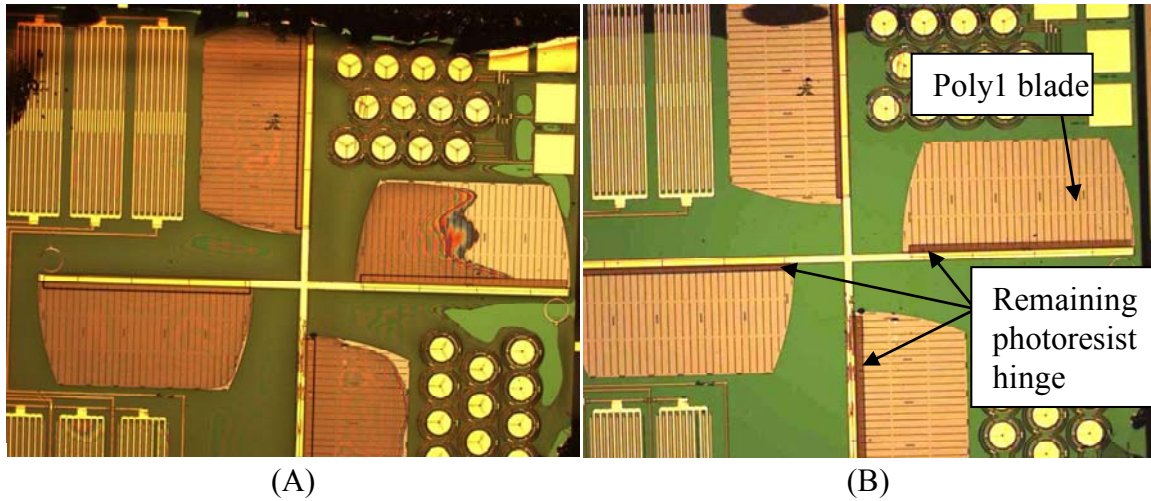


Figure 71: Image (A) shows the chip after the first step of exposure and development, a large majority of the PR is still in place. Image (B) shows the result after a second sequence of exposure and development was completed. The only unwanted remaining PR is the edge bead seen near the very top portion of image (B).

The before and after etch pictures of the rotor are shown in Figure 72. The PR in Figure 72 (A) has a uniform flat surface with crisp lines defining the edges of PR. After the released chip was baked for 5 minutes, the PR surface has rounded some.

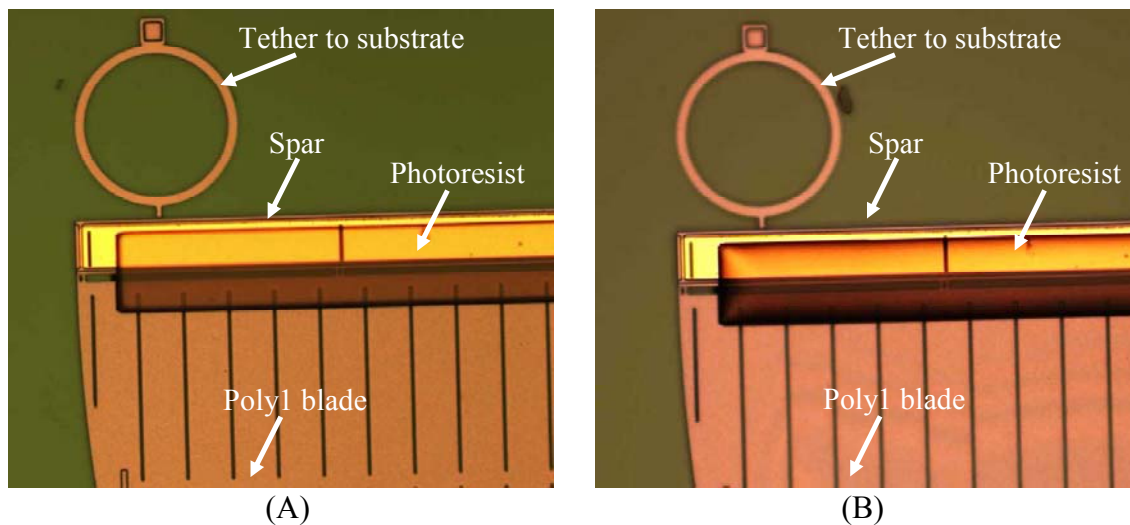


Figure 72: Four layers of Rohm & Haas 1818 photoresist are masking the spar-Poly1 blade joint in (A) prior to fully releasing the sacrificial oxides. Image (B) shows the result after five minute etch in HF acid and drying on a hot plate for 5 minutes.

No noticeable deflection was achieved from the initial attempt at bending the rotor blade up with PR. The chip was then taken to the micromanipulator to investigate why no deflection occurred. Figure 73 (A) shows the probe tip lifting the Poly1 blade off the surface. Figure 73 (B) shows the main contributing factor as to why no deflection was achieved; PR had seeped under the Poly1 blade. Small portions of Oxide1 had been removed in the brief initial etch in HF, causing the PR to adhere to the underside of the Poly1 blade and the substrate surface.

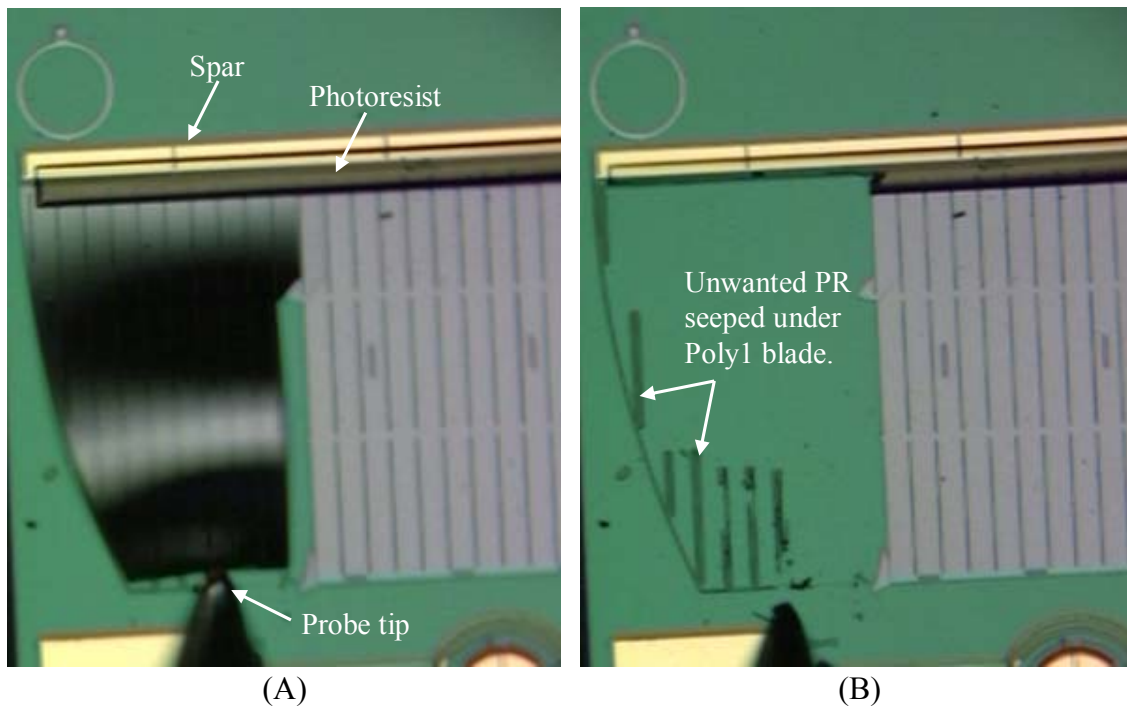


Figure 73: Image (A) shows the probe tip lifting up the Poly1 rotor blade. After that portion of the rotor blade is removed, image (B) shows the remaining PR which partially caused the rotor blade to not achieve any deflection.

Another new chip was released using HF with no PR applied. Further investigation showed that the small tethers connecting the Poly1 blade to the spar were too stiff. Using a probe tip the Poly1 blades were lifted up and a large amount of

curvature could be seen. After the blade tip was lifted away from the surface several micron, the blades would snap off the spar. The large amount of curvature in the Poly1 blade means the hinge tethers were too stiff. The stiffness in the hinges would greatly inhibit deflection. To remedy the previously mentioned two problems, the rotor design need to be modified. Figure 74 shows the improved concept that should be implemented. The improved design would have very few tether hinges or no tether hinges at all, relying on the PR to act as the structural connection. A Poly1 blade with a connected Poly2 region, as shown in Figure 74 would greatly reduce processing time and the margin for error by not having to remove Oxide2 in order to allow the PR to contact the blade.

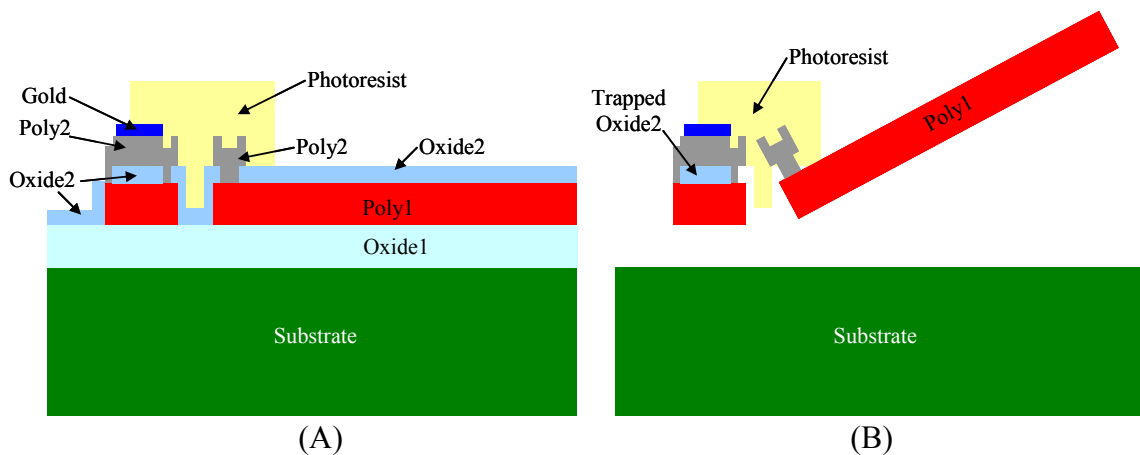


Figure 74: Image (A) shows an improved concept of the cross-section of a rotor blade with photoresist on prior to releasing the device in HF acid. The image in (B) shows how the rotor blade should look after the oxide layers are removed.

6.7 Chapter Summary

In summary, this section covered the experimental setup and testing of the following MEMS devices: circular scratch drives, three phase electrostatic motors, comb drives, and five various rotor designs. The circular scratch drive tested with Poly2/gold

wings attached was the most complete design, integrating the motor with the rotor blades attached. The simplicity of the design is also a nice feature, no flip bonding or using micromanipulators were required for assembly. The motor could rotate slowly with a 36 V waveform applied; unfortunately the maximum achieved rotational speed was less than 3 RPM.

Thirty six electrostatic motor designs were completed, with moderate success. In previous work done by Fan *et. al.*, they were able to fabricate electrostatic motors with diameters of 60 through 200 μm that could rotate at speeds of 50 – 500 RPM. The majority of the motors designed in this work had diameters ranging from 120 to 220 μm . The larger diameter motors were designed in the hope that they would be able to produce more torque to turn an attached rotor blade. Not enough electrostatic force between the electrodes could be generated to turn the inner stator, let alone an attached rotor. The planar style electrostatic motors used in this research were not a viable drive mechanism to turn a rotor blade on a MAV.

The comb drive designs done in this work depended on the resonant frequencies to oscillate and were successfully demonstrated. The comb drives all performed well except when they were connected together orthogonally. It was discounted that a Poly0 layer was needed below the connected pusher arm. That would have ensured the pusher arm and the Poly0 would be the same potential, preventing electrostatic attraction to the substrate. Similar comb drive designs done here could be implemented on a larger scale to propel a MAV and will be discussed further in Chapter 7. The complete summary of

the motor performance done in this work is shown in Table 11 compared to other state of the art motors.

Table 11: Summary of motor performance done in this work compared to other state of the art motors.

Motor Type	Experimental Rotational Rate	Best performance by other Designers
Scratch Drive	0 – 3 RPM	0 – 180 RPM
Electrostatic Motor	No complete rotation	0 – 500 RPM
Comb Drive Motor	No rotation, but 45,000 RPM (potentially)	0 – 300,000 RPM

The Poly2/gold rotor blade designs did not provide a large enough angle of deflection. The rotor with the best deflection achieved an angle of attack of 5.7° , which is 24.3° less than desired. The photoresist hinge method must be used to achieve the desired amount of deflection. Design changes must be implemented on the rotor to make bending the hinge easier.

VII. Conclusions and Recommendations

The following sections will discuss the conclusions drawn from this research and recommendations for future work on MAV design.

7.1 Conclusions of Research

Flight on the millimeter scale can be achieved, with modifications made to the current designs. The scratch drive with attached rotors was elegant in its simplicity, but operated far too slowly. The scratch drive used could be optimized, but it still would not rotate fast enough to achieve lift.

The hope was to improve the performance of the planar electrostatic motor that others had done previously, which rotated at 8.33 Hz which is much too slow for a rotor on the millimeter scale. The electrostatic motor designs in this work improved over the four fabrication runs, although successful rotation did not occur, some movement was noted. Single stator bank planar electrostatic motors are most likely not a viable motor for a MAV.

Comb drive actuation has shown to be the most viable means of turning a rotor. The ability to operate over a range of frequencies and shuttle displacements is a desirable feature. The missing Poly0 layer under the linked pusher arms could be easily corrected for future fabrication runs. The spring constant of the orthogonally linked comb drives only slightly increased over the completely independent comb drives. This means the operation of the linked comb drives would have been very similar to the independent ones.

The mask design created for mounting the rotor blades with photoresist to either an electrostatic motor or toothed gear would have provided good electrical isolation. This is necessary so the rotor blades would not be attracted to the biased features below them. The theoretical collar mounting system devised for the electrostatic motors and rotor blade mounting was not implemented in this work. The use of the micromanipulators involved too much physical assembly, and more importantly, would not ensure good electrical isolation.

The best performing Poly2/gold rotor blade design had a 500 μm chord length and achieved a 5.7° angle of attack. The Poly2/gold rotor blade designs did not cause enough deflection to create the desired angle of attack. A photoresist hinge system will have to be used to generate the needed deflection in the rotor blade. The rotor design done in this research for photoresist hinge bending showed Poly1 was the wrong layer of material to use for the blade and that the tethers used were too stiff. Removing only the Oxide2 layer to expose Poly1 proved too time consuming and a poor design. A Poly2 blade would have required no initial HF etch and PR could not have gotten under the blades. Two-hinge tethers or no-hinge tethers would have produced better results. Rotor designs required significant real-estate, which limited the number of variations that could be done.

7.2 Recommendations for Future Research

More MAV research needs to be done on millimeter-scale rotary aircraft. Advanced fabrication processes, similar to the SUMMiT V process or other high aspect ratio processes, must be utilized and improved upon to make flight on the millimeter

scale a reality. For example, thicker layers with smaller gaps between the comb fingers would greatly increase the area of capacitive interaction in comb drive motors. A larger capacitive area means lower operating voltages, which would lead to increased performance by reducing the voltage requirements of the MAV.

The proposed design for future work is shown in Figure 75. This design is still less than a centimeter in size and would operate with banks of comb drives. Individual comb drives would be linked together to form a bank, all biased to move in the same direction to generate more force. The design changed from a two-rotor system to a four rotor system due to the orthogonal arrangement of the comb drives. Had the system been built with only two rotors, the structure would have had poor symmetry, potentially causing an imbalance. Each time one of the two main banks of comb drives is actuated, they would be causing rotation in one of the two rotors they are connected to.

The MAV shown in the top portion of Figure 75 is being viewed from the bottom and in the lower portion of Figure 75 shows the MAV from a side view. The angle of deflection in the rotor blades needs to be so large it would prevent them from being mounted deflecting toward the surface of the MAV. The deflection of the rotor blades needs to be away from the surface, so the mounting connection could be made thinner. Since the rotor blades would be mounted on the bottom of the MAV, legs or posts would need to be in place so the device could land without damaging the rotors. Each rotor of the proposed design would generate 40 times more thrust than the model-4 rotor fabricated in this work, assuming they were turning at the same rate. With the advances

in solar cell technology and the larger size of the envisioned MAV, a solar cell could generate enough power to actuate the comb drives.

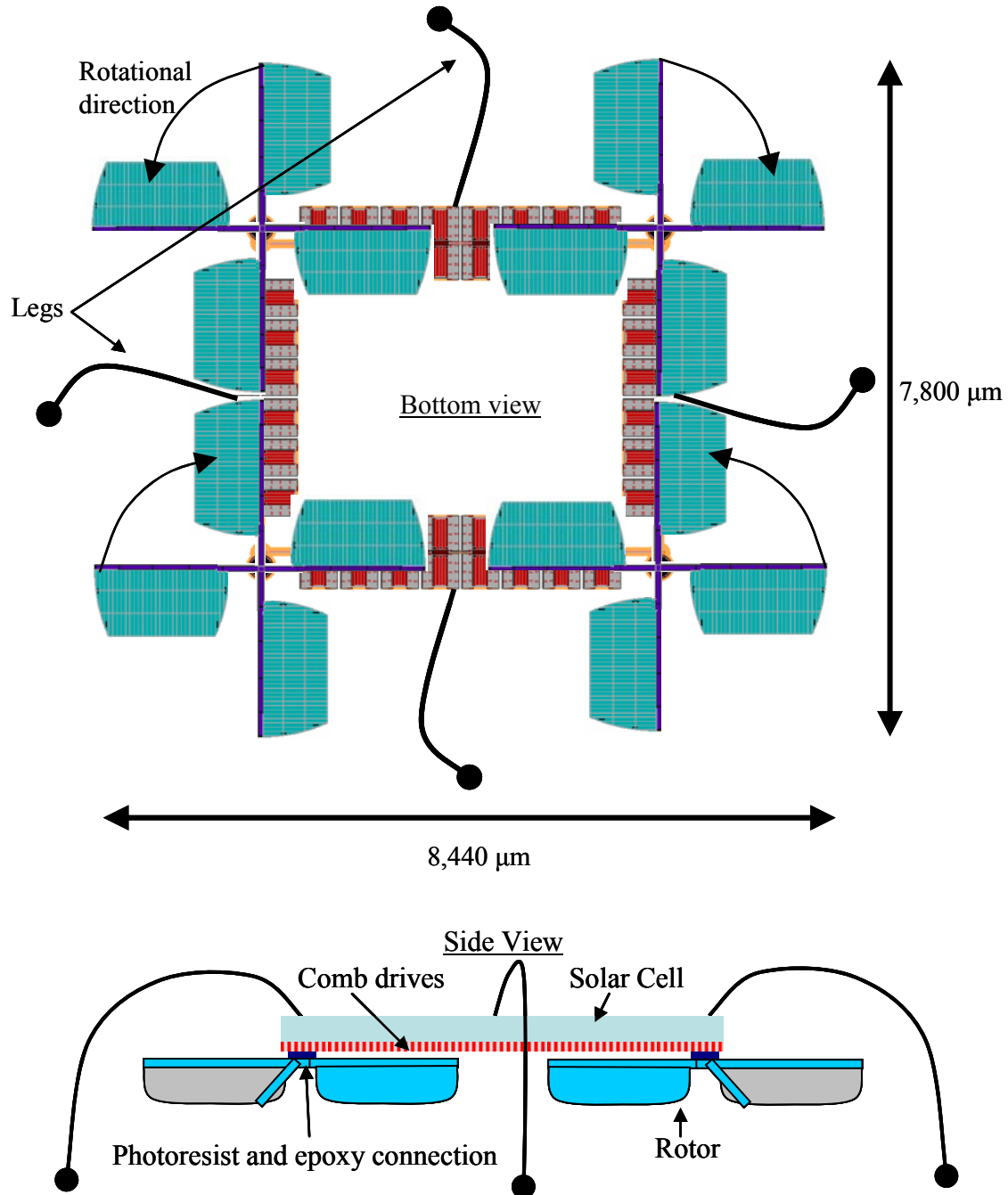


Figure 75: Proposed design would consist of four rotors with two independent banks of pusher comb drives and four small independent clutch comb drives. Views shown are from the bottom and side respectively.

7.3 Summary

Flying robots less than a centimeter in diameter will emerge more frequently over the next few years. The needed micromachining technology exists today, but fabrication costs and an onboard power sources are the main prohibitive factors preventing flight on the millimeter scale. Starting on a slightly larger scale than desired and progressively making the designs smaller will most likely be the path to success for creating millimeter-scale MAVs.

The following are a few recommendations for those who continue work on the design of a micro air vehicle. Get started early; equipment fails, ordered parts maybe out of stock, and the best devised plan may contain the smallest error, rendering devices useless. To maximize your likelihood of success, review designs with colleagues and mentors weeks prior to design submission deadlines. Waiting until the last minute can lead to missed minor errors which could mean the difference between the success and failure of the device. Most importantly stay positive, success will come with hard work and some creative thinking.

Appendix A: L-Edit Mask Designs for PolyMUMPs Fabrication

Appendix A consists of all of the PolyMUMPs designs that were submitted for fabrication, starting from run 71 through run 75. The second round of designs was typically due only days after the first designs were received back from the foundry. This made it difficult to implement significant improvements in the designs until the third run of the sequence.

Below each of the following figures, a brief description of the layouts is given, which highlights the important devices or features. Information on the predicted operation and some of the experimental results may also be given. Several times, die space was shared between students to maximize coverage. Designs completed by other students are grayed out and the specific designer is named.

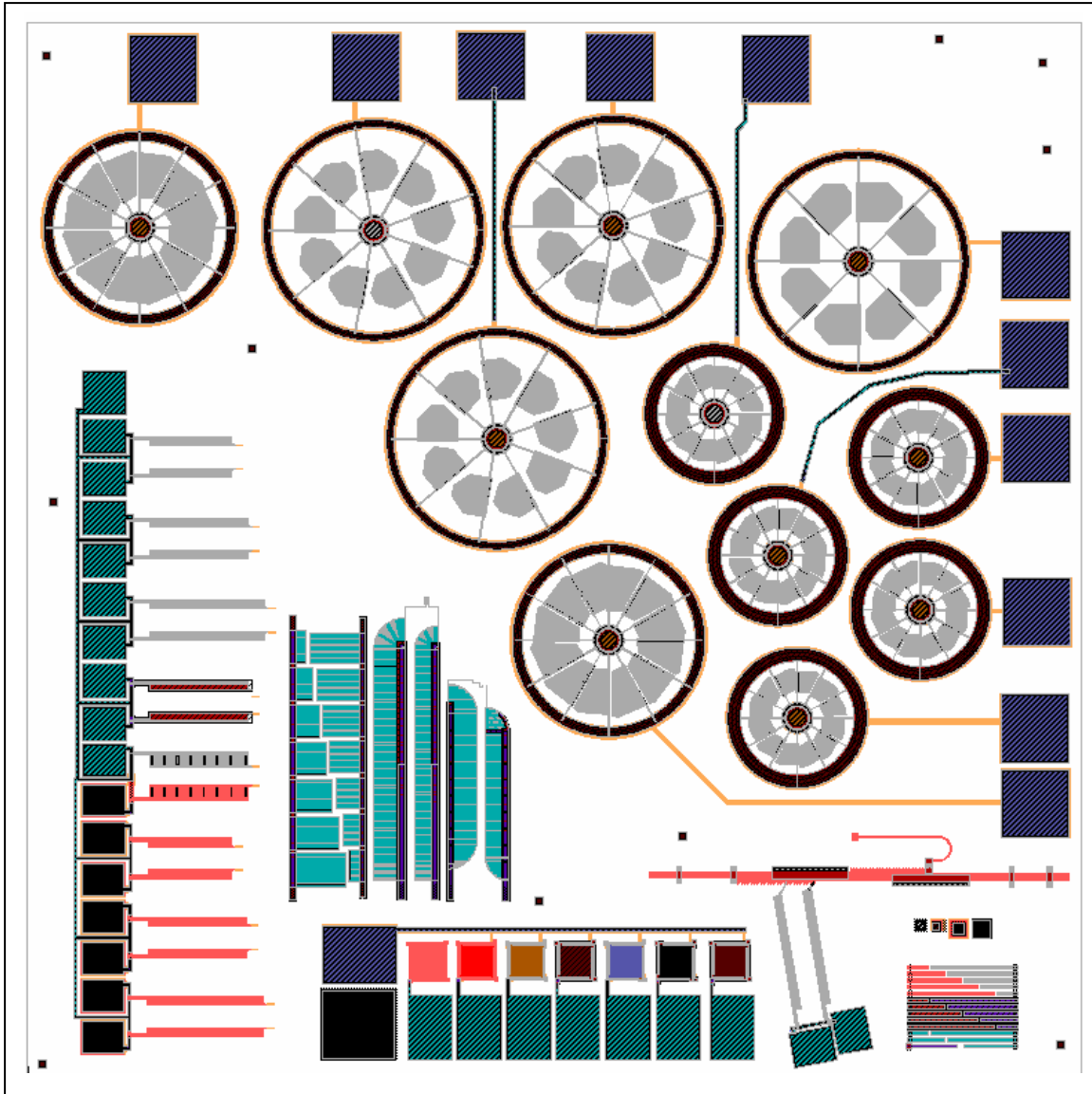


Figure 76: MUMPs® 71 Glauvitz Chip 1 scratch drives and test structures.

MUMPs® run: 71 (original designs, EENG 636 homework assignments, and [47])

Layout: Circular scratch drives, vertical deflecting micro-mirrors, single arm thermal actuators, residual stress cantilevers, rotor blade designs, and ratcheting device [47].

Comments: Scratch drives – several different plate styles were attempted as plate length plays an important role in the required operating voltage. Several of the designs attempted to maximize the number of plates and plate length. Unfortunately some plates were too big and did not fully release after being etched in acid for more than 7 minutes. The majority of the thermal actuators and mirrors operated well. The rotor blades proved to have too little deflection and their cord length needed to be increased.

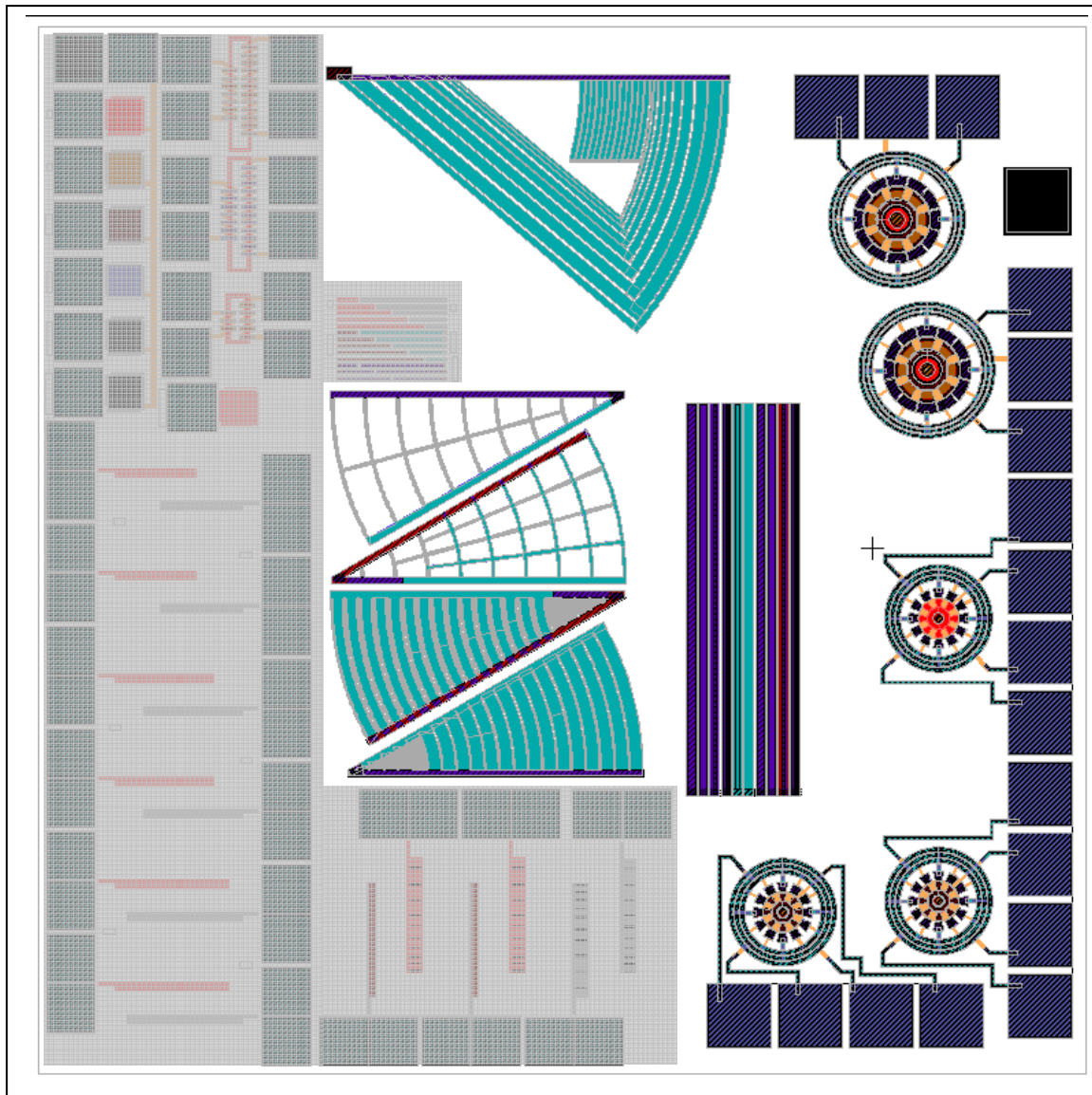


Figure 77: MUMPs® 71 Glauvitz Chip 2 electrostatic motors and rotor test structures.

MUMPs® run: 71 (original designs and motor design ideas from multiple sources)

Layout: Rotor blade designs, large cantilever beams and electro-static motors.

Comments: There are five different rotor wing designs on Chip 2, the deflection proved difficult to measure on the IFM due to the steep angles. All of the electrostatic motors on this run failed to operate as desired although slight movement did occur for a very brief instant. Fragments of polysilicon off the stators or electrodes would short the devices out just after power was applied. The grayed out region are designs from a fellow student, Jason Paul.

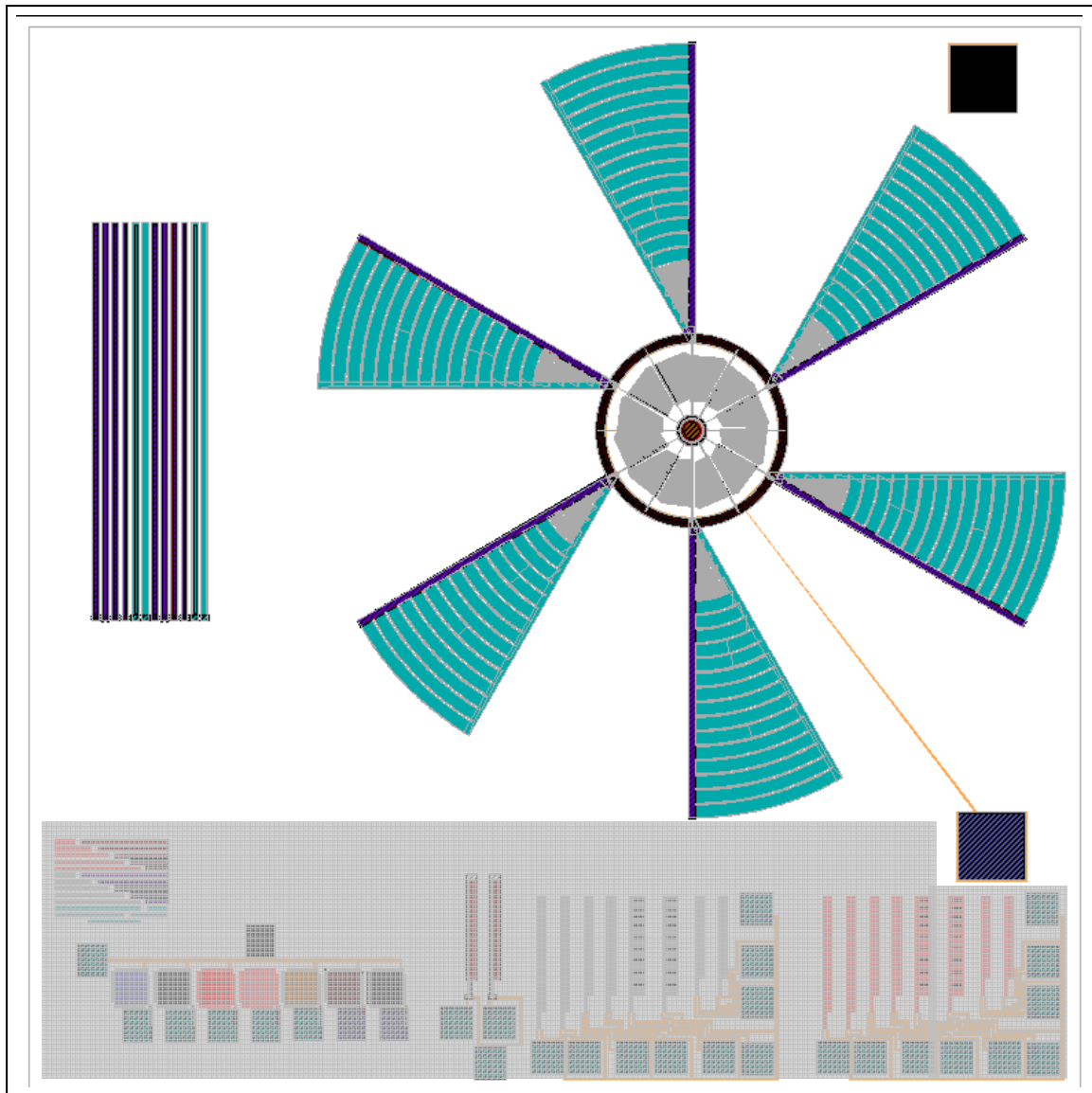


Figure 78: MUMPs® 71 Glauvitz Chip 3 scratch drive with rotors and large cantilever beams.

MUMPs® run: 71 (original designs)

Layout: Scratch drive with rotor blades and large cantilever beams.

Comments: This scratch drive with rotors attached did not function because the large rotor area was strongly attracted to the grounded substrate causing too much friction. The solution to this problem is to put Poly0 under the entire device as shown in Figure 85. The grayed out region are designs from a fellow classmate, Karl Schwenn.

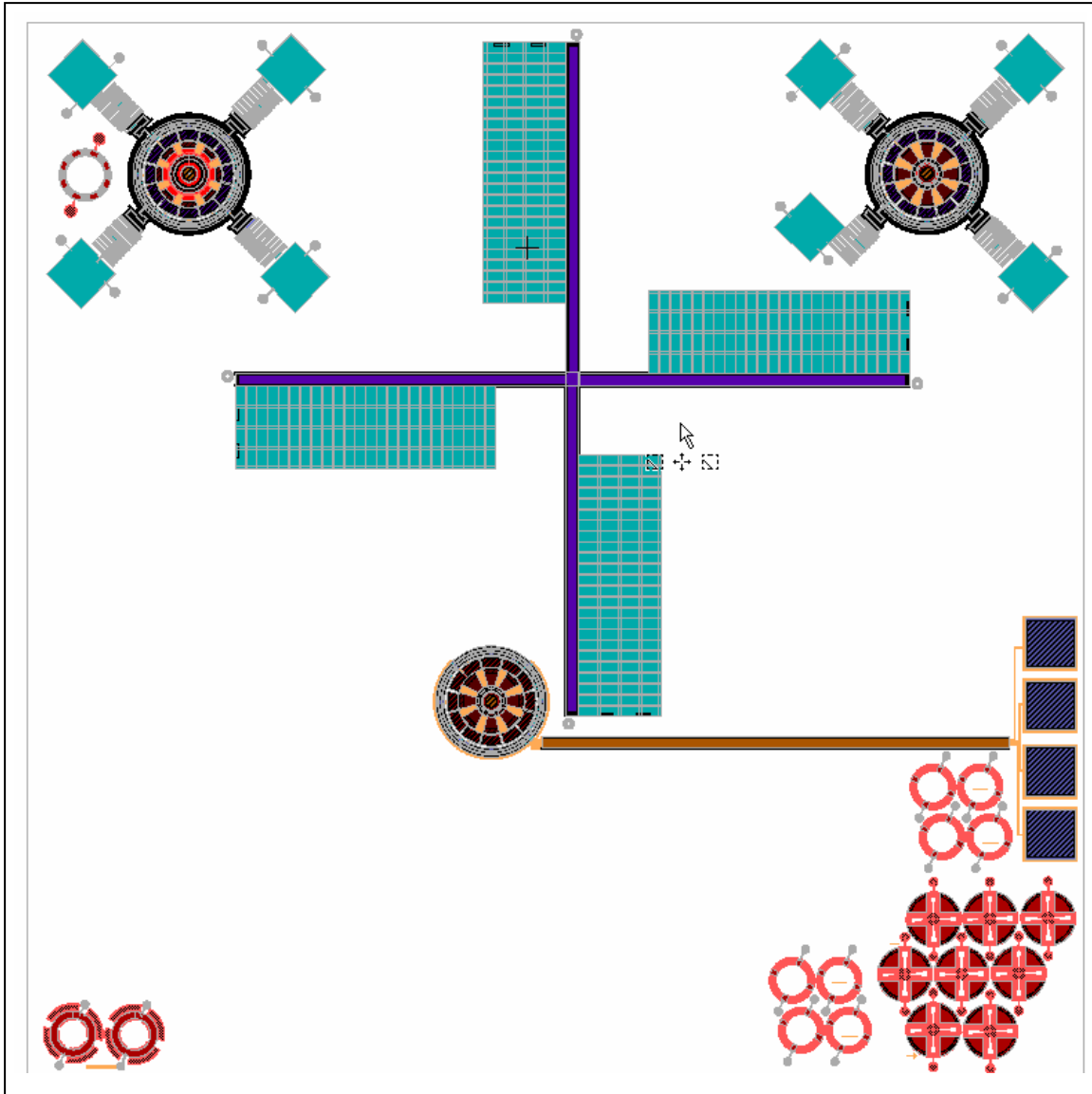


Figure 79: MUMPs® 72 Glauvitz Chip 1 electrostatic motors with rotor mounting collars.

MUMPs® run: 72 (original designs)

Layout: Test fixtures for rotor design with two other electrostatic motors.

Comments: The electrostatic motors did not work as they suffered from the same poly stringers as the previous designs, shorting out when power was applied. The rotor mounting collars proved very difficult to handle, something needed to be added to make maneuvering them easier.

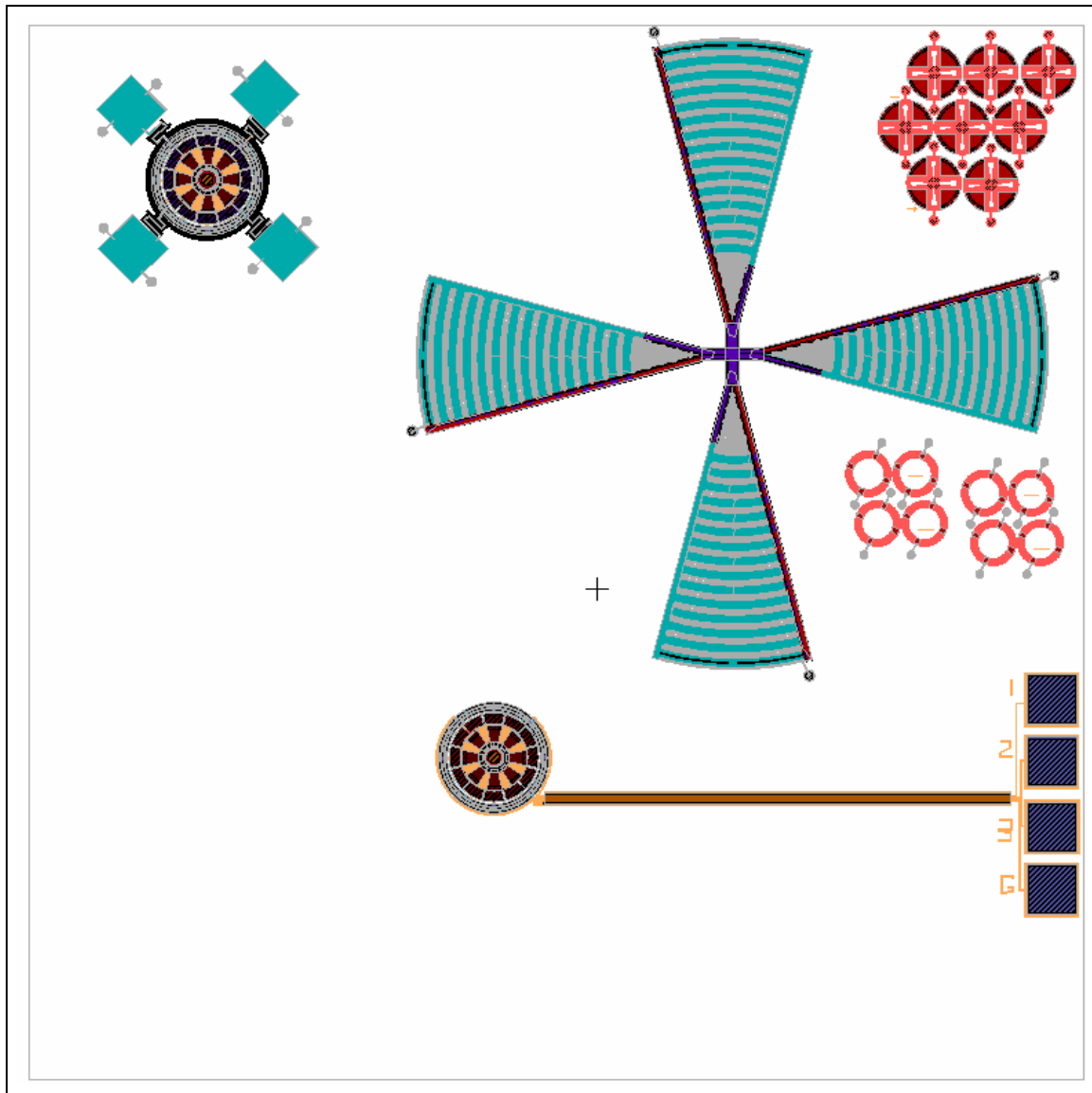


Figure 80: MUMPs® 72 Glauvitz Chip 2 electrostatic motors with rotor mounting collars.

MUMPs® run: 72 (original designs)

Layout: Test fixtures for rotor design with one other electrostatic motor.

Comments: The status of the electrostatic motors is the same as mentioned on the previous page. Another rotor design is shown with a longer chord length.

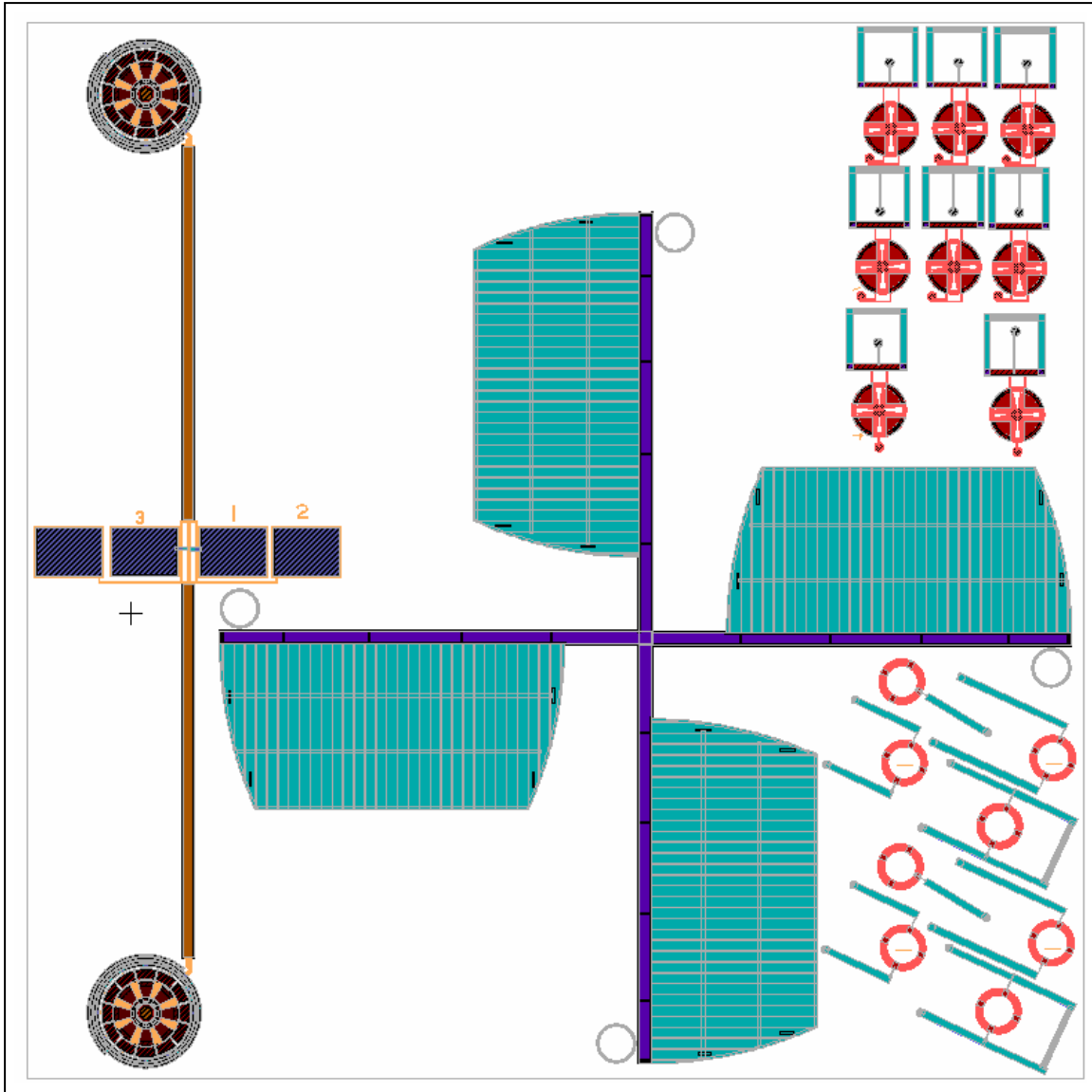


Figure 81: MUMPs® 73 Glauvitz Chip 1 electrostatic motors with rotor mounting collars.

MUMPs® run: 73 (original designs)

Layout: Dual electrostatic motors which turn in opposite direction along with fitting collars to mount the rotors.

Comments: The rotor blade dimensions were doubled from spar to leading edge in an effort of increase the vertical deflection compared to the rotor in Figure 80. The double motor design can be seen on the left side of the chip. The motors are wired to turn in opposite directions. In an effort to make the micromanipulation easier, carrier structures have been added to the motor attachment rings. These electrostatic motors were designed the same as the previous two runs and did not function properly.

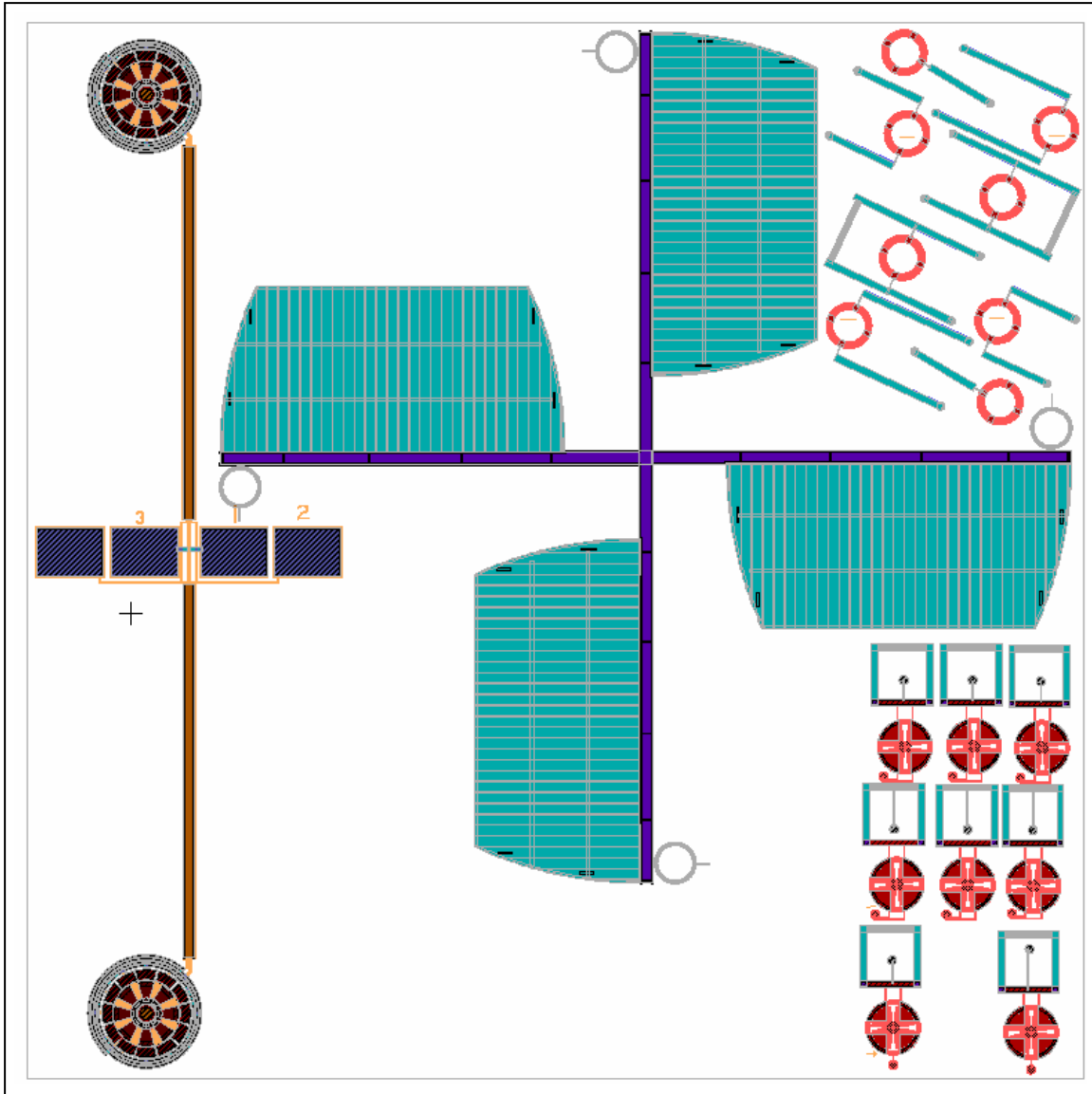


Figure 82: MUMPs® 73 Glauvitz Chip 2 electrostatic motors with rotor mounting collars.

MUMPs® run: 73 (original designs)

Layout: Dual electrostatic motors which turn in opposite direction along with fitting collars to mount the rotors.

Comments: The rotor from this chip was fabricated to turn in the opposite direction of the rotor seen in Figure 81. There is a slight difference in the motor design; the gap from the rotor to stator is 1 μm larger. The poly stringers still existed, shorting the motors out.

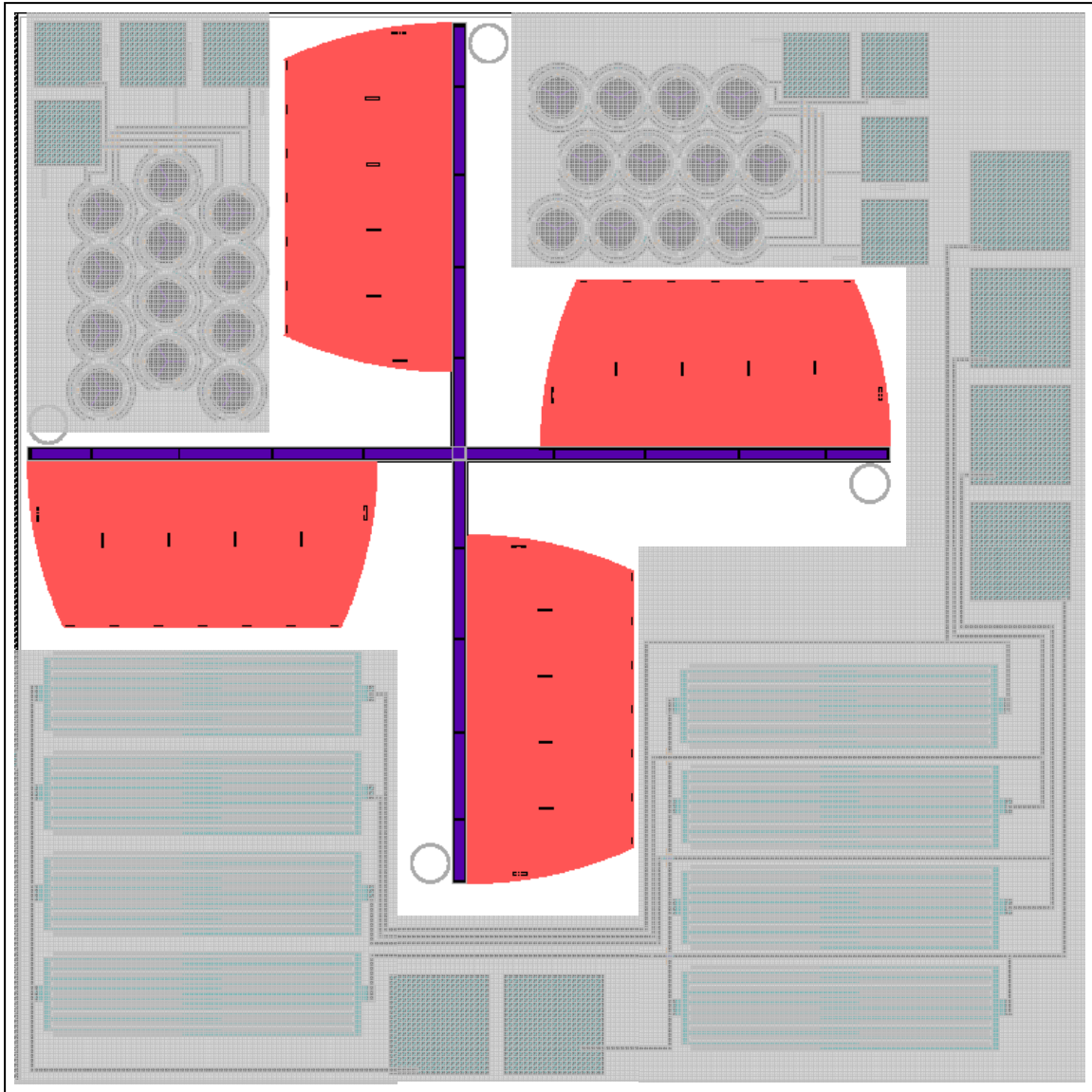


Figure 83: MUMPs[®] 73 Glauvitz Chip 3 with rotor designed for photoresist hinge.

MUMPs[®] run: 73 (original designs)

Layout: Rotor design which would rely on a polyimide hinge to achieve the desired blade deflection.

Comments: The rotor blade design made of Poly1 was a poor choice. The Oxide2 layer had to be removed before the photoresist hinge could be applied. A better design would be to make the rotor blade out of Poly2/gold with no connection hinges or very few connection hinges between the spar and the blade. The current hinge configuration is too stiff. The grayed out regions are designs from fellow classmates, Mark Allard and Matthew Johnson.

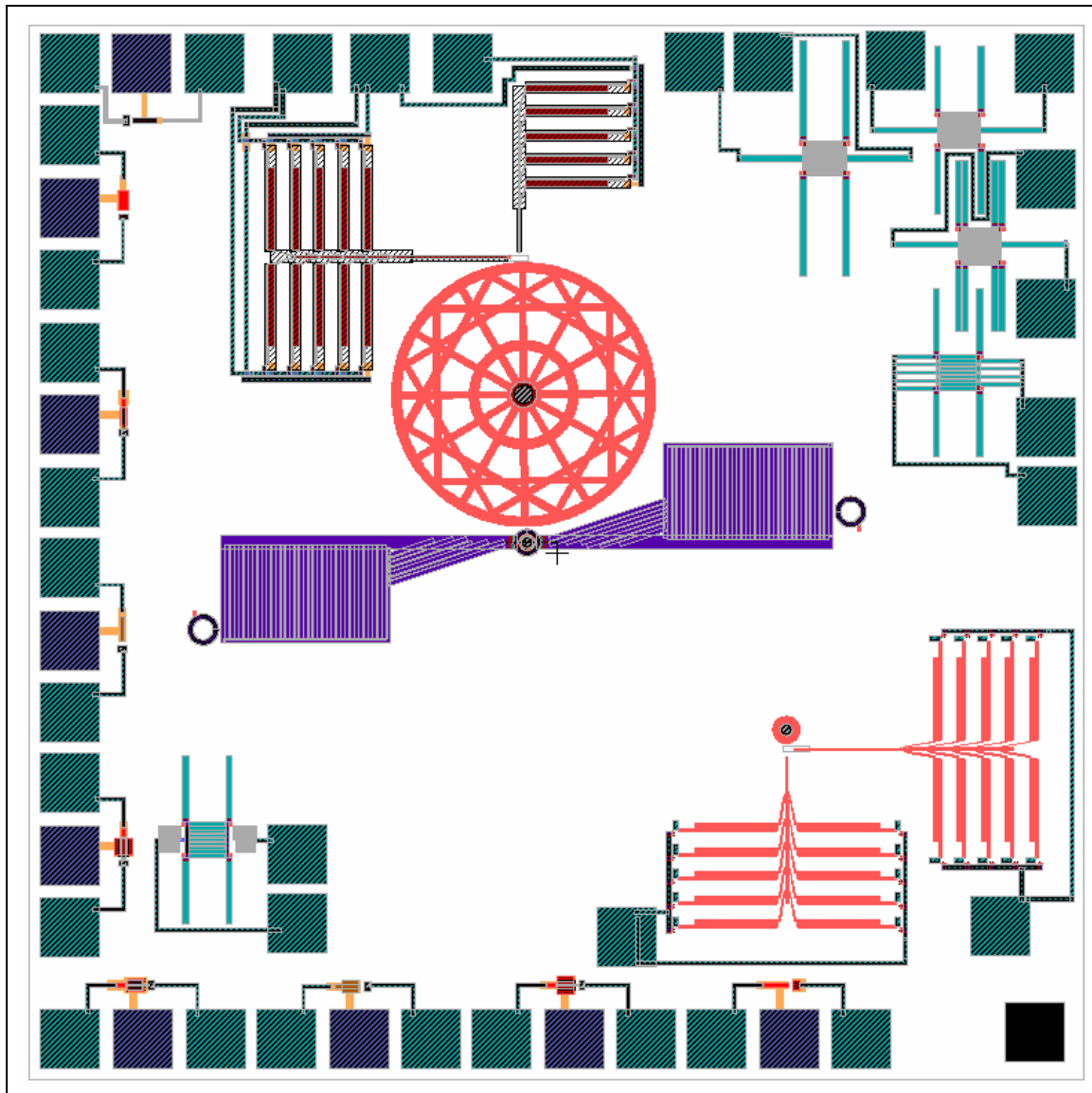


Figure 84: MUMPs® 74 Glauvitz Chip 1 thermal actuators drive a gear system.

MUMPs® run: 74 (original designs)

Layout: Arrays of thermal actuators to rotate wheels, sample switches, sensor designs.

Comments: The thermal arrays pictured moved but could not turn the toothed gears. It was most likely a combination wiring and yoke connection problems, the thin connection regions were fused together, decreasing the amount of possible bending length.

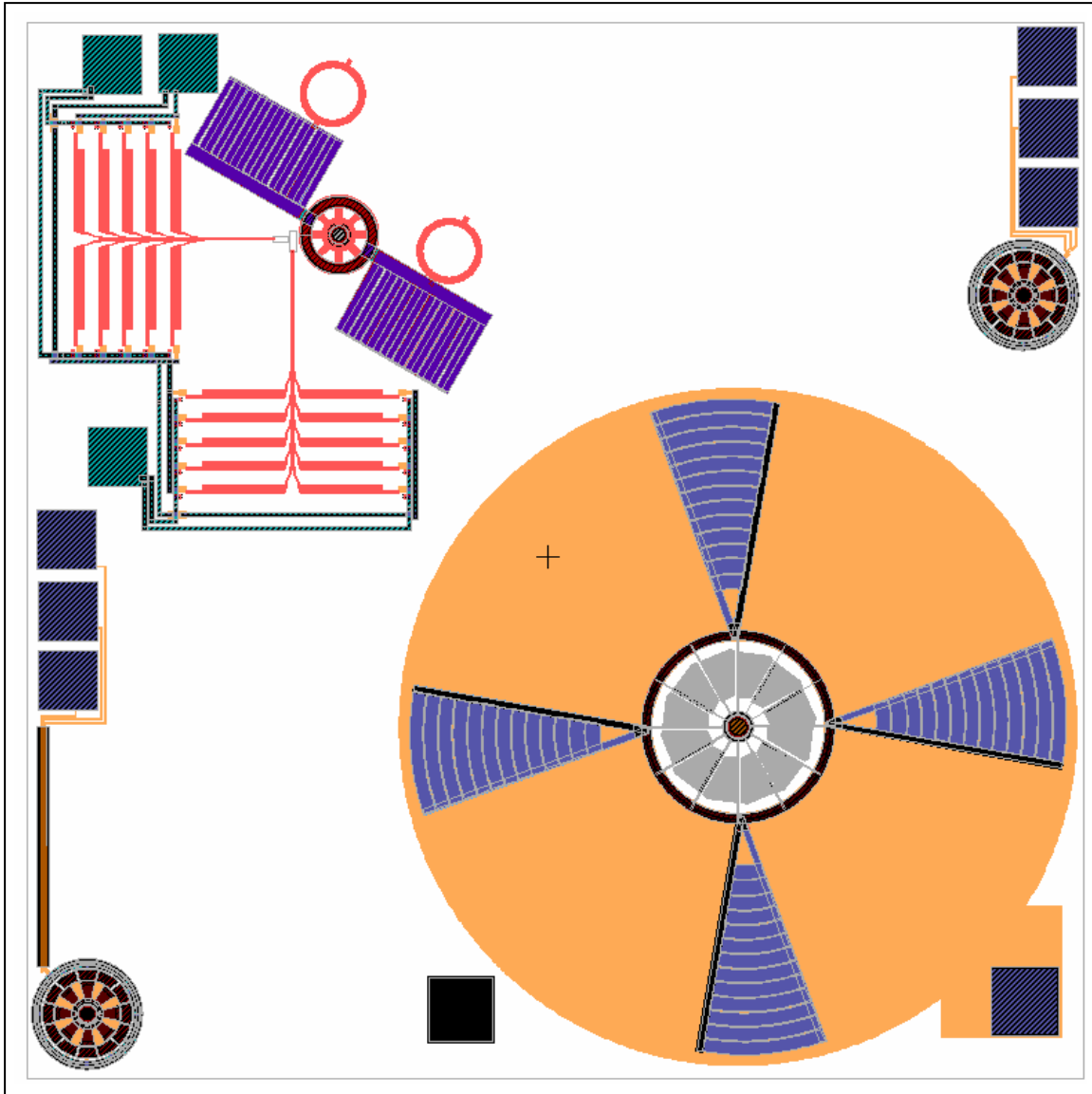


Figure 85: MUMPs[®] 74 Glauvitz Chip 2 contains a scratch drive with rotors, electrostatic motors, and thermal actuator array driving a gear with wings.

MUMPs[®] run: 74 (original designs)

Layout: Scratch drive with rotors, electrostatic motors, and thermal actuator array driving a gear with wings.

Comments: The large SDA motor with wings did rotate at just less than 3 RPM. The thermal devices actuated, but they couldn't turn the tooth gear. The electrostatic motors shorted out immediately after power was applied.

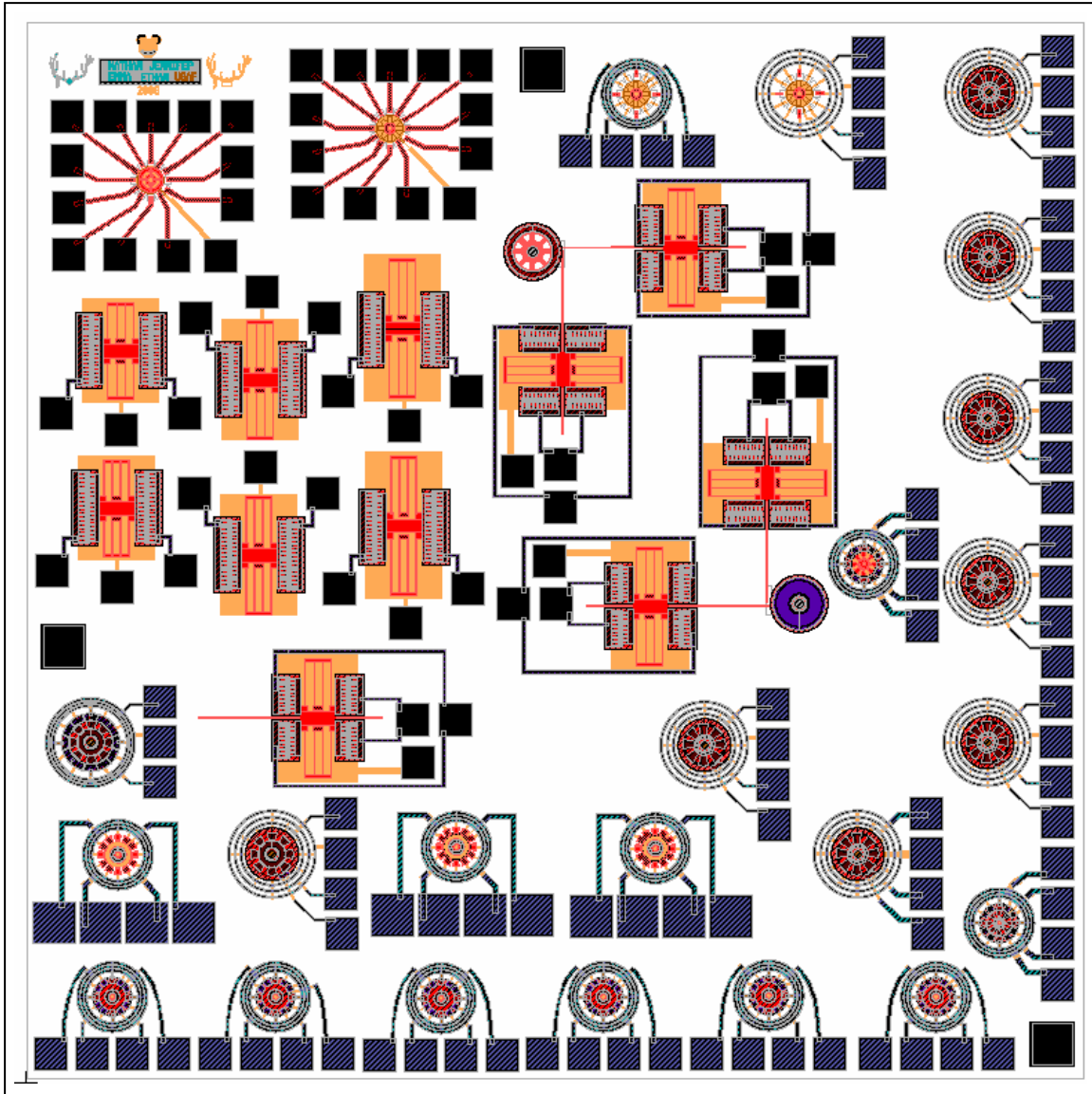


Figure 86: MUMPs® 75 Glauvitz Chip 1 layout of electrostatic motors and comb drive resonators.

MUMPs® run: 75 (original designs)

Layout: Comb drive resonators, electrostatic motors, one wobble motor and sample cantilever sensor designs.

Comments: A wide variety of electrostatic motors have been done using different diameters, gap spaces, wiring widths, and layers. The poly stringers should be eliminated on nearly all of the motors done in this run. More testing on these motors could be completed; with the equipment problems, limited tests were done. All the CD worked except when the “pusher” rod was attached.

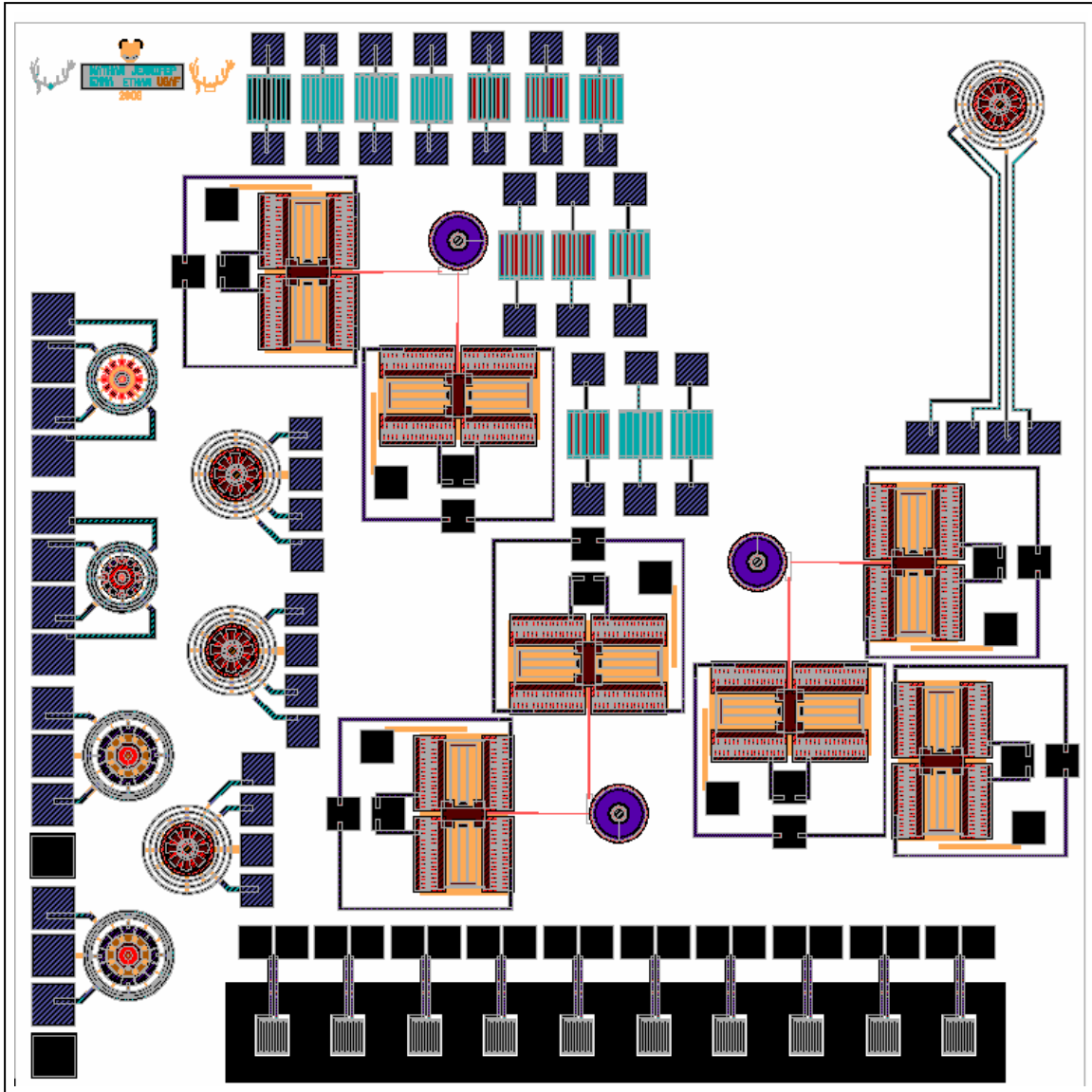


Figure 87: MUMPs® 75 Glauvitz Chip 2 has different electrostatic motors, comb drive resonators rotating a wheel and cantilever beam sensor designs.

MUMPs® run: 75 (original designs)

Layout: Comb-drive resonators, electrostatic motors, and sample cantilever sensor designs.

Comments: The large CD oscillated nicely when the “pusher” arm was not connected; Poly0 needs to be placed under the pusher arm. Only very few of the electrostatic motors were tested yielding no real results. The bottom row is a set of pixel designs for a detector.

Appendix B: Mask Designs for Rotor Mounting and Bending

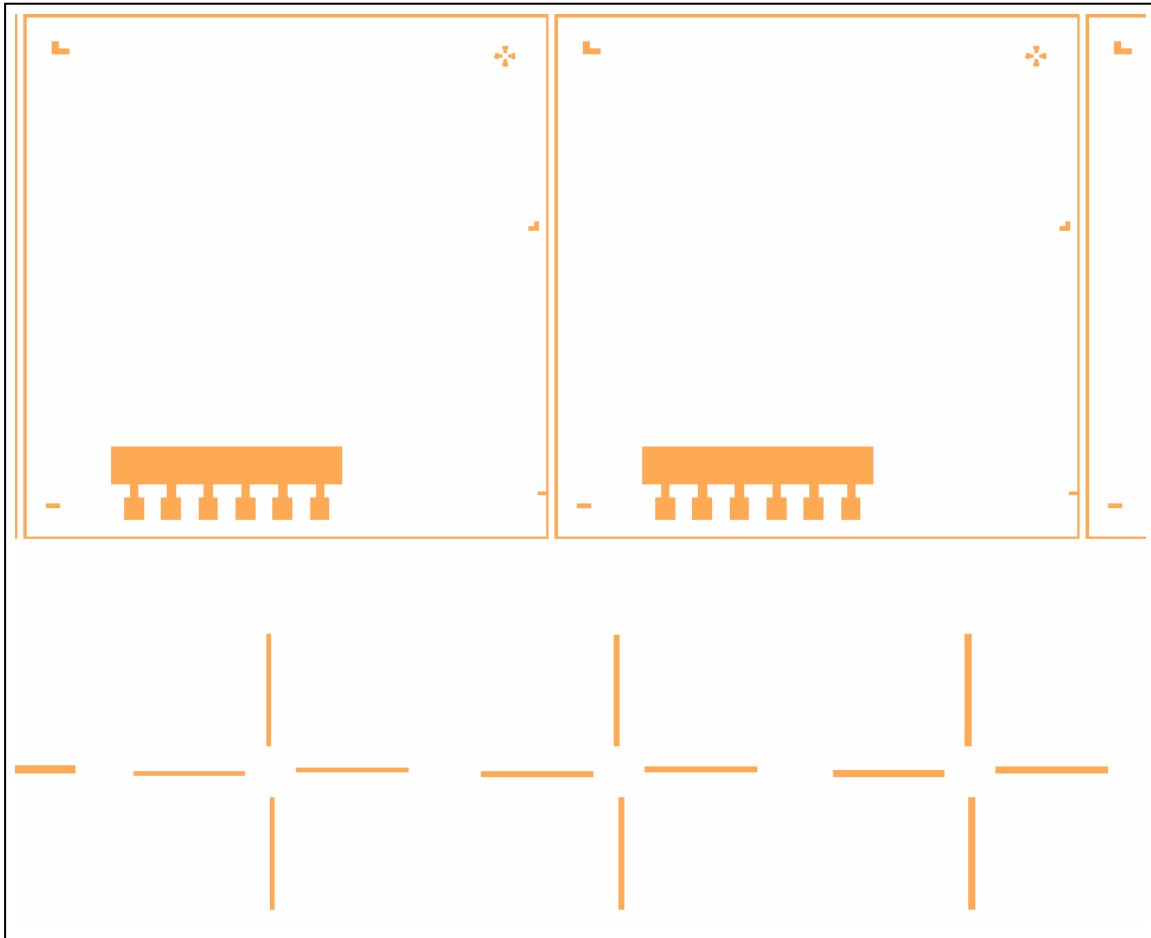


Figure 88: Mask designed in L-Edit to achieve rotor bending and bonding location of the rotor to the electrostatic motors.

- Mask:** Mask designed for rotor blade bending and rotor mounting
- Layout:** Various widths for the rotor bending are done and one rotor mounting spot is shown.
- Comments:** The upper right hand corner of the rectangle is the position of the rotor mounting mask. Along the bottom of the image, the crosses have different line thicknesses for rotor bending.

Appendix C: LabVIEW VI Files and External Circuit

LabVIEW was used to create the required phase shift in the signals for the three phase motors. The LabVIEW block diagram shown in Figure 89 illustrates how the wiring was completed to achieve the proper phase shift in the signals. The signal wiring then had to be connected to the DAQ assistant to determine which analog output each signal was assigned to.

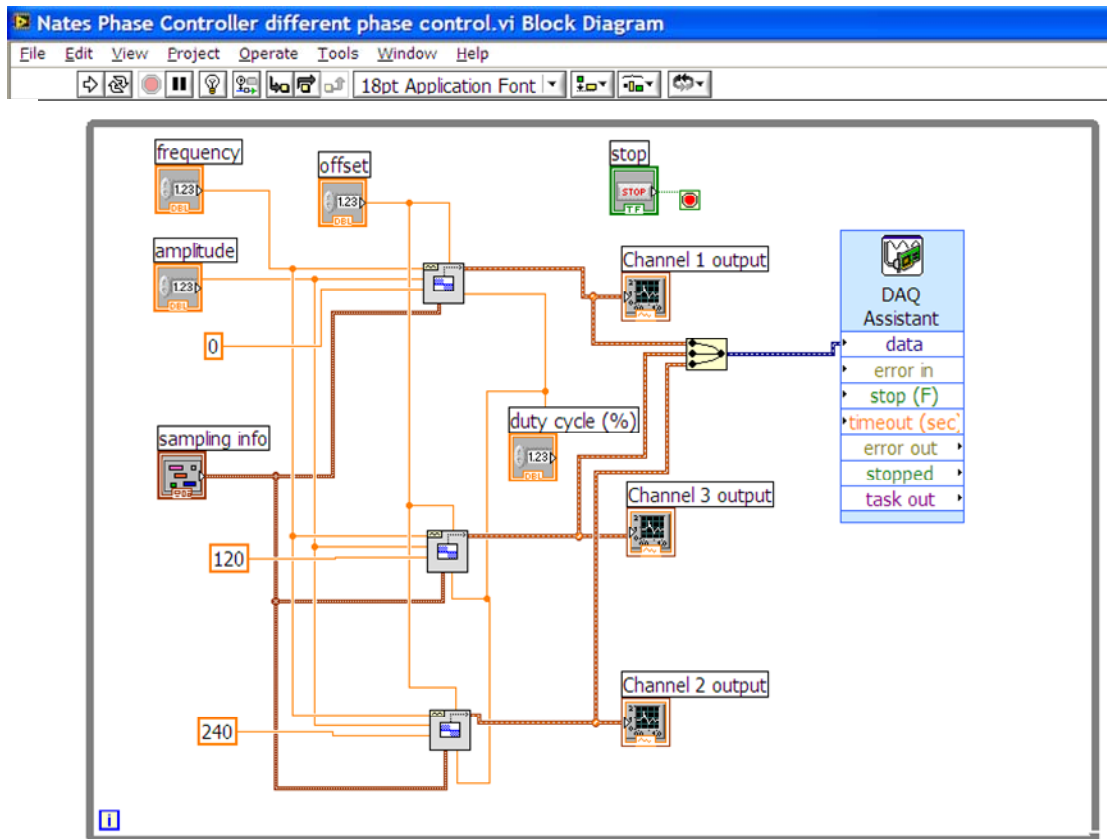


Figure 89: LabVIEW block diagram that is used to generate the three phase signals designed to operate the electrostatic motors.

The LabVIEW front panel shown in Figure 90 is the interface used to input the desired signal frequency, amplitude, duty cycle, and sampling rate. The resulting

waveform plots are shown on the right side of Figure 90, only one channel at a time goes low, just as desired.

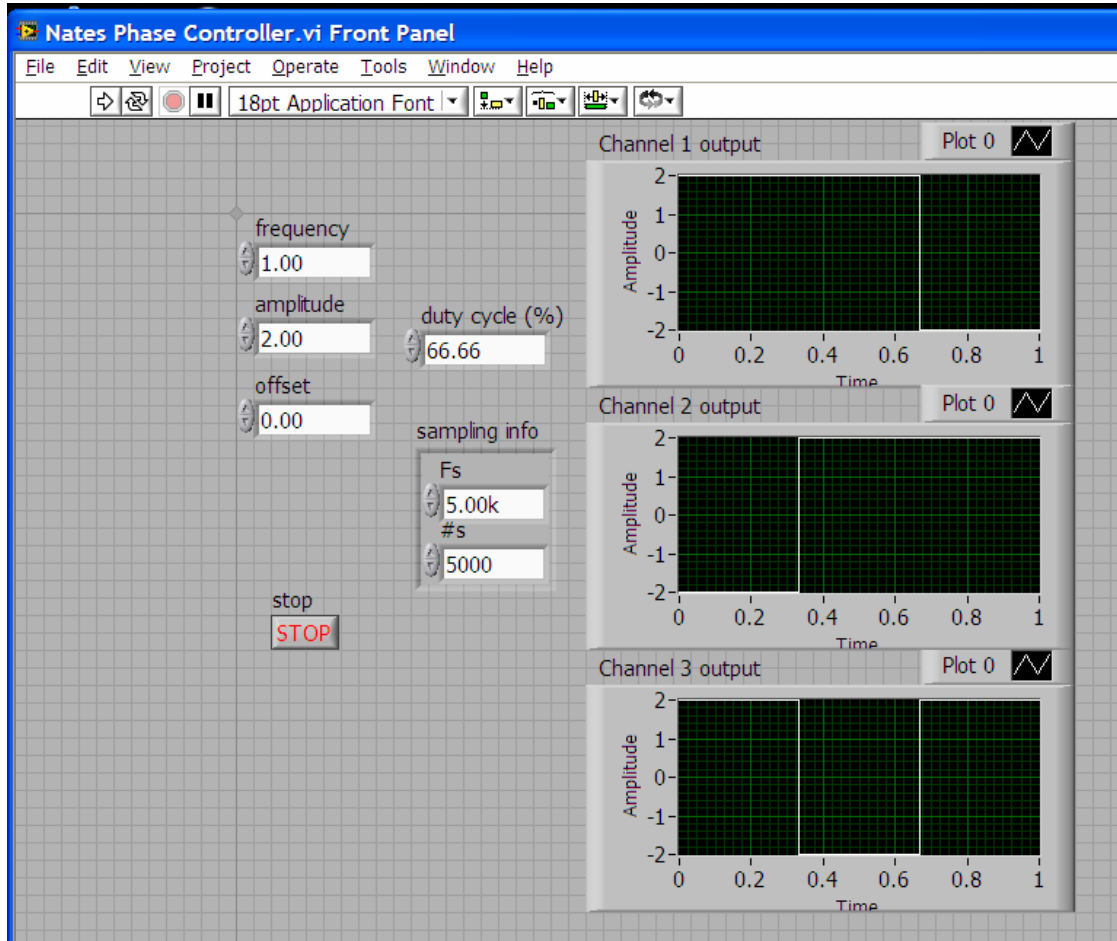


Figure 90: The LabVIEW front panel shows the variables that can be adjusted and what the signal at each output will look like.

One of the external circuits used to drive the electrostatic motors is displayed in Figure 91. The components used in this circuit were limited to a 200 V bias. Another circuit was built later to accommodate a 300 V bias.

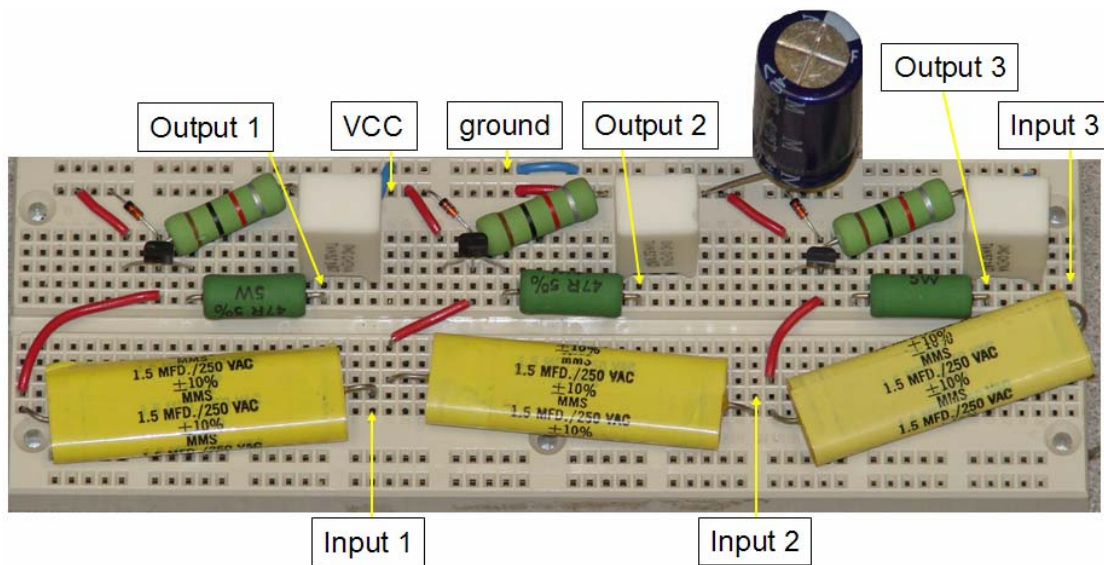


Figure 91: One of the external circuits built to drive the three phase motors.

Appendix D: Comb Drive Calculations

The calculations for the large stacked Poly1/Poly2 comb drive were done in Mathcad below showing the spring constant, electrostatic force, and shuttle displacement.

Designs made of Poly 1&2. Springs have 4 μm wide flexures.

Material Properties

$$\text{Density} := 2.33 \frac{\text{gm}}{\text{cm}^3}$$

Density of polysilicon.

$$\text{Youngs_P1} := 131\text{GPa}$$

Youngs modulus for poly 1.

$$\text{Youngs_P2} := 162\text{GPa}$$

Youngs modulus for poly 2.

$$\text{Thick_P1} := 2\mu\text{m}$$

Thickness of Poly 1.

$$\text{Thick_P2} := 1.5\mu\text{m}$$

Thickness of Poly 2.

$$\text{Thick_oxide} := 0.75\mu\text{m}$$

Thickness of trapped Oxide 2.

Design Parameters

$$\text{Width} := 4\mu\text{m}$$

Width of the springs.

$$\text{Length} := 250\mu\text{m}$$

Length of the springs.

$$I_{z_P1} := \frac{\text{Thick_P1}^3 \cdot \text{Width}}{12}$$

Moment of inertia for each spring layer.

$$I_{z_P2} := \frac{\text{Thick_P2}^3 \cdot \text{Width}}{12}$$

$$k_{x_P1} := \frac{24 \cdot \text{Youngs_P1} \cdot I_{z_P1}}{\text{Length}^3}$$

$$k_{x_P2} := \frac{24 \cdot \text{Youngs_P2} \cdot I_{z_P2}}{\text{Length}^3}$$

$$k_{x_P1} = 0.537 \frac{\text{kg}}{\text{s}^2}$$

$$k_{x_P2} = 0.28 \frac{\text{kg}}{\text{s}^2}$$

Spring constant for each spring layer.

$$k_{x_both} := k_{x_P1} + k_{x_P2}$$

$$k_{x_both} = 0.817 \frac{\text{kg}}{\text{s}^2}$$

Spring constant for the system.

$\text{gap} := 3\mu\text{m}$ Gap between the fingers in the combs.

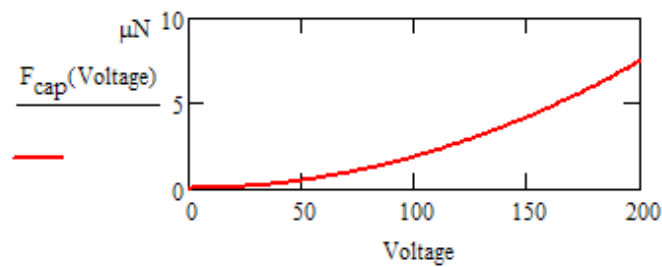
$h := 3.5\mu\text{m}$ Thickness of the fingers.

$\text{Number} := 36$ Number of interdigitated fingers on one side of the comb.

$\epsilon_0 := 8.85418 \cdot 10^{-14} \frac{\text{F}}{\text{cm}}$ Permittivity in vacuum

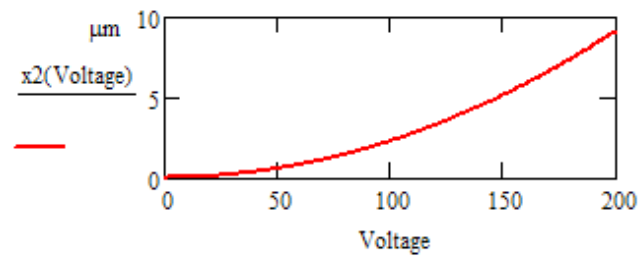
$\text{Voltage} := 0\text{V}, 1\text{V}..200\text{V}$

$$F_{\text{cap}}(\text{Voltage}) := \frac{1}{2} \cdot \text{Number} \cdot \epsilon_0 \cdot \text{Voltage}^2 \cdot \frac{h}{\text{gap}}$$



$F_{\text{cap}}(200\text{V}) = 7.438 \times 10^{-6} \text{ N}$ Electrostatic force in the comb.

$$x2(\text{Voltage}) := \frac{1}{2} \cdot \frac{\text{Number} \cdot h \cdot \epsilon_0 \cdot \text{Voltage}^2}{\text{gap} \cdot k_{x_both}}$$



$x2(200\text{V}) = 9.109 \times 10^{-6} \text{ m}$ Shuttle displacement

Bibliography

- [1] Miki, N. and Shimoyama, I., "Soft-magnetic rotational microwings in an alternating magnetic field applicable to microflight mechanisms," *Journal of Microelectromechanical Systems*, Vol. 12, no. 2, pp. 221–227, April 2003.
- [2] Miki, N. and Shimoyama, I., "Flight Performance of Micro-Wings Rotating in an Alternating Magnetic Field," *Proceedings of the 12th Annual IEEE International Conference on Micro Electro Mechanical Systems – MEMS '99*, pp. 153-158, Orlando, FL, 17-21 Jan . 1999.
- [3] Seiko Epson Corp. http://www.epson.co.jp/e/newsroom/news_2004_08_18.htm, 3 March 2007.
- [4] Linderman, R. J., Kladitis, P. E. and Bright, V. M., "Development of the micro rotary fan", *Sensors and Actuators*, A 95, 2002, pp. 135-142.
- [5] <http://adg.stanford.edu/mesicopter/imageArchive/images/113098Mesi.jpg>
- [6] Kroo, I. and Kunz, P., "Development of the Mesicopter: A Miniature Autonomous Rotorcraft," *American Helicopter Society Vertical Lift Aircraft Design Conference*, San Francisco, CA, 2000.
- [7] Kroo, I. and Kunz, P., "The Mesicopter: A Meso-Scale Flight Vehicle NIAC Phase I Final Report", <http://www-aa.stanford.edu/mesicopter/>.
- [8] Denninghoff, Daniel J. *Power Scavenging MEMS Robots*, MS thesis, AFIT/GE/ENG/06-17, Graduate School of Engineering and Management, Air Force Institute of Technology (AU), Wright-Patterson AFB OH, March 2006.
- [9] Wood, R. J., Avadhanula, S., Menon, M. and Fearing, R. S., "Microrobotics Using Composite Materials: The Micromechanical Flying Insect Thorax," *IEEE International Conference on Robotics and Automation*, Taipei, Taiwan, pp. 1842-1849, May 2003.
- [10] University of California Berkeley,
<http://robotics.eecs.berkeley.edu/~ronf/MFI/mfi.html>, 3 March 2007.
- [11] Chan, H., Lam, J. H. and Li, W. J., "Biomimetic Flying Silicon Microchip: Feasibility Study," *IEEE Int. Conf. on Robotics and Biomimetics (ROBIO) 2004*, Shenyang, China, August 22-26, 2004, pp. 447-451.
- [12] Michelson, R. C. and Naqvi, M. A., "Extraterrestrial Flight (Entomopter-Based Mars Surveyor)," *Low RE Aerodynamics on Aircraft Including Applications in Emerging UAV Technology RTO-AVT von Karman Institute for Fluid Dynamics Lecture Series*, Nov. 24-28, 2003.

- [13] Stiles, Ed, author, <http://uanews.org/cgi-bin/WebObjects/UANews.woa/1/wa/EngrStoryDetails?ArticleID=9796>, 3 March 2007.
- [14] Grasmeyer, J. M., and Keennon, M. T., “Development of the Black Widow Micro Air Vehicle”, *American Institute of Aeronautics and Astronautics*, Vol 0124, pp. 1-9, 2001.
- [15] Keyword – camber, http://en.wikipedia.org/wiki/Camber_%28aerodynamics%29, 3 March 2007.
- [16] Stiles, Ed, author, Aki, Motoyuki, designer, Novel Wing Changes Shape to Optimize Micro Air Vehicle Performance, October 27, 2004.
<http://uanews.org/cgi-bin/WebObjects/UANews.woa/10/wa/ENGRStoryDetails?ArticleID=10016>
- [17] Colucci, Frank, “Battlefield Air Operations Kit”, *Special Operations Technology Online*, <http://www.special-operations-technology.com/article.cfm?DocID=1068>, 1 February 2007.
- [18] Parsch, Andreas, AFRL BATCAM, <http://www.designation-systems.net/dusrm/app4/batcam.html>, 3 March 2007.
- [19] Sniegowski, J. J. and Garcia, E. J., Surface Micromachined Gear Trains Driven by an On-Chip Electrostatic Microengine, *IEEE Electron Device Letters*, Vol. 17, No. 7, July 1996.
- [20] <http://mems.sandia.gov/scripts/images.asp>, 3 March 2007.
- [21] Krygowski, T. W., Rodgers, M. S., Sniegowski, J. J., Miller, S. M. and Jakubczak, J., “A Low-Voltage Rotary Actuator Fabricated Using a Five-Level Polysilicon Surface Micromachining Technology”, 1999 *IEDM*, pp. 697-700.
- [22] Kovacs, G. T. A., *Micromachined Transducers Sourcebook*, WCB/McGraw-Hill, 1998.
- [23] <http://www.sandia.gov/mstc/technologies/micromachines/movies/motors.html>, 3 Mar 2007.
- [24] Lee, J. B., Chen, Z., Allan, M. G., Rohatgi, A. and Arya, R., “A miniaturized high-voltage solar cell array as an electrostatic MEMS power supply, *Journal of Microelectromechanical Systems*, Vol. 4, No. 3, Sept 1995.
- [25] Hollar, S., Flynn, A., Bellew, C. and Pister, K. S. J., Solar Powered 10 mg Silicon Robot, *MEMS 2003*, Kyoto, Japan, January 19-23, 2003.

- [26] Boeing, What is an airfoil,
http://www.boeing.com/companyoffices/aboutus/wonder_of_flight/airfoil.html, 3 March 2007
- [27] T. J. Mueller and J. D. DeLaurier, An overview of Micro Air Vehicle Aerodynamics, *American Institute of Aeronautics and Astronautics*, Inc., 2001.
- [28] McMichael, J. M. and Francis, M. S., Micro Air Vehicles – Toward a New Dimension in Flight, 1997, http://fas.org/irp/program/collect/docs/mav_auvi.htm, 3 March 2007.
- [29] Koester, D., Cowen, A., Mahadevan, R., Stonefield, M. and Hardy, B., PolyMUMPs Design Handbook, a MUMPs[®] Process, Revision 10.0, MEMCAP 2003.
- [30] SUMMiT VTM Five Level Surface Micromachining Technology Design Manual, Version 1.2, Science and Technology Department Microelectronics Development Laboratory, Sandia National Laboratories, 2001.
- [31] Nguyen, C., Micro mechanical Resonators for Oscillators and Filters, *IEEE Ultrasonics Symposium*, 489-499, 1995.
- [32]. Mazer, J. A., *Solar Cells: An introduction to Crystalline Photovoltaic Technology*, Kluwer Academic Publishers, 1997.
- [33]. NASA produced solar irradiance plot, <http://en.wikipedia.org/wiki/MODIS>. 3 March 2007.
- [34]. Energy Efficiency and Renewable Energy; Energy: A 21st Century Perspective; National Academy of Engineering; 2 June 2005.
- [35]. Taya, Minoru, AFOSR-MURI on Energy Harvesting and Storage Systems (EHSS), University of Washington, 25 August 2006.
- [36]. Sze, S. M., *Semiconductor Device Physics and Technology*, 2nd Ed, John Wiley & Sons, Inc., 1985.
- [37]. <http://www.omega.com/techref/das/divider.html>
- [38]. King, R. R., Sherif, R. A., Fetzer, C. M., Colter, P. C., Cotal, H. L., Paredes, A. and Edmondson, K. M., Advances in High-Efficiency Multijunction Terrestrial Concentrator Cells and Receivers, *NCPV and Solar Program Review Meeting 2003*.
- [39]. Sun, W., Kherani, N. P. and Hirschman, K. D., *et. al.*, A Three-Dimensional Porous Silicon p-n Diode for Betavoltaics and Photovoltaics, *Advanced Materials*, Vol. 17, No. 1, 13 May 2005.

- [40]. NASA Jet Propulsion Laboratory, Space Craft Safety,
<http://saturn.jpl.nasa.gov/spacecraft/safety.cfm>, 3 March 2007.
- [41]. Hi-Z Technology Inc., <http://www.hi-z.com/websit02.htm>, 3 March 2007.
- [42]. <http://www.thermoelectrics.com/introduction.htm>, 3 March 2007
- [43]. Argonne National Laboratory, EVS, Human Health Fact Sheet, August 2005,
<http://www.ead.anl.gov/pub/doc/polonium.pdf>, 3 March 2007
- [44]. Cao, Guozhong, AFOSR-MURI on Nanostructured Electrodes for Efficient Energy Storage and Harvesting, University of Washington, 25 August 2006.
- [45]. Spectrolab, A Boeing Company, <http://www.spectrolab.com/prd/terres/cell-main.htm>, 3 March 2007.
- [46] Linderman, R. J. and Bright, V. M., "Optimized Scratch Drive Actuator for Tethered Nanometer Positioning of Chip-Sized Components," *Solid State Sensor and Actuator Workshop, Hilton Head Island, South Carolina, June 4-8*, 214-217, 2000.
- [47] Comtois, J. H. and Bright, V. M., "Design techniques for surface-micromachining MEMS processes," *SPIE*, Vol. 2639, 211-222, 1995.

Vita

Nathan Glauvitz was born in Minneapolis, Minnesota in 1976. In 1978 the Glauvitz family moved to Hustisford, Wisconsin where he grew up with his two sisters. After graduating from Hustisford High School in 1995, he went to the Illinois Institute of Technology (IIT) in Chicago, Illinois on an Air Force ROTC scholarship. After three semesters at IIT, he transferred to the University of Wisconsin–Madison. In 1999 he married his high school sweetheart. He completed a Bachelor of Science Degree in Electrical Engineering at UW-Madison and was commissioned into the Air Force on 21 May 2000. Nathan spent nine months at Vandenberg AFB, California completing missile Initial Qualification Training (IQT) for an operational tour in Space and Missiles. In April 2001 they moved to Minot AFB, North Dakota where he worked as a missileer in the best squadron in the 91st Space Wing, the 740th Missile Squadron. In the summer of 2005, he started the masters program at the Air Force Institute of Technology where he completed the Microelectronics and MEMS sequences. Upon graduation from AFIT he is assigned to work at the Air Force Research Laboratory Starfire Optical Range, Kirtland AFB, New Mexico as a developmental engineer.

REPORT DOCUMENTATION PAGE				Form Approved OMB No. 074-0188	
<p>The public reporting burden for this collection of information is estimated to average 1 hour per response, including the time for reviewing instructions, searching existing data sources, gathering and maintaining the data needed, and completing and reviewing the collection of information. Send comments regarding this burden estimate or any other aspect of the collection of information, including suggestions for reducing this burden to Department of Defense, Washington Headquarters Services, Directorate for Information Operations and Reports (0704-0188), 1215 Jefferson Davis Highway, Suite 1204, Arlington, VA 22202-4302. Respondents should be aware that notwithstanding any other provision of law, no person shall be subject to a penalty for failing to comply with a collection of information if it does not display a currently valid OMB control number.</p> <p>PLEASE DO NOT RETURN YOUR FORM TO THE ABOVE ADDRESS.</p>					
1. REPORT DATE (DD-MM-YYYY) 22-03-2007		2. REPORT TYPE Master's Thesis		3. DATES COVERED (From – To) Jun 2005 – Mar 2007	
4. TITLE AND SUBTITLE TOWARD A FLYING MEMS ROBOT				5a. CONTRACT NUMBER	
				5b. GRANT NUMBER	
				5c. PROGRAM ELEMENT NUMBER	
6. AUTHOR(S) Glauvitz, Nathan E., Captain, USAF				5d. PROJECT NUMBER	
				5e. TASK NUMBER	
				5f. WORK UNIT NUMBER	
7. PERFORMING ORGANIZATION NAMES(S) AND ADDRESS(S) Air Force Institute of Technology Graduate School of Engineering and Management (AFIT/EN) 2950 Hobson Way, Building 640 WPAFB OH 45433-8865				8. PERFORMING ORGANIZATION REPORT NUMBER AFIT/GE/ENG/07-09	
9. SPONSORING/MONITORING AGENCY NAME(S) AND ADDRESS(ES) AFRL/MNAV AFMC Attn: Mr. Chris E. Perry, Lead of Micromunitions Team 101 West Eglin Blvd, Suite 332 Eglin AFB, FL 32536 DSN: 872-4651 (Chris.Perry@eglin.af.mil)				10. SPONSOR/MONITOR'S ACRONYM(S)	
				11. SPONSOR/MONITOR'S REPORT NUMBER(S)	
12. DISTRIBUTION/AVAILABILITY STATEMENT APPROVED FOR PUBLIC RELEASE; DISTRIBUTION UNLIMITED.					
13. SUPPLEMENTARY NOTES					
14. ABSTRACT <p>The work in this thesis includes the design, modeling, and testing of motors and rotor blades to be used on a millimeter-scale helicopter style flying micro air vehicle (MAV). Three different types of motor designs were developed and tested, which included circular scratch drives, electrostatic motors, and comb drive resonators. Six different rotor designs were tested; five used residual stress while one design used photoresist to act as a hinge to achieve rotor blade deflection. Two key parameters of performance were used to evaluate the motor and rotor blade designs: the frequency of motor rotation and the angle of deflection achieved in the rotor blades. One successful design utilized a scratch drive motor with four attached rotor blades to try to achieve lift. While the device rotated successfully, the rotational frequency was insufficient to achieve lift-off. The electrostatic motor designs proved to be a challenge, only briefly moving before shorting out; nonetheless, lessons were learned. Comb drive designs operated over a wide range of high frequencies, lending them to be a promising method of turning a rotary MAV. None of the fabricated devices were able to achieve lift, due to insufficient rotational rates and low angles of attack on the rotor blades. With slight modifications to the current designs, the required rotational rates and rotor blade deflections would yield a viable MAV. The ultimate objective of this effort was to create an autonomous MAV on the millimeter scale, able to sense and act upon targets in its environment. Such a craft would be virtually undetectable, stealthily maneuvering and capable of precision engagement.</p>					
15. SUBJECT TERMS Microelectromechanical systems, MEMS, micro air vehicle (MAV), electrostatic motor, comb drive, scratch drive					
16. SECURITY CLASSIFICATION OF:			17. LIMITATION OF ABSTRACT	18. NUMBER OF PAGES	19a. NAME OF RESPONSIBLE PERSON
a. REPORT	b. ABSTRACT	c. THIS PAGE			LaVern A. Starman, Maj, USAF (ENG)
U	U	U	UU	135	19b. TELEPHONE NUMBER (Include area code) (937) 255-3636, ext 4618 (LaVern.Starman@afit.edu)